

Studies on Sodium-containing Transition Metal Phosphates for Sodium-ion Batteries

Masafumi Nose

2016

Studies on Sodium-containing Transition Metal Phosphates for Sodium-ion Batteries

Masafumi Nose

Department of Energy and Hydrocarbon Chemistry
Graduate School of Engineering
Kyoto University
Kyoto, Japan

2016

Preface

This thesis is a compilation of ‘Studies on Sodium-containing transition Metal Phosphates for Sodium-ion Batteries’, carried out by the author under the supervision of *Professor Takeshi Abe*, Department of Energy and Hydrocarbon Chemistry, Graduate School of Engineering, Kyoto University during 2013-2016.

The author wishes to express his sincere gratitude to *Professor Takeshi Abe* for his guidance, suggestions and discussions throughout this work. The author wishes to thank *Professor Tetsuo Sakka* and *Professor Hiroshi Kageyama*, Graduate School of Engineering, Kyoto University, for their helpful comments and discussions.

The author is deeply grateful to *Dr. Hideki Iba*, *Dr. Shinji Nakanishi*, *Mr. Hidetaka Nishikoori* and *Dr. Hideki Nakayama* (Toyota Motor Corporation) for their continuous encouragement and understanding toward accomplishing this thesis. The author is deeply indebted to *Dr. Hiroki Moriwake* (Japan Fine Ceramics Center) for his support and fruitful discussions.

Finally, the author wishes to express his special thanks to his family *Tomoyo*, *Sota* and *Yuto* for their warm encouragement and deep understanding toward accomplishing this thesis.

Masafumi Nose

Kyoto Japan

2016

Contents

General Introduction

Background of the work	1
Outline of the work	7

Chapter 1

$\text{Na}_4\text{Co}_3(\text{PO}_4)_2\text{P}_2\text{O}_7$; Novel Electrode Material for Sodium-ion Batteries

1.1. Introduction	13
1.2. Experimental	14
1.3. Results and Discussion	16
1.4. Conclusions	19

Chapter 2

Structural and Electrical Analysis of $\text{Na}_4\text{Co}_3(\text{PO}_4)_2\text{P}_2\text{O}_7$ during Electrochemically Na^+ Extraction/Insertion

2.1. Introduction	27
2.2. Experimental	29
2.3. Results and Discussion	29
2.4. Conclusions	34

Chapter 3

$\text{Na}_4\text{Ni}_3(\text{PO}_4)_2\text{P}_2\text{O}_7$; First-ever Experimental Evidence on Potentially Highest Properties of Nickel-based Polyanion Family

3.1. Introduction	47
3.2. Experimental	48
3.3. Results and Discussion	50
3.4. Conclusions	56

Chapter 4

Na₄Co_{2.4}Mn_{0.3}Ni_{0.3}(PO₄)₂P₂O₇ : High Potential and High Capacity Electrode Material for Sodium-Ion Batteries

4.1. Introduction	71
4.2. Experimental	72
4.3. Results and Discussion	73
4.4. Conclusions	77

Chapter 5

Electrochemical Li⁺ Insertion Capability into Na_{4-x}Co₃(PO₄)₂P₂O₇ and Its Application to Novel Hybrid-ion Battery

5.1. Introduction	83
5.2. Experimental, Results and Discussion	84
5.3. Conclusions	88

Publication List	98
------------------	----

GENERAL INTRODUCTION

Background of the work

Lithium-ion batteries (LIBs) have been well established as power sources of portable electric devices for the last 20 years because of their high energy density, light weight, long cycle life and so on¹⁻³. To date, LIBs have diversified their applications such as eco-friendly vehicles and therefore have been still developing for new requirements. To meet the demands of the large-scale applications, much effort has been devoted to new type batteries (e.g. sodium and manganese ion batteries^{4,5}) which would make it possible to build up a sustainable society with green chemistry. Especially, high power battery ($W = I \times V$), which can be achieved by the compatibility of high rate capability (I) and high voltage (V), has been strongly desired to further enhance the fuel and/or electrical efficiency of upcoming systems, which are so-called “energy efficiency”.

In rockin-chair-type batteries as represented by LIBs and sodium-ion batteries (SIBs), rate capability is determined by any one of the following rate-limiting steps. (I) Ion conduction in electrolyte, (II) Ion transfer at the electrolyte / electrode interface *via*. desolvation process, and (III) Ion diffusion in the bulk of electrode materials *via*. phase transition. It is well accepted that LIBs have suffered from the disadvantage of high activation barrier of Li^+ transfer at the electrolyte / electrode interface owing to high Lewis acidity of Li^+ and therefore high interaction between Li^+ and solvent. On the other hand, some fundamental studies clarified lower activation barrier of Na^+ transfer at the electrolyte / electrode interface because of lower Lewis acidity of Na^+ than Li^+ , indicating SIBs should have potentially advantage of providing high rate capability as long as suitable electrode materials can be used⁶.

1. Positive electrode materials

In this section, representative materials as a positive electrode of LIBs and SIBs will be summarized.

1-1. Positive electrode materials for LIBs

Early findings on positive electrode materials for LIBs are divided into three crystal structures (Fig. 1) of Layered rocksalt (LiMO_2)⁷⁻⁹, Spinel ($\text{LiM}_x\text{M}'_{2-x}\text{O}_4$)^{10,11} and Olivine (LiMPO_4)¹².

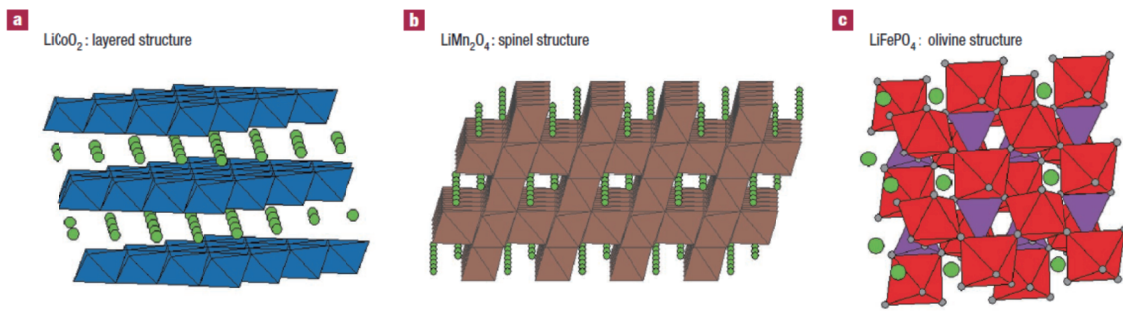
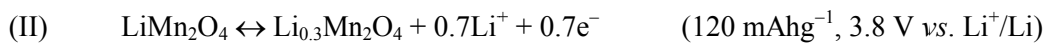
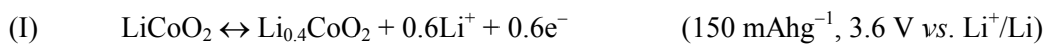


Fig. 1 Polyhedral views of crystal structures of a) LiCoO_2 , b) LiMn_2O_4 and c) LiFePO_4 ¹³

Li^+ accommodation sites in these crystal structures were well designed along diffusion pathways and charge compensation by redox reactions of transition metal ion [$\text{M}^{n+}/\text{M}^{(n+1)+}$] makes it possible to release Li^+ and electron (e^-) simultaneously to negative electrode and outer loading, respectively. Typical half reaction equations at positive electrode side during charge/discharge are described as follows.





In order to enhance their performances, there have been various attempts of optimizing synthesis conditions, particle sizes, lattice doping to transition metal sites and so on. Such great efforts led to discoveries of derivative electrode materials such as $\text{LiNi}_{1/3}\text{Co}_{1/3}\text{Mn}_{1/3}\text{O}_2$ (NCM)¹⁴, $\text{LiNi}_{0.5}\text{Mn}_{1.5}\text{O}_4$ (LMNO)^{15,16} and LiCoPO_4 (LCPO)^{17,18}, whose reversible capacity, potential, rate and/or cycle performances were improved as compared with electrode materials. In parallel with the developments, new Li^+ intercalation structures such as Tavorite structure (e.g. LiFeSO_4F ¹⁹ and LiVPO_4F ²⁰) and pyrophosphates (e.g. $\text{Li}_2\text{MP}_2\text{O}_7$ ²¹ and LiVP_2O_7 ²²) have been reported so far.

1-2. Positive electrode materials for SIBs

Fundamental researches on electrochemical Na^+ intercalation into/from crystal lattice of ceramics such as NaMO_2 ($M = \text{Ni, Mn and Co}$) were already carried out in 1950s, but have gradually faded out since the commercialization of LIBs by SONY corp. in 1991. Hence, typical positive electrode materials for SIBs had been restricted as layered structure (Na_xMO_2)^{23,24} and NASICON structure²⁵. Since Okada et al. reported the electrochemical properties of NaFeO_2 ²⁶ in 2005, SIBs have been reconsidered as one of the key technologies from the reasons as follows. The first is an abundant of sodium working as an ionic carrier instead of Li^+ and the other is the various intercalation structures, which are not familiar with lithium equivalences. Actually, many unique electrode materials (e.g. $\text{Na}_2\text{MP}_2\text{O}_7$ [$M = \text{Fe, Mn and Co}$]²⁷⁻²⁹, $\text{Na}_2\text{FePO}_4\text{F}$ ³⁰, and $\text{Na}_3\text{V}_2(\text{PO}_4)_2\text{F}_3$ ³¹) have been reported in 2000s.

1-3. Performance maps

As mentioned in the section 1, high operating voltage (V) is desirable to establish high power

batteries ($W = V \times I$) and therefore $\text{LiNi}_{0.5}\text{Mn}_{1.5}\text{O}_4$ ^{15,16} and/or LiCoPO_4 ^{17,18} would be attractive electrode materials owing to their high potentials of 4.8 V vs. Li^+/Li . But unfortunately, reversible capacities of either material gradually decreased during repeated charge/discharge reactions, because of some serious problems such as structural degradation^{32,33}, transition metal dissolution by HF formation³⁴ and so on. Given the critical situation, NCA, NMC or LiMn_2O_4 are still assembled as a positive electrode in the state-of-the-art of LIBs. Hence, when graphite or $\text{Li}_4\text{Ti}_5\text{O}_{12}$ as a typical negative electrode is combined, their average voltages exhibit not more than 3.7 V or 2.3 V-class³⁵, respectively.

On the other hand, as summarized in Fig. 2, there have been no electrode materials for SIBs which operate at comparable potential region to 4.8 V-class Olivine LiCoPO_4 or Spinel $\text{LiNi}_{0.5}\text{Mn}_{1.5}\text{O}_4$.

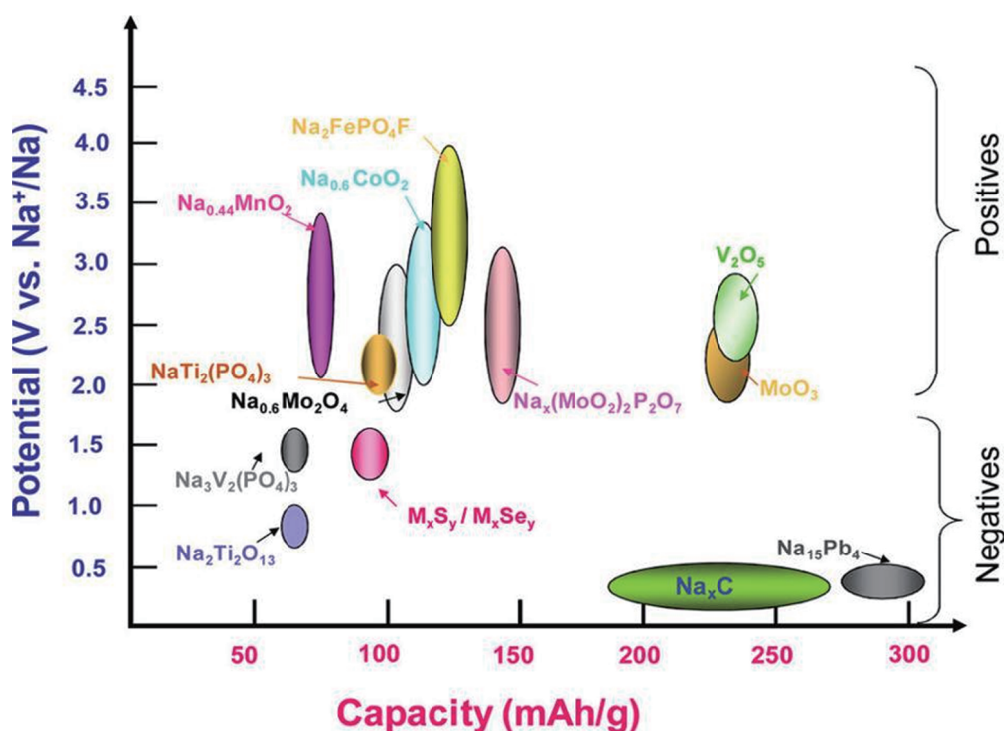


Fig. 2 Performance map of ever reported electrode materials for SIBs³⁶.

Maricite NaMPO_4 [$M = \text{Co}$ and/or Ni] may have a nice operating potential beyond 4.0 V vs. Na^+/Na from material screening done by DFT calculation. Actually, Maricite phase is electrochemically inactive from its structural viewpoint, namely, Na^+ are located in the enclosed framework and octahedral CoO_6 unit block the Na^+ diffusion. Nevertheless, it should be noted that high redox potentials of transition metal have been certainly induced by polyanion unit such as PO_4 , which is so-called ‘inductive effect’. Accordingly, the author focussed on sodium-containing transition metal phosphates which have a wider variety of stable phases on phase diagram than lithium-containing ones.

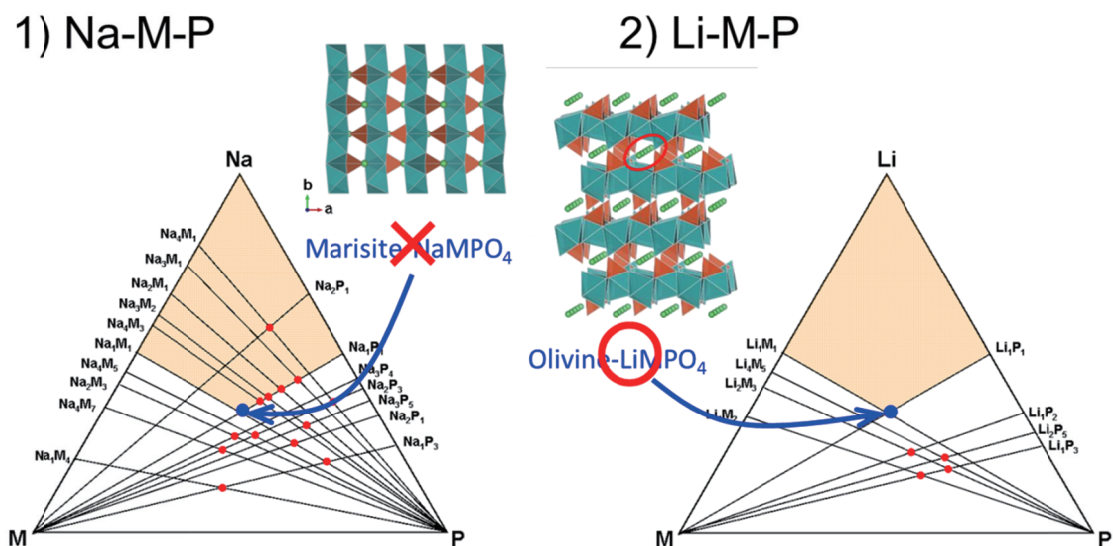


Fig. 3 Phase diagrams of 1) Na-M-P and 2) Li-M-P systems .

Among them, the crystal structure of $\text{Na}_4\text{M}_3(\text{PO}_4)_2\text{P}_2\text{O}_7$ [$M = \text{Fe}, \text{Mn}, \text{Co}$ and Ni]^{38,39} should be attractive for new positive electrode materials of SIBs from the possible reasons as follows.

- 1) High theoretical capacity of ca. 170 mAhg^{-1} estimated by reversible extraction/insertion of 4Na^+ .

- 2) Geometrically well-designed 3D diffusion pathways locating Na^+ sites as described by Bond Valence Sum (BVS) method (Fig. 4).
- 3) High redox potentials of $\text{Co}^{2+}/\text{Co}^{3+}$ or $\text{Ni}^{2+}/\text{Ni}^{3+}$ induced by inductive effect of PO_4 and/or P_2O_7 frameworks
- 4) Wide selectivity in novel solid solution phases of central transition metal because of close ionic radius between Mn^{2+} , Co^{2+} and Ni^{2+} .

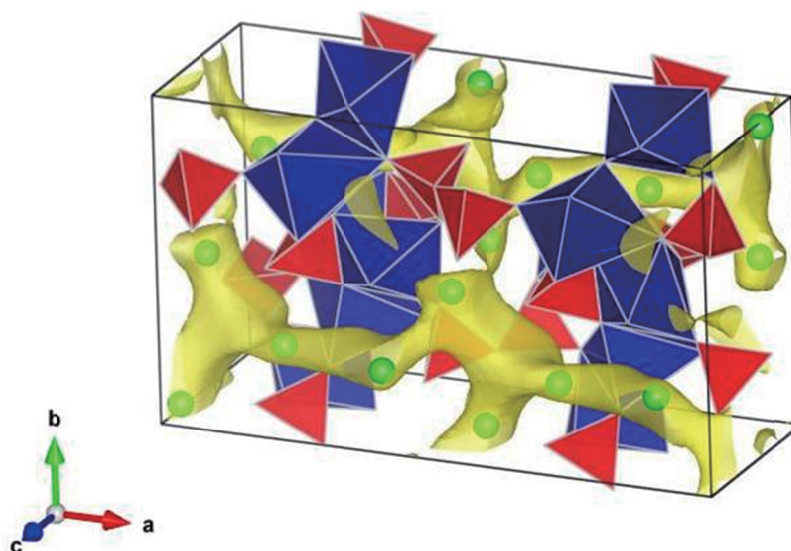


Fig 4. Geometrically large space, indicating possible diffusion pathways, in crystal structures (Polyhedral views) of $\text{Na}_4\text{Co}_3(\text{PO}_4)_2\text{P}_2\text{O}_7$ visualized by Bond Valence Sum (BVS) method⁴⁰⁻⁴².

In spite of such positive motivations, electrochemical characteristics of $\text{Na}_4M_3(\text{PO}_4)_2\text{P}_2\text{O}_7$ [$M=\text{Co}$ and Ni] had not been clarified at all before the author started the researches and has been investigated in the author's work.

Outline of the work

As mentioned above, new electrode materials are still desired to establish high power batteries. In LIBs, many researchers have investigated and developed the performances of lithium-containing compounds for the last several decades and thus their properties are well understood. On the other hand, there are few researches on electrode materials for SIBs, while the sodium-containing compounds have more variety of crystal structures which are not familiar with the lithium counterparts. Owing to the polymorph of sodium-containing compounds, the possibility of sodium-ion batteries should be reconsidered. Hence, the author has been focussing on $\text{Na}_4\text{Co}_3(\text{PO}_4)_2\text{P}_2\text{O}_7$ and its derivatives as the possible intercalation structure whose electrochemical, structural and electrical characteristics during Na^+ insertion/extraction had not been clarified yet. Brief summaries of my thesis are as follows:

In chapter I, the author investigated electrochemical properties of $\text{Na}_4\text{Co}_3(\text{PO}_4)_2\text{P}_2\text{O}_7$ as a new electrode material for SIBs. $\text{Na}_4\text{Co}_3(\text{PO}_4)_2\text{P}_2\text{O}_7$ can deliver the reversible capacity of 95 mAhg^{-1} , corresponding to ca. 56% of its theoretical capacity in the highest potential region of 4.1-4.7 V vs. Na^+/Na among ever reported electrode materials for SIBs. The reversible capacity could be repeatedly delivered after 50 cycle and retain ca. 80% even at 25C rate. The properties indicate $\text{Na}_4\text{Co}_3(\text{PO}_4)_2\text{P}_2\text{O}_7$ has the compatibility of high operating potential and rate capability, while the low utilization of its theoretical capacity should be improved before the practical use for SIBs.

In chapter II, structural and electrical properties of $\text{Na}_4\text{Co}_3(\text{PO}_4)_2\text{P}_2\text{O}_7$ during Na^+ extraction/insertion was investigated by First-principles calculations in order to understand the residual issue of low reversible capacity as shown in chapter I. Assuming a stepwise desodiation process, removal of Na down to $\text{Na}_4\text{Co}_3(\text{PO}_4)_2\text{P}_2\text{O}_7$ is found to be accompanied by oxidation of

Co^{2+} to Co^{3+} . Further removal of Na to give $\text{Co}_3(\text{PO}_4)_2\text{P}_2\text{O}_7$ requires oxidation of oxygen 2p orbitals, rather than Co^{2+} being oxidized to Co^{3+} . At the same time, a large volume shrinkage is observed during this last desodiation step. These two factors may explain the difficulty encountered experimentally in removing Na from $\text{NaCo}_3(\text{PO}_4)_2\text{P}_2\text{O}_7$.

In chapter III, the author describes the electrochemical and structural characteristics of $\text{Na}_4\text{Ni}_3(\text{PO}_4)_2\text{P}_2\text{O}_7$ as the member within nickel-based polyanion family such as LiNiPO_4 , which has created considerable interest for their potentially highest properties predicted by previous calculation results. At first, the experimental evidence on the highest potential of 4.8 V-class (vs. Na^+/Na) among ever reported electrode materials supports the previous predictions for higher potentials of $\text{Ni}^{2+}/\text{Ni}^{3+}$ than $\text{Co}^{2+}/\text{Co}^{3+}$ in any isostructural polyanion frameworks. Next, we identified, through synchrotron X-ray diffraction, the competitive two phase reactions utilizing multiple diffusion pathways at the former charge and subsequently structural rearrangement to new single phase by further Na^+ extraction. Finally, by combining their reaction potentials obtained from cyclic voltammetry technique and structural analysis, the author discussed the competitiveness and the reversibility of the structural transformation, which contribute to the superior rate and cycle performances, respectively.

In chapter IV, the author investigated the electrochemical properties of $\text{Na}_4\text{Co}_{2.4}\text{Ni}_{0.3}\text{Mn}_{0.3}(\text{PO}_4)_2\text{P}_2\text{O}_7$ as one of the representative solid solution phases of $\text{Na}_4M_3(\text{PO}_4)_2\text{P}_2\text{O}_7$ [$M=\text{Co}$, Ni and Mn]. $\text{Na}_4\text{Co}_{2.4}\text{Mn}_{0.3}\text{Ni}_{0.3}(\text{PO}_4)_2\text{P}_2\text{O}_7$, isostructural to $\text{Na}_4\text{Co}_3(\text{PO}_4)_2\text{P}_2\text{O}_7$, was successfully synthesized by using a sol-gel method and has been evaluated as a positive electrode for sodium-ion batteries. The novel material has two redox couples around 4.2 V and 4.6 V vs. Na^+/Na on the cyclic voltammograms and can deliver the high capacity of ca. 103 mAhg^{-1} even

at the high current density of 850 mA g^{-1} (5C). X-ray absorption spectroscopy (XAS) results show that Co, Mn and Ni redox proceed simultaneously in the charge process and it is indicated the novel material provide high mixed potential of Co, Mn and Ni redox. These findings suggest the derivatives of $\text{Na}_4\text{Co}_3(\text{PO}_4)_2\text{P}_2\text{O}_7$ should be employed as high potential and high capacity electrode materials.

In chapter V, the author describes both Li^+ and Na^+ insertion capabilities of electrochemically Na^+ -extracted $\text{Na}_{4-x}\text{Co}_3(\text{PO}_4)_2\text{P}_2\text{O}_7$. Given the compatible properties, the new-type hybrid-ion battery was also demonstrated by combining $\text{Na}_4\text{Co}_3(\text{PO}_4)_2\text{P}_2\text{O}_7$ positive electrode and $\text{Li}_4\text{Ti}_5\text{O}_{12}$ negative electrode in lithium-based electrolyte.

References

1. Tarascon, J-M. & Armand, M., *Nature* 414, 359-367 (2001).
2. Armand, M. & Tarascon, J-M., *Nature* 451, 652-657 (2008).
3. Thackeray, M, *Nature Mater.* 1 (2002) 81-82.
4. N. Yabuuchi, K. Kubota, M. Dahbi and S. Komaba, *Chem. Rev.*, 2014, 114 (23), 11636–11682.
5. D. Aurbach , Z. Lu , A. Schechter , Y. Gofer , H. Gizbar , R. Turgeman , Y. Cohen , M. Moshkovich & E. Levi, *Nature* 407, 724–727.
6. F Sagane, T Abe, Y Iriyama, Z Ogumi, *J. Power Sources*, 146 1-2 (2005) 749-752
7. K. Mizushima, P. C. Jones, P. J. Wiseman, J. B. Goodenough, *Mater. Res. Bull.*, 15 (1980) 783.
8. J. N. Reimers, J. R. Dahn, *J. Electrochem. Soc.*, 139 8 (1992) 2091.
9. J. M. Paulsen, J. R. Mueller-Neuhaus, J. R. Dahn, *J. Electrochem. Soc.*, 147 (2) (2000) 508.
10. Y. Xia, H. Noguchi, M. Yoshio, *J. Power Sources*, 56 (1995) 61.
11. R. J. Gummow, A de Kock, M. M. Thackeray, *Solid State Ionics*, 69 (1994) 59.
12. A. K. Padhi, K. S. Nanjundaswamy, J. B. Goodenough, *J. Electrochem. Soc.*, 144 (1997) 1188.
13. T. Ohzuku, R. J. Brodd, *J. Power Sources*, 174(2) (2007) 449.
14. N. Yabuuchi, Y. Koyama, N. Nakayama and T. Ohzuku, *J. Electrochem. Soc.*, 152 7 (2005) A1434-A1440.
15. M. Okada, Y.-S. Lee, M. Yoshio, *J. Power Sources*, 90 2 (2000) 196-200.
16. Y. E. Eli, J. T. Vaughey, M. M. Thackeray, S. Mukerjee, X. Q. Yang and J. McBreen, *J. Electrochem. Soc.*, 146 3 (1999) 908-913.

17. K. Amine, H. Yasuda, M. Yamachi, *Electrochem. Solid State Lett.*, 3 (2000) 178.
18. S. Okada, S. Sawa, M. Egashira, J. Yamaki, M. Tabuchi, H. Kageyama, T. Konishi, A. Yoshino, *J. Power Sources*, 97 (2001) 430.
19. N. Recham, J-N. Chotard, L. Dupont, C. Delacourt, W. Walker, M. Armand & J-M. Tarascon, *Nature Materials*, 9 (2010) 68-74.
20. J. Barker, R. K. B. Gover, P. Burns, A. Bryan, M. Y. Saidi, J. L. Swoyer, *J. Power Sources*, 146 1-2 (2005) 516-520.
21. T. Ye, P. Barpanda, S.-Nishimura, N. Furuta, S.-C. Chung and A. Yamada, *Chem. Mater.*, 25 (18) (2013) 3623-3629.
22. J. Barker, R. K. B. Gover, P. Burns, A. Bryan, *Electrochem. Solid-State Lett.*, 8 (9) (2005) A446-A448.
23. C. Delmas, J. J. Bracnner, C. Fouassier, P. Hagenmuller, *Solid State Ion.*, 3-4 (1981) 165.
24. R. Berthelot, D. Carlier, C. Delmas, *Nature Mater.*, 10 (2011) 74.
25. A. K. Padhi, K. S. Nanjundaswamy, C. Masquelier and J. B. Goodenough, *J. Electrochem. Soc.*, 144 (8) (1997) 2581-2586.
26. S. Okada, Y. Takahashi, T. Kiyabu, T. Doi, J. Yamaki and T. Nishida, *ECS Meeting Abstract* 602, 201 (2006).
27. P. Barpanda, G. Liu, C. D. Ling, M. Tamaru, M. Avdeev, S. C. Chung, Y. Yamada and A. Yamada, *Chem. Mater.*, 25 (17) (2013) 3480-3487.
28. P. Barpanda, T. Ye, M. Avdeev, S. C. Chung and A. Yamada, *J. Mater. Chem. A*, 1 (2013) 4194-4197.
29. P. Barpanda, T. Ye, M. Avdeev, S. C. Chung and A. Yamada, *Inorg. Chem.*, 52 (1) (2013) 395-401.
30. Y. Kawabe, N. Yabuuchi, M. Kajiyama, N. Fukuhara, T. Inamasu, R. Okuyama, I. Nakai

- and S. Komaba, *Electrochemistry*, 80 (2012) 80-84.
31. K. Chihara, A. Kitajou, I. D. Gocheva, S. Okada and J. Yamaki, *J. Power Sources*, 227 (2013) 80-85.
 32. Quang Duc Truong, Murukanahally Kempaiah Devaraju, Takaaki Tomai, and Itaru Honma, *ACS Appl. Mater. Interfaces*, 5 (2013) 9926.
 33. Quang Duc Truong, Murukanahally Kempaiah Devaraju, Yoshikazu Sasaki, Hiroshi Hyodo, Takaaki Tomai, and Itaru Honma, *Chem. Mater.*, 26 (2014) 2770.
 34. Y.-K. Sun, K.-J. hong, J. Prakash and K. Amine, *Electrochem. Comm.*, 4 (4) (2002) 344-348.
 35. S. Kisugi, H. Inagaki and N. Takami, *Toshiba Review*, 63 (2) (2008) 54-57.
 36. P. Senguttuvan, V. Seznec, J.-M. Tarascon and M. R. Palacin, *Chem. Mater.* **23**, 4109–4111 (2011).
 37. S. P. Ong, V. L. Chevrier, G. Hautier, A. Jain, C. Moore, S. Kim, X. Ma and G. Ceder, *The Royal Society of Chemistry* 4, 3680-3688 (2011).
 38. F. Sanz, C. Parada, U. Amador, M.A. Monge and C. Ruiz-Valero, *J. Solid State Chem.*, 1996, **123**, 129-139.
 39. F. Sanz, C. Parada, J. M. Rojo, and C. Ruiz-Valero, *Chem. Mater.*, 2001, **13**, 1334-1340.
 40. S. Adams, *Acta Cryst*, B57 (2001) 278.
 41. F. Izumi and K. Momma, *Solid State Phenom.* 130 (2007) 15-20.
 42. K. Momma and F. Izumi, *J. Appl. Crystallogr.* 41 (2008) 653-658.

Chapter I

$\text{Na}_4\text{Co}_3(\text{PO}_4)_2\text{P}_2\text{O}_7$; Novel Electrode Material for Sodium-ion Batteries

1.1. Introduction

Lithium-ion batteries (LIBs) have been well established as power sources of portable electric devices for the last 20 years because of their high energy density, light weight, long cycle life and so on¹⁻³. To date, LIBs have diversified their applications not only as large-scale power sources of hybrid vehicles (HVs), plug-in hybrid vehicles (PHVs) and electric vehicles (EVs) but also as back-up storage systems of solar and wind energy, which have been developing for new requirements yet. In order to meet the expectations and demands, much effort has been devoted on the new types of rechargeable batteries as represented by sodium-ion batteries. As summarized in Figure S1 showing the average voltage *vs.* capacity, various sodium storage materials have been recently reported not only for a positive electrode (e.g. layered oxides⁴⁻⁶ and phosphates⁷⁻⁹) but also for a negative electrode (e.g. carbonaceous material¹⁰ and titanium oxides¹¹⁻¹³). However, sodium storage materials for a positive electrode with both high operating potential and high Na^+ diffusivity in the bulk, which are also parameters to determine high power of the battery, have not been found yet. Lack of the compatible storage material is one of the most important issues to establish high power type sodium-ion batteries.

Maricite NaCoPO_4 may have a nice operating potential beyond 4.0 V *vs.* Na^+/Na from

material screening done by DFT calculation¹⁴. High redox potential of transition metal has been certainly induced by polyanion unit such as PO₄. However, from its structural viewpoint shown in Figure S2, NaCoPO₄ is electrochemically inactive because Na⁺ are located in the enclosed framework and octahedral CoO₆ unit block the Na⁺ diffusion. In LIBs, olivine LiFePO₄ is well known to electrochemically active because it has a one-dimensional (1D) Li⁺ mobile route in the bulk¹⁵. These results suggest that the crystal structure will play an important role in mobile ion's diffusivity in the bulk. Here, we focused on various polymorphs of sodium-based cobalt phosphates, which might not be familiar with lithium-based cobalt phosphates. Among them, we have succeeded in discovering a notably unique and electrochemically active crystal structure of Na₄Co₃(PO₄)₂P₂O₇. Na₄Co₃(PO₄)₂P₂O₇ has a space group of *Pn*2₁a and Co₃P₂O₁₃ blocks parallel to bc plane are linked with P₂O₇ unit along a-axis¹⁶. Interestingly, four types of Na⁺ sites are located in the 3D ion channel, which can be seen in the spinel type LiMn₂O₄ and Li₄Ti₅O₁₂ as promising candidates for storage materials in high power types of LIBs. Considering the multiple and fast ion diffusivity in the spinel compounds³, Na⁺ mobility in the 3D ion channel must be much higher than the 1D or 2D ion channel's ones, and thus Na₄Co₃(PO₄)₂P₂O₇ can be a fast ion diffusive material in the bulk. In this chapter, we demonstrate the properties of the novel sodium storage material Na₄Co₃(PO₄)₂P₂O₇.

1.2. Experimental

Na₄Co₃(PO₄)₂P₂O₇ was synthesized by using a typical sol-gel method. Reagent grade of (CH₃COO)₂Co, Na₄P₂O₇ and NH₄H₂PO₄ (Nacalai tesque) were used as the starting materials. These materials were mixed in a diluted nitric acid solution and then glycolic acid was added to prevent the particle growth of Na₄Co₃(PO₄)₂P₂O₇ precursor. The solution was heated at 80°C for 12 hr with continuous stirring. The gel obtained was annealed to 700°C for 50hr under air

atmosphere. After that, the active material and Vapor-Grown Carbon Fiber (Showa Denko, VGCF, battery grade) were mixed with a weight ratio of 5 to 1, and subsequently carbothermal treatment was carried out at 700°C for 5hr under purging Ar. Then, a N-methyl pyrrolidone (NMP) based slurry composed of the $\text{Na}_4\text{Co}_3(\text{PO}_4)_2\text{P}_2\text{O}_7$ /VGCF composite (90wt%), acetylene black (battery grade, 5wt%) as a conductive filler and poly(vinylidene fluoride) (battery grade, PVdF, 5wt%) as a binder was cast on an aluminum current collector.

The as-prepared material was characterized by powder X-ray diffraction measurements with X-ray diffractometer (Ultima IV, Rigaku corp. Ltd., Japan) using Cu $K\alpha$ radiation with 40 kV of tube voltage and 40 mA of current. Schematic illustrations of the crystal structure of $\text{Na}_4\text{Co}_3(\text{PO}_4)_2\text{P}_2\text{O}_7$ were drawn using the program VESTA²⁷. Surface morphology of the as-prepared material was obtained with a field emission scanning electron microscope (Ultra55, ZEISS).

CR2032-type coin cell was fabricated with the above-described positive electrode. Metallic sodium (Aldrich) was used as a negative electrode and 1.0 mol/cm³ NaPF₆ (Kishida Chem., battery grade) dissolved in ethylene carbonate (EC) / diethylene carbonate (DEC) (50:50 by vol., Kishida Chem., battery grade) was applied to the electrolyte. All electrochemical tests were conducted in a thermostatic bath maintaining at 25°C. Cyclic voltammetry was measured using VMP3 (Biologic) at a constant scan rate of 0.01 mVs⁻¹ in the potential region between 3.9 V and 4.8 V vs. Na⁺/Na. Galvanostatic charge-discharge test was carried out using a charge-discharge machine (SM8, Hokuto) at a constant current density of 34 mA/g (0.2C) between 3.0 V and 4.7 V vs. Na⁺/Na. 1C was defined as the current density of 170 mA/g, at which its theoretical capacity (170 mAh/g) can be delivered for an hour. Rate performances were also evaluated using another charge-discharge machine (BTS2004, Nagano) between 2.0 V and 5.0 V vs. Na⁺/Na at different current densities of 1700 mA/g (10C), 3400 mA/g (20C) and

4250 mA/g (25C).

New type sodium-ion battery was assembled by combining $\text{Na}_4\text{Co}_3(\text{PO}_4)_2\text{P}_2\text{O}_7$ as a positive electrode and hard carbon (Kureha, battery grade) as a negative electrode. The negative electrode was composed of hard carbon (92.5wt%) and PVdF binder (7.5wt%) on a copper current collector. The battery performance was checked using a charge-discharge machine (BTS2004, Nagano) at a constant current density of 34 mA/g (0.2C) in the voltage range between 3.0 V and 4.8 V.

1.3. Results and discussion

$\text{Na}_4\text{Co}_3(\text{PO}_4)_2\text{P}_2\text{O}_7$ was synthesized by a typical sol-gel method and subsequent heat treatment as described in the Method section. Figure 1.1 a) shows the synchrotron X-ray diffraction and Rietveld refinement patterns of as-prepared material. A small trace (ca. 3 wt.%) of NaCoPO_4 was identified as impurity and the crystal structure of the main product (ca. 97 wt.%) was successfully indexed with space group $Pna2_1$ in an orthorhombic unit cell. Refined atomic position was listed in Table 1 and the fitting was satisfactory ($R_{\text{wp}}=4.65$, $R_{\text{e}}=4.12$ and $S=1.13$). As is also shown in Fig. 1.1 b), as-prepared material had a poly crystal with approximately 3 μm in diameter which was composed of submicron-sized primary particles. Figure 1.2 describes the charge-discharge curves at the 1st, 10th and 50th cycles. The potential limits were set at 3.0 V and 4.7 V vs. Na^+/Na and the current density was at a constant current density of 34 mA/g (0.2C). Here, 1C rate was defined as the current density of 170 mA/g, at which its theoretical capacity (170 mAh/g) can be delivered for an hour. Reversible capacity of $\text{Na}_4\text{Co}_3(\text{PO}_4)_2\text{P}_2\text{O}_7$ reaches ca. 95 mAh/g, corresponding more than half of its theoretical capacity. Inset figure shows the charge-discharge capacity as a function of cycle number. Note that $\text{Na}_4\text{Co}_3(\text{PO}_4)_2\text{P}_2\text{O}_7$ provides the 4.5 V-class highest average potential among ever reported Na^+ intercalation materials, and

the capacity fading is negligible even after 100th cycles.

Figure 1.3 a) shows the cyclic voltammograms (CVs) of $\text{Na}_4\text{Co}_3(\text{PO}_4)_2\text{P}_2\text{O}_7$ at the 2nd and 5th cycles between 3.9 V and 4.8 V vs. Na^+/Na at a sweeping rate of 0.01 mV/s. First redox couple corresponding to Na^+ extraction and insertion was confirmed at 4.26 V and 4.18 V vs. Na^+/Na , respectively. Then, multi redox couples appeared with an increase in the sweeping potential, and the highest redox potential was ca. 4.65 V and 4.62 V vs. Na^+/Na , respectively. No more reversible redox couple was obtained over 4.7 V vs. Na^+/Na , and then an irreversible oxidation current caused by the electrolyte decomposition gradually increased with an increase of the scanning potential up to 4.8 V vs. Na^+/Na . The CV curve at the 5th cycle was perfectly consistent with the 2nd one, which implies that the $\text{Na}_4\text{Co}_3(\text{PO}_4)_2\text{P}_2\text{O}_7$ material will be tough in crystal structure even after electrochemical extraction and insertion of Na^+ . In addition, it should be emphasized that the overpotential of the first redox couple was roughly ± 40 mV, while those of other redox couples were quite small (i.e. ± 10 -20 mV). This result suggests that sodium-ion diffusivity will strongly depends on Na^+ content and distribution in the bulk, and in particular, a fast Na^+ intercalation can be achieved in a specific structure where Na^+ is partially extracted. Olivine LiFePO_4 has only a kind of Li^+ site and a single Li^+ diffusion pathway, and furthermore shows a single redox couple around 3.5 V vs. Li^+/Li . The overpotential of LiFePO_4 was reported to be roughly ± 65 mV¹⁷ at the same scan rate (0.01 mVs⁻¹), which is much larger than that of $\text{Na}_4\text{Co}_3(\text{PO}_4)_2\text{P}_2\text{O}_7$. Herein, it is highly possible that the small overpotential of $\text{Na}_4\text{Co}_3(\text{PO}_4)_2\text{P}_2\text{O}_7$ is delivered by arbitrarily distributed redox potentials in the charge-discharge process, and is also derived from a variety of designed Na^+ sites and flexible diffusion pathways in this unique structure.

Figure 1.3 b) shows the rate capabilities of $\text{Na}_4\text{Co}_3(\text{PO}_4)_2\text{P}_2\text{O}_7$ at different rates of 1700 mA/g (10C), 3400 mA/g (20C) and 4250 mA/g (25C) under the potential limits of 2.0 V and 5.0 V vs.

Na⁺/Na. Surprisingly, the reversible capacity reached ca. 80 mAh/g even at 4250 mA/g. This result verifies that large reversible capacity of ca. 80 mAh/g can be delivered within 70 seconds. More interestingly, the polarization of the charge and discharge reactions, which is related with energy efficiency of the battery, is little enough to maintain the high average potential beyond 4.0 V vs. Na⁺/Na even at 4250 mA/g. As far as we know, no sodium storage material has been reported on the compatibility of high voltage and ultrahigh rate capability. As discussed in the results of the CVs, designed Na⁺ sites and diffusion pathways in the bulk produce the distributed equilibrium redox potentials and fast redox reaction for each potential will occur because of the small overpotentials. We call this new phenomenon “distributed redox reactions”. Although the distributed redox reactions proceed separately at low rates as shown in the CVs, the new type of redox reaction occurs in parallel at high rates and then makes it possible to enhance notably the overall Na⁺ diffusivity in the bulk. This is the first time to propose the parallel diffusion mechanism at high rates, suggesting that Na₄Co₃(PO₄)₂P₂O₇ has great advantages of rapid charge-discharge capability as well as high energy efficiency.

For the future, we will face on a remaining issue which is to increase the reversible capacity in this promising intercalation structure, ultimately close to its theoretical capacity of 170 mAh/g. To achieve the theoretical value, ca. 33% of the initial Co must be oxidized from Co²⁺ through Co³⁺ up to Co⁴⁺ for the charge compensation of 4Na⁺ extraction from Na₄Co₃(PO₄)₂P₂O₇. Now, the reversible capacity of 95 mAh/g at 34 mA/g (0.2C) corresponds to about 2.2 Na⁺ extraction and all the redox reaction is obtained up to 4.8 V vs. Na⁺/Na as shown in the results of the CVs, indicating that Co²⁺/Co³⁺ redox couple will be utilized in the charge-discharge reaction. Herein, the redox couple of Co³⁺/Co⁴⁺ might be observed in the extraordinary high potential region beyond 4.8 V vs. Na⁺/Na. This potential is corresponding to ca. 5.1 V vs. Li⁺/Li at which most of the organic electrolytes in LIBs are well understood to be

unstable. Therefore, a suitable electrolyte having a wide potential window must be developed to activate further redox reaction of $\text{Na}_4\text{Co}_3(\text{PO}_4)_2\text{P}_2\text{O}_7$.

Finally, We constructed the new type of practical sodium-ion battery by combining $\text{Na}_4\text{Co}_3(\text{PO}_4)_2\text{P}_2\text{O}_7$ as a positive electrode and hard carbon^{10,18} instead of Na metal as a negative electrode shown in Figure 1.1S (Supporting information). This battery exhibited the excellent capacity retention of 93% at 50 cycles and retained 4.0 V-class high voltage. The long-term stability strongly implies that the Na^+ intercalation reaction between $\text{Na}_4\text{Co}_3(\text{PO}_4)_2\text{P}_2\text{O}_7$ and hard carbon reversibly occurred. We believe the marked performances of the novel storage material $\text{Na}_4\text{Co}_3(\text{PO}_4)_2\text{P}_2\text{O}_7$ bring a new perspective of sodium-ion batteries for HVs and other large-scale power sources which are requiring high power.

1.4. Conclusions

$\text{Na}_4\text{Co}_3(\text{PO}_4)_2\text{P}_2\text{O}_7$ was successfully prepared by sol-gel method and then heat treatment. The prepared $\text{Na}_4\text{Co}_3(\text{PO}_4)_2\text{P}_2\text{O}_7$ delivers the reversible capacity of 95 mAhg^{-1} , corresponding to ca. 56% of its theoretical capacity, in the high potential region of 4.1-4.7 V vs. Na^+/Na . It should be noted that the reversible capacity retained ca. 84% and the discharge potential maintained above 4.0 V vs. Na^+/Na , suggesting $\text{Na}_4\text{Co}_3(\text{PO}_4)_2\text{P}_2\text{O}_7$ has the compatibility of high rate and potential and therefore should be a promising electrode material for high power batteries.

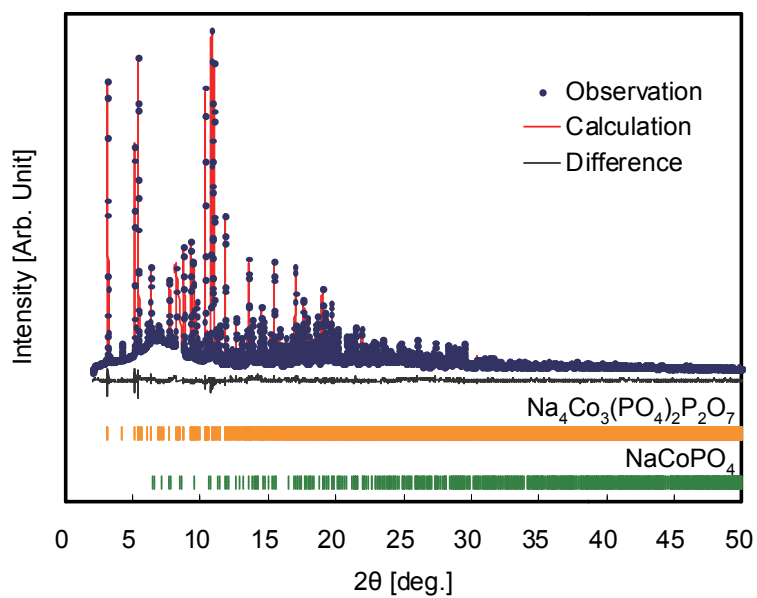
References

1. Tarascon, J-M. & Armand, M. Issues and challenges facing rechargeable lithium batteries. *Nature* **414**, 359-367 (2001).
2. Armand, M. & Tarascon, J-M. Building better batteries. *Nature* **451**, 652-657 (2008).
3. Thackeray, M. An expected conductor. *Nature Mater.* **1**, 81-82 (2002).

4. Yabuuchi, N. *et al.* P2-type $\text{Na}_x[\text{Fe}_{1/2}\text{Mn}_{1/2}]\text{O}_2$ made from earth-abundant elements for rechargeable Na batteries. *Nature Mater.* **11**, 512-517 (2012).
5. Berthelot, R., Carlier, D. & Delmas, C. Electrochemical investigation of the P2- Na_xCoO_2 phase diagram. *Nature Mater.* **10**, 74-80 (2011).
6. Okada, S. *et al.* Layered transition metal oxides as cathodes for sodium secondary battery. *ECS Meeting Abstract* **602**, 201 (2006).
7. Recham, N. *et al.* Ionothermal Synthesis of Sodium-Based Fluorophosphate Cathode Materials. *J. Electrochem. Soc.* **156**, A993-A999 (2009).
8. Kawabe, Y. *et al.* Synthesis and electrode performance of carbon coated $\text{Na}_2\text{FePO}_4\text{F}$ for rechargeable Na batteries. *Electrochem. Commun.* **13**, 1225-1228 (2011).
9. Barker, J., Saidi, M-Y. & Swoyer, J-L. A Sodium-Ion Cell Based on the Fluorophosphate Compound NaVPO_4F BATTERIES AND ENERGY CONVERSION. *Electrochem. Solid-state Lett.* **6**, (1) A1-A4 (2003).
10. Stevensa, D-A & Dahn, J-R. High Capacity Anode Materials for Rechargeable Sodium-Ion Batteries. *J. Electrochem. Soc.* **147**, (4) 1271-1273 (2000).
11. Senguttuvan, P. *et al.* $\text{Na}_2\text{Ti}_3\text{O}_7$: Lowest Voltage Ever Reported Oxide Insertion Electrode for Sodium Ion Batteries. *Chem. Mater.* **23**, 4109-4111 (2011).
12. Trinh, N-D. *et al.* Synthesis, Characterization and Electrochemical Studies of Active Materials for Sodium Ion Batteries. *ECS Transaction* **35**, (32) 91-98 (2011).
13. Zhao, L. *et al.* Spinel lithium titanate ($\text{Li}_4\text{Ti}_5\text{O}_{12}$) as novel anode material for room-temperature sodium-ion battery. *Chin. Phys. B.* **21**, 028201/1-028201/4 (2012).
14. Ceder, G. *et al.* Voltage, stability and diffusion barrier differences between sodium-ion and lithium-ion intercalation materials. *The Royal Society of Chemistry* **4**, 3680-3688 (2011).
15. Nishimura, S. *et al.* Experimental visualization of lithium diffusion in Li_xFePO_4 . *Nature*

- Mater.* **7**, 707-711 (2008).
16. Sanz, F. *et al.* $\text{Na}_4\text{Co}_3(\text{PO}_4)_2\text{P}_2\text{O}_7$, a New Sodium Cobalt Phosphate Containing a Three-Dimensional System of Large Intersecting Tunnels. *J. Solid State Chem.* **123**, 129-139 (1996).
 17. Shin, H-C. *et al.* Electrochemical properties of the carbon-coated LiFePO_4 as a cathode material for lithium-ion secondary batteries. *Journal of Power Sources* **159**, 1383-1388 (2006).
 18. Franklin, R-E. Crystallite growth in graphitizing and non graphitizing carbons. *Mathematical, Physical and Engineering Sciences* 209, 196-218 (1951).
 19. Momma, K. & Izumi, F. VESTA: A three-dimensional visualization system for electronic and structural analysis. *J. Appl. Crystallogr.* **41**, 653-658 (2008).

a)



b)

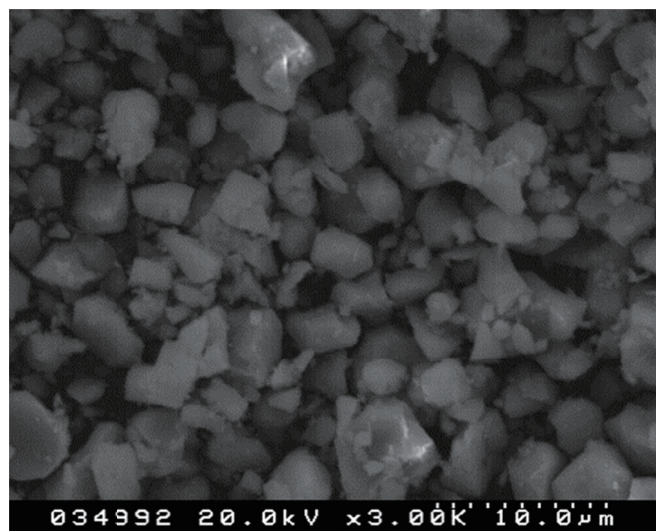


Fig. 1.1 a) Synchrotron X-ray diffraction (SXR) pattern with Rietveld refinement ($R_{wp}=4.65$, $R_e=4.12$ and $S=1.13$) and b) Field Emission-Scanning Electron Microscope image of as-prepared material by sol-gel method.

Table 1. Refined atomic position of $\text{Na}_4\text{Co}_3(\text{PO}_4)_2\text{P}_2\text{O}_7$ prepared by sol-gel method.

Atom	x	y	z	Temperature factor	Occupancy
Co1	0.165882	0.001119	0.065193	0.476245	1
Co2	0.139602	0.496585	0.075731	0.476245	1
Co3	0.242193	0.743234	0.340020	0.476245	1
P1	0.291850	0.505839	0.070747	0.507858	1
P2	0.178459	0.483649	0.578900	0.507858	1
P3	0.067100	0.761959	0.214258	0.507858	1
P4	0.051228	0.226223	0.021501	0.507858	1
Na1	0.008364	0.474512	0.347000	1.019240	1
Na2	0.202646	0.243003	0.320923	1.019240	1
Na3	0.392145	0.257201	0.236307	1.019240	1
Na4	0.038439	0.044765	0.494152	1.019240	1
O1	0.236034	0.617318	0.106533	0.343498	1
O2	0.342934	0.480567	0.251843	0.343498	1
O3	0.162665	0.042533	0.394989	0.343498	1
O4	0.241569	0.390222	0.040431	0.343498	1
O5	0.267034	0.105406	0.084495	0.343498	1
O6	0.373722	0.000061	0.252855	0.343498	1
O7	0.232002	0.373520	0.625618	0.343498	1
O8	0.134018	0.465419	0.376536	0.343498	1
O9	0.011325	0.205608	0.808562	0.343498	1
O10	0.060929	0.636025	0.100811	0.343498	1
O11	0.123325	0.770136	0.384984	0.343498	1
O12	0.415337	0.368506	0.569403	0.343498	1
O13	0.043135	0.369305	0.060502	0.343498	1
O14	0.132859	0.186347	0.000000	0.343498	1
O15	0.010615	0.140107	0.178696	0.343498	1

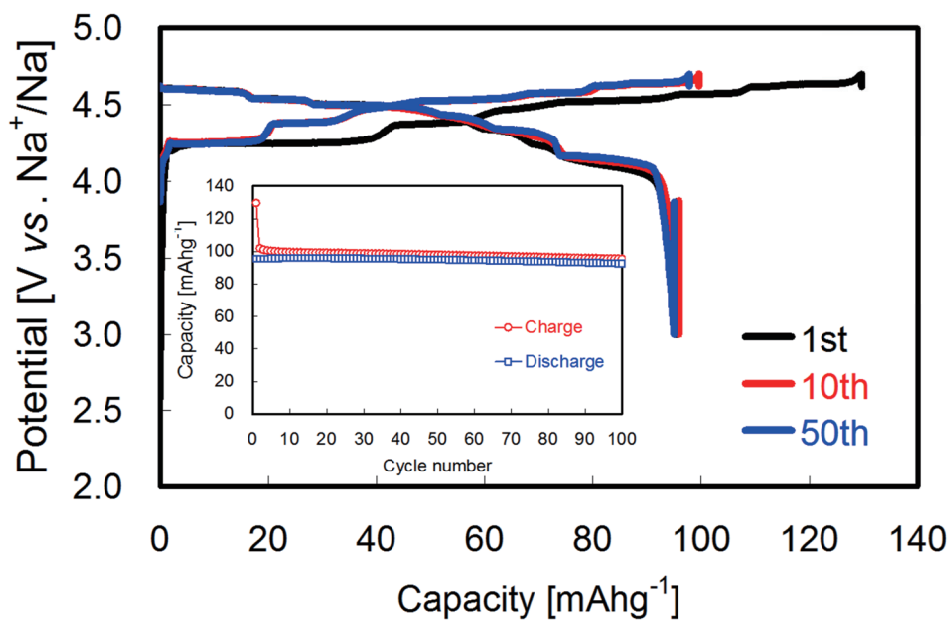
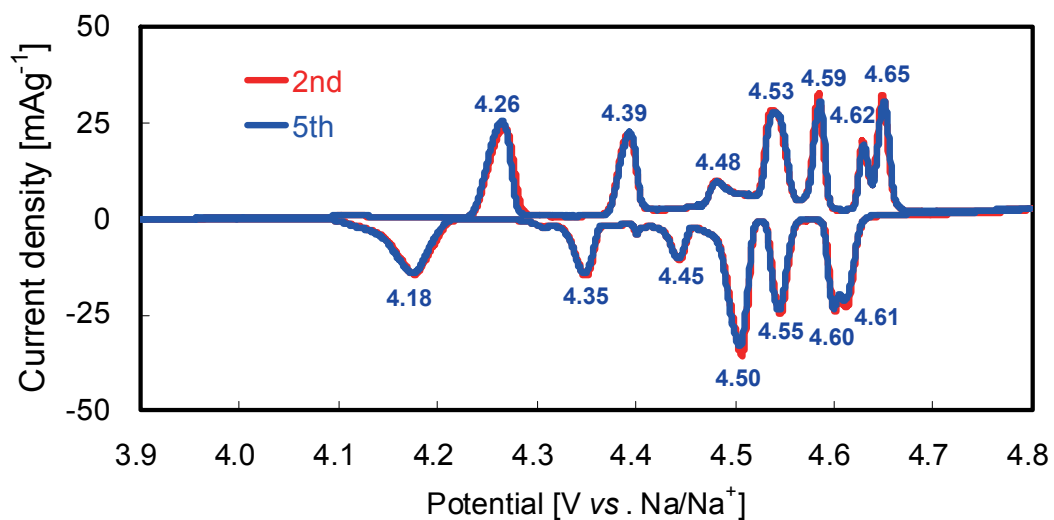


Fig. 1.2 Galvanostatic charge-discharge curves at 1st, 10th and 50th cycles and charge-discharge capacities as a function of cycle number of $\text{Na}_4\text{Co}_3(\text{PO}_4)_2\text{P}_2\text{O}_7$.

a)



b)

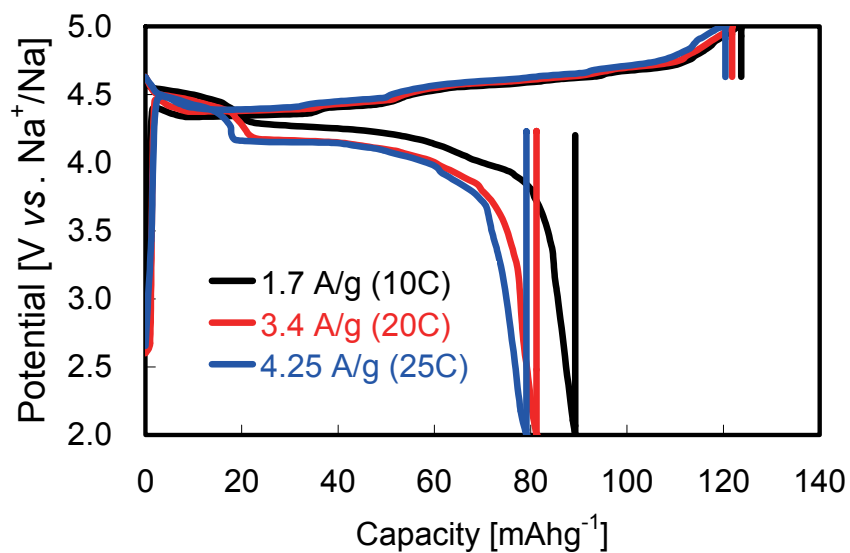
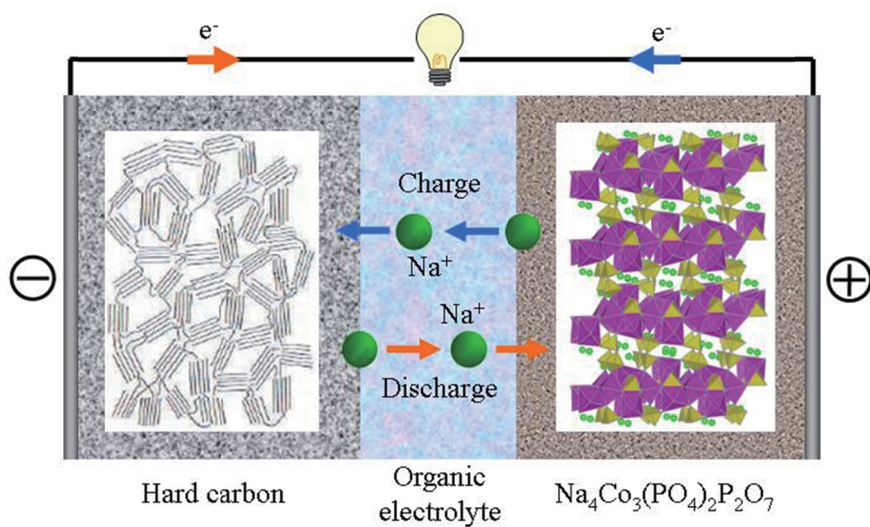


Fig. 1.3 a) 2nd and 5th cyclic voltammograms at the scan rate of 0.01 mV/sec in the potential range of 3.9 V and 4.8 V vs. Na⁺/Na and b) rate capabilities at 1.7 A/g (10C), 3.4 A/g (20C) and 4.25 A/g (25C) rates.

a)



b)

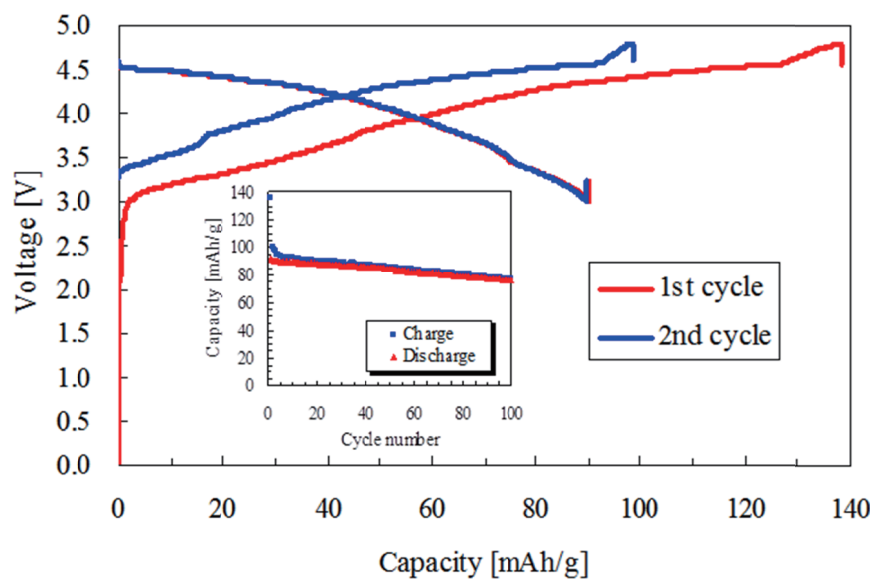


Fig. 1.1S a) Schematic image of new battery assembled by Na₄Co₃(PO₄)₂P₂O₇ and hard carbon as a positive and negative electrode, respectively and b) charge and discharge curves at 1st and 2nd cycle at the current density of 34 mA/g.

Chapter II

Structural and Electrical Analysis of $\text{Na}_4\text{Co}_3(\text{PO}_4)_2\text{P}_2\text{O}_7$ during Electrochemically Na^+ Extraction/Insertion

2.1. Introduction

Lithium-ion batteries (LIBs) are widely used as energy storage devices for mobile electronics (e.g., mobile phones, laptops, digital cameras) because of their high energy density, light weight, and good durability. Recently, LIBs have been scaled up to serve as power sources in electric vehicles, and are also being developed for use in energy storage systems for intermittent power generators such as wind turbines, solar panels, and so on. For these large-scale applications, however, the high cost and limited availability of lithium resources is a serious concern. Because sodium is much higher in abundance than lithium with vast terrestrial reserves over the last decade sodium-ion batteries (SIBs) have rapidly gained interest as an attractive alternative to LIBs [1-5].

Numerous sodium-containing materials have already been investigated for use as positive [1-9] and negative electrodes [1-5, 10-14] in SIBs. The richer chemical and structural phase space of Na-containing systems compared to their Li counterparts is another promising feature of SIBs, because in order to develop viable high performance SIBs that can compete with LIBs, Na cathode materials need to be found that exhibit both high cell potentials and high Na-ion diffusivity.

Recently, the author et al. reported high voltages and high rate behavior of SIBs that use

$\text{Na}_4\text{Co}_3(\text{PO}_4)_2\text{P}_2\text{O}_7$ as the cathode material [15]. This material has a complex crystal structure, as shown in Fig. 1 (all crystal structure representations in this paper were drawn using VESTA [16]). X-ray diffraction studies of $\text{Na}_4M_3(\text{PO}_4)_2\text{P}_2\text{O}_7$ ($M=\text{Co}, \text{Ni}, \text{Mn}, \text{Mg}$ or Fe) have shown that this family of compounds has a common structure type belonging to space group $Pna21$ (no. 33). The structure consists of $M_3\text{P}_2\text{O}_{13}$ sheets parallel to the bc plane linked by P_2O_7 units parallel to the a axis to form an open framework with large interconnected channels in which the Na ions sit [17, 18]. There are four crystallographically distinct Na sites as indicated in Fig. 1. Na1 and Na4 sites are 6-fold coordinated to oxygen, while Na2 and Na3 sites have 7-fold coordination. The large channels enable long-range Na-ion migration to occur with a low activation energy, making $\text{Na}_4\text{Co}_3(\text{PO}_4)_2\text{P}_2\text{O}_7$ a good 3D ion conductor [19]. This is advantageous vis-à-vis 1D conductors because even if some channels are blocked, for example, by crystalline defects, other pathways will still be available to allow Na insertion/extraction into/from the cathode.

Electrochemical properties of $\text{Na}_4\text{Co}_3(\text{PO}_4)_2\text{P}_2\text{O}_7$ have been reported by the author et al.[15]. We showed that this material displays excellent rate performance and has a relatively high battery voltage (close to 5 V) compared to other Na-ion cathode materials. However, the battery capacity is rather low, and it was found that $\text{Na}_x\text{Co}_3(\text{PO}_4)_2\text{P}_2\text{O}_7$ cannot be fully desodiated, with the lowest Na content that could be obtained being $x=1$. In order to understand and improve the performance of this material further, a detailed understanding of the desodiation mechanism is desirable. Computer modeling provides an efficient, systematic means of obtaining such information with a high degree of precision[20]. In this study we probe the atomistic and electronic changes occurring in $\text{Na}_x\text{Co}_3(\text{PO}_4)_2\text{P}_2\text{O}_7$ ($0 < x < 4$) during the charge/discharge process at a fundamental level using first-principles techniques. The next section outlines the methodology used, while results are presented and discussed in section 2.3, and the main conclusions summarized in section 2.4.

2.2 Methodology

First-principles calculations were performed using the projector-augmented wave (PAW) method [21] within the framework of density functional theory (DFT) [22,23], as implemented in the VASP code [24,25]. Exchange-correlation interactions were treated by the generalized gradient approximation (GGA-PBE) [26]. On-site Coulomb repulsion was treated using the GGA+ U method [27]. We used a Hubbard effective charge of $U_{\text{eff}}=5.0\text{eV}$ for Co3 d electrons. For the PAW potentials, 2 p and 3 s for Na, 3 d and 4 s for Co, 3 s and 3 p for P, and 2 s and 2 p for O were explicitly treated as valence electrons. Plane wave expansion was performed up to 500 eV. A $2\times 2\times 3$ k -point mesh, based on the Monkhorst-Pack scheme [28], was used for Brillouin zone sampling of primitive cells containing 104 atoms. Calculated errors were estimated to be below 2meV per $\text{Na}_4\text{Co}_3(\text{PO}_4)_2\text{P}_2\text{O}_7$ formula unit. Lattice constants and internal atomic coordinates were considered fully optimized when residual Hellmann-Feynman (HF) forces were smaller than 1.0×10^{-3} eV/Å. For simplicity, all spin configurations were considered to be ferromagnetic.

2.3 Results and discussion

2.3.1. Crystal and electronic structure of $\text{Na}_4\text{Co}_3(\text{PO}_4)_2\text{P}_2\text{O}_7$

Our calculations reproduced the reported experimental lattice parameters [16] of the $\text{Na}_4\text{Co}_3(\text{PO}_4)_2\text{P}_2\text{O}_7$ unit cell (Fig. 1) to within the usual DFT error. Bond lengths and bond angles are also well reproduced.

Figure 2 shows the calculated density of states (DOS) of $\text{Na}_4\text{Co}_3(\text{PO}_4)_2\text{P}_2\text{O}_7$. The valence bands consist mainly of Co3 d and O2 p orbitals, indicating that there is some hybridization between these two types of orbital. In contrast, Na makes a negligibly small contribution to the valence bands. In chemical terms, Co and O form strong covalent bonds, with the O atoms also

linked to P to form PO₄ (and P₂O₇) polyhedral, resulting in a robust framework structure. Co²⁺ ions exist in a high spin state with $s = 3/2$ (3 μ B), with a Hubbard gap between the minority spin Co3d t_{2g} orbitals, as seen in Fig. 2. Na⁺ ions within the large channels form essentially ionic bonds with their oxygen nearest neighbors.

2.3.2 Initial desodiation step

The desodiation process was examined by systematically removing Na atoms from sites in the unit cell to maintain *Pna21* symmetry. In other words, desodiation was assumed to occur as a four-step process, with all atoms of a particular coordination environment removed at each step (partial occupation of crystallographic sites was not considered). For each step, once one of the four Na sites was made vacant the structure was relaxed to its local energy minimum. The structure with the lowest energy, i.e., most stable structure, was used to identify the site from which Na would be removed during that step, and this structure was then taken as the starting point for the next desodiation step.

For the first step, one quarter of the Na atoms were removed from the unit cell. Figure 3 shows the calculated battery voltages relative to Na metal (Na/Na⁺) for each site type, with 7-coordinated and 6-coordinated sites indicated by orange and blue labels, respectively. The lowest battery voltage of 4.05V was calculated for vacant Na2 sites. Removal of Na from 7-fold Na sites produced lower battery voltages (Na2 site: 4.05 V and Na3 site: 4.17V) than from the 6-fold sites (Na1 site: 4.39 V and Na4 site: 4.35 V). This can be rationalized by noting that the average bond strength of the former two sites is weaker than the latter two sites. In any case, regardless of which site is made vacant, the calculated battery voltage relative to Na metal is always over 4 V, which is high for a cathode material.

Plots of the full and partial DOS of Na₃Co₃(PO₄)₂P₂O₇ are shown in Fig.4. Detailed analysis

revealed that during the first desodiation step one-third of the Co^{2+} ions are oxidized to Co^{3+} , and Co^{3+} ions with their $3d^6$ electron configuration are stabilized in a high spin state by the highly distorted oxygen octahedral in which they lie. The band gap decreases substantially, from an initial value of 3.05eV for $\text{Na}_4\text{Co}_3(\text{PO}_4)_2\text{P}_2\text{O}_7$ down to 1.5eV, closer to that of a typical semiconductor.

2.3.3 Subsequent desodiation steps

The second desodiation step (from $\text{Na}_3\text{Co}_3(\text{PO}_4)_2\text{P}_2\text{O}_7$ to $\text{Na}_2\text{Co}_3(\text{PO}_4)_2\text{P}_2\text{O}_7$) was examined in a similar manner to the first desodiation step (from $\text{Na}_4\text{Co}_3(\text{PO}_4)_2\text{P}_2\text{O}_7$ to $\text{Na}_3\text{Co}_3(\text{PO}_4)_2\text{P}_2\text{O}_7$). Of the remaining Na ions, removal of Na from Na1 sites produced not only the lowest energy structure, but also the lowest voltage (4.33 V). This is slightly lower than for removal of Na from Na1 sites in the first desodiation step. This voltage change can be attributed to the change in local structure (relaxation) around Na vacancies after the first desodiation step. This indicates that battery voltage is affected not only by the number of coordinating O ions of the Na site from which they are removed, but also by distortion of the local bonding environment. After the second desodiation step, two-thirds of Co^{2+} ions are oxidized to Co^{3+} , with all Co^{3+} ions in high spin states.

The second desodiation step was followed by a third desodiation step from $\text{Na}_2\text{Co}_3(\text{PO}_4)_2\text{P}_2\text{O}_7$ to $\text{NaCo}_3(\text{PO}_4)_2\text{P}_2\text{O}_7$. In this case, removal of Na ions from Na4 sites was found to be the most energetically favorable. This produced a material with a battery voltage of 4.81V, a large increase compared to the desodiation from the Na1 site in the previous step. Removal of sodium has a similar effect on the electronic structure as in previous steps, with the remaining Co^{2+} ions oxidized to Co^{3+} . As there are only three Co ions per formula unit, no further Co^{2+} ions are available to facilitate a fourth desodiation step.

In the final step, Na ions were removed from Na3 sites, leaving all Na sites empty. The DOS of the desodiated $\text{Co}_3(\text{PO}_4)_2\text{P}_2\text{O}_7$ compound is shown in Fig.6. After this final step, new empty states appear in the bandgap. These states are mainly composed of O2*p* orbitals rather than Co3*d* orbitals, indicating that when the last Na ion is removed all Co ions remain as Co^{3+} rather than some being oxidized to Co^{4+} ; instead, electrons are removed from O2*p* orbitals.

If we assume a two-phase reaction as suggested from experiment [14], the battery voltages during charging can be plotted as a function of Na content as shown in Fig.7. As Na is removed, the battery voltage increases stepwise over the entire charge process from 4.3 to 4.8 V. This multi-plateau voltage plot qualitatively reproduces the experimentally observed charge-discharge behavior of this compound [16]. Discrepancies between the calculated results and experimental results can be attributed to the size constraints imposed by limiting our calculations to a single unit cell (and ignoring the possibility of partial or mixed occupation of Na sites).

Calculated lattice parameter changes during the desodiation process are summarized in Fig.8. As Na is removed from $\text{Na}_4\text{Co}_3(\text{PO}_4)_2\text{P}_2\text{O}_7$ to $\text{NaCo}_3(\text{PO}_4)_2\text{P}_2\text{O}_7$, the *a* and *c* parameters contract by about 3%, while the *b* parameter lengthens by about 2%. In contrast, during the final desodiation step from $\text{NaCo}_3(\text{PO}_4)_2\text{P}_2\text{O}_7$ to $\text{Co}_3(\text{PO}_4)_2\text{P}_2\text{O}_7$, there is a marked, discontinuous change in the structure parameters, with the *c* parameter shrinking by about 3%, and the *a* parameter elongating by about 6% in a single step. Figure 9 highlights the change in crystal structure during the desodiation process by comparing the unit cell structures of $\text{Na}_4\text{Co}_3(\text{PO}_4)_2\text{P}_2\text{O}_7$ and $\text{Co}_3(\text{PO}_4)_2\text{P}_2\text{O}_7$. This shows that the discontinuous changes in lattice parameters is associated with a large contraction of the Na channels upon removal of the last Na ions. This contraction also blocks the Na diffusion paths, which may explain why in practice it is found very difficult to remove all Na from this compound. Because the channel network

remains intact down to $x=1$, charging and discharging the cathode within compositional limits $1 < x < 4$ can be expected to favor reversible Na ion extraction and insertion, and thus good cycling performance, as has been observed experimentally [16].

Also, the increase in battery voltage between the third desodiation (Na1 site) and fourth desodiation (Na2 site) step is only 0.2 V. Even without this small increase, the voltage of the fully charged cathode is close to the decomposition voltage of common electrolytes (around 5V), in excellent agreement with experiment [16].

Oxidation of Co^{3+} to Co^{4+} is known to occur in some LIB and SIB cathode materials. For example, in LiCoO_2 and NaCoO_2 , Co^{3+} is oxidized to Co^{4+} during delithiation. The difference with the present material can be attributed to differences in the local structures around Co ions and their spin states. In LiCoO_2 , Co^{3+} ion sit within smaller, symmetrical CoO_6 octahedral (Co-O bond length $\sim 1.94\text{\AA}$), and are in a low spin state (with small ionic radius), and is antiferromagnetic in its ground state. The compact coordination allows the smaller Co^{4+} ion to be stabilized, although its inherent chemical instability leads to crystal fatigue after repeated cycling [29]. In contrast, in $\text{Na}_4\text{Co}_3(\text{PO}_4)_2\text{P}_2\text{O}_7$, Co ions are located within large, distorted CoO_6 octahedral (Co-O bond lengths $\sim 2.041\text{-}2.656\text{\AA}$) and are in a high spin state with a larger ionic radius. The differences in coordination environments are illustrated in Fig. 10 along with schematic orbital energy diagrams of the two compounds. The orbital energy diagrams show that, unlike in LiCoO_2 , only three $\text{Co}3d$ electrons in $\text{Na}_4\text{Co}_3(\text{PO}_4)_2\text{P}_2\text{O}_7$ are shared with the $\text{O}2p$ orbitals, so that much more energy would be required to remove a fourth, deeper energy electron to form Co^{4+} . Consequently the fourth electron is removed from $\text{O}2p$ orbitals alone instead. One consequence of this is that the phosphate-containing system exhibits superior cycling performance than layered cobalt oxide because the 3D framework retains its structural integrity.

2.4 Conclusions

Density functional theory calculations using the GGA+*U* method were performed to evaluate the theoretical battery voltage and crystal and electronic structure changes during charging and discharging of sodium-ion battery cathode material $\text{Na}_x\text{Co}_3(\text{PO}_4)_2\text{P}_2\text{O}_7$ ($x=0$ to 4).

The main findings can be summarized as follows:

- 1) The battery voltage changes from 4.05 to 4.95 V as a function of charge state. Below an Na content of $x=1$, the battery voltage has a value close to the decomposition voltage (around 5.0 V) of typical liquid electrolytes.
- 2) During desodiation of $\text{Na}_4\text{Co}_3(\text{PO}_4)_2\text{P}_2\text{O}_7$ to $\text{NaCo}_3(\text{PO}_4)_2\text{P}_2\text{O}_7$, all three Co^{2+} ions per formula unit are oxidized to Co^{3+} .
- 3) When charging / discharging within compositional range $1 < x < 4$, lattice parameters change by less than 3 %, consistent with the good cyclability of this material.
- 4) During the last desodiation step from $\text{NaCo}_3(\text{PO}_4)_2\text{P}_2\text{O}_7$ to $\text{Co}_3(\text{PO}_4)_2\text{P}_2\text{O}_7$, electrons are removed from O orbitals rather than Co orbitals, so that all three Co ions per formula unit remain trivalent. Simultaneously, a discontinuous structure change associated with Na channel contraction occurs. These two factors may explain the difficulty of desodiating $\text{NaCo}_3(\text{PO}_4)_2\text{P}_2\text{O}_7$ to $\text{Co}_3(\text{PO}_4)_2\text{P}_2\text{O}_7$ found experimentally.

References

1. S.-W. Kim, D.-H. Seo, X. Ma, G. Ceder, K. Kang, *Adv. Energy Mater.* **2** (2012) 710–721.
2. V. Palomares, M. Casas-Cabanas, E. Castillo-Martínez, M.H. Han, T. Rojo, *Energy Environ. Sci.* **6** (2013) 2312-2337.
3. H. Pan, Y.-S. Hu, L. Chen, *Energy Environ. Sci.* **6** (2013) 2338-2360.

4. M. D. Slater, D. Kim, E. Lee, C.S. Johnson, *Adv. Funct. Mater.* **23** (2013) 947–958.
5. L. P. Wang, L. Yu, X. Wang, M. Srinivasan, Z. J. Xu, *J. Mater. Chem. A* **3** (2015) 9353-9378.
6. M. H. Han, E. Gonzalo, G. Singh, T. Rojo, *Energy Environ. Sci.* **8** (2015) 81-102.
7. M. Sathiya, K. Hemalatha, K. Ramesha, J.M. Tarascon, A.S. Parkash, *Chem. Mater.* **24** (2012) 1846-1853.
8. N. Yabuuchi, M. Kajiyama, J. Iwatate, H. Nishikawa, S. Hitomi, R. Okuyama, R. Usui, Y. Yamada, S. Komaba, *Nature Mater.* **11** (2012) 512-517.
9. X. Liu, X. Wang, A. Iyo, H. Yu, D. Lia, H. Zhou, *J. Mater. Chem. A* **2** (2014) 14822-14826.
14
10. M. Shirpour, J. Cabana, M. Doeff, *Energy Environ. Sci.* **6** (2013) 2538-2547.
11. H. Kim, I. Park, D.H. Seo, S. Lee, S.-W. Kim, W.J. Kwon, Y.U. Park, C.S. Kim, S. Jeon, K. Kang, *J. Am. Chem. Soc.* **134** (2012) 10369-10372.
12. K. Gotoh, T. Ishikawa, S. Shimadzu, N. Yabuuchi, S. Komaba, K. Takeda, A. Goto, K. Deguchi, S. Ohki, K. Hashi, T. Shimizu, H. Ishida, *J. Power Sources* **225** (2013) 137-140.
13. P. Senguttuvan, G. Rousse, V. Seznec, J.-M. Tarascon, M.R. Palacín, *Chem. Mater.* **23** (2011) 4109-4111.
14. G. Hasegawa, K. Kanamori, T. Kiyomura, H. Kurata, K. Nakanishi, T. Abe, *Adv. Energy Mater.* **5** (2015) 1400730.
15. M. Nose, H. Nakayama, K. Nobuhara, H. Yamaguchi, S. Nakanishi, H. Iba, *J. Power Sources* **234** (2013) 175-179.
16. K. Momma, F. Izumi, *J. Appl. Crystallogr.* **41**(2008) 653.
17. F. Sanz, C. Parada, U. Amador, M.A. Monge, C. Ruiz-Valero, *J. Solid State Chem.* **123** (1996) 129-139.

18. F. Sanz, C. Parada, J.M. Rojo, C. Ruiz-Valero, Chem. Mater. **13** (2001) 1334-1340.
19. S. M. Wood, C. Eames, E. Kendrick, M. S. Islam, J. Phys. Chem. C **119** (2015) 15 15935–15941.
20. M. S. Islam, C. A. J. Fisher, Chem. Soc. Rev. **43** (2014) 185-204.
21. P. E. Blöchl, Phys. Rev. B **50** (1994) 17953.
22. P. Hohenberg, W. Kohn, Phys. Rev. **136** (1964) B864.
23. W. Kohn, L. J. Sham, Phys. Rev. **140** (1965) A1133.
24. G. Kresse, J. Furthmüller, Phys. Rev. B **54** (1996) 11169.
25. G. Kresse, D. Joubert, Phys. Rev. B **59** (1999) 1758.
26. J. P. Perdew, K. Burke, M. Ernzerhof, Phys. Rev. Lett. **77** 3865 (1996)
27. S. L. Dudarev, G. A. Botton, S. Y. Savrasov, C. J. Humphreys, A. P. Sutton, Phys. Rev. B **57** 1505 (1998).
28. H. J. Monkhorst, J. D. Pack, Phys. Rev. B **13** (1976) 5188.
29. J. Geder, J. H. Song, S. H. Kang, D. Y. W. Yu, Solid State Ionics **268** (2014) 242-246.

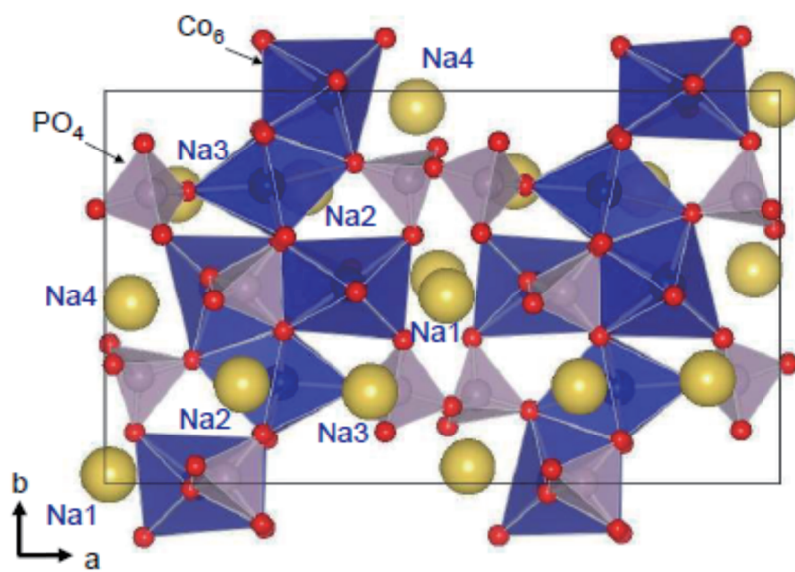


Fig. 2.1 Unit cell of $\text{Na}_4\text{Co}_3(\text{PO}_4)_2\text{P}_2\text{O}_7$ (S.G. $Pna2_1$) showing CoO_6 octahedral and PO_4 tetrahedral. Large yellow balls are Na, blue balls are Co, gray balls are P and small red balls are oxygen.

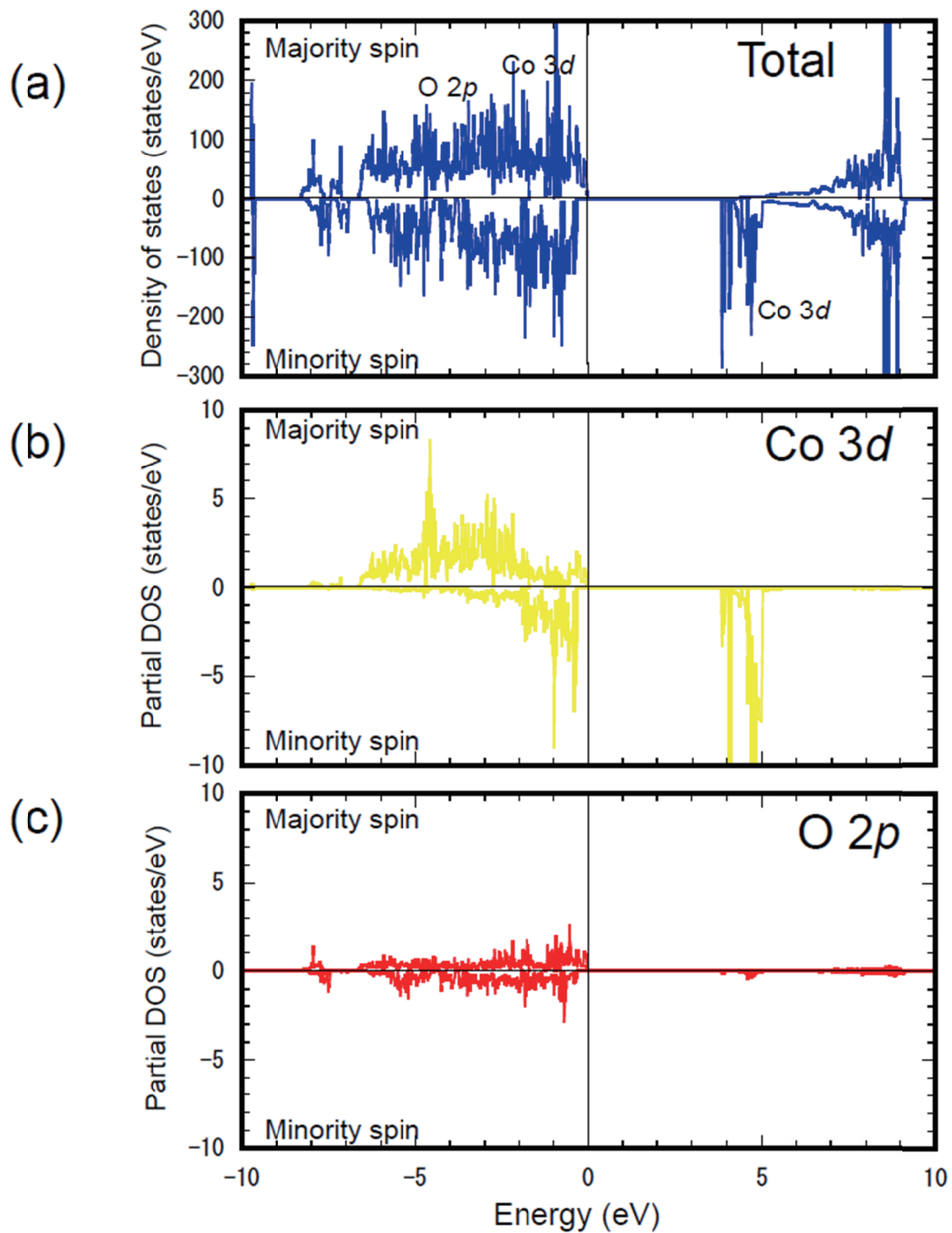


Fig. 2.2 Electric structure of $\text{Na}_4\text{Co}_3(\text{PO}_4)_2\text{P}_2\text{O}_7$: (a) Total density of states (DOS); partially density of states of (b) $\text{Co}3d$ electrons and (c) $\text{O}2p$ electrons.

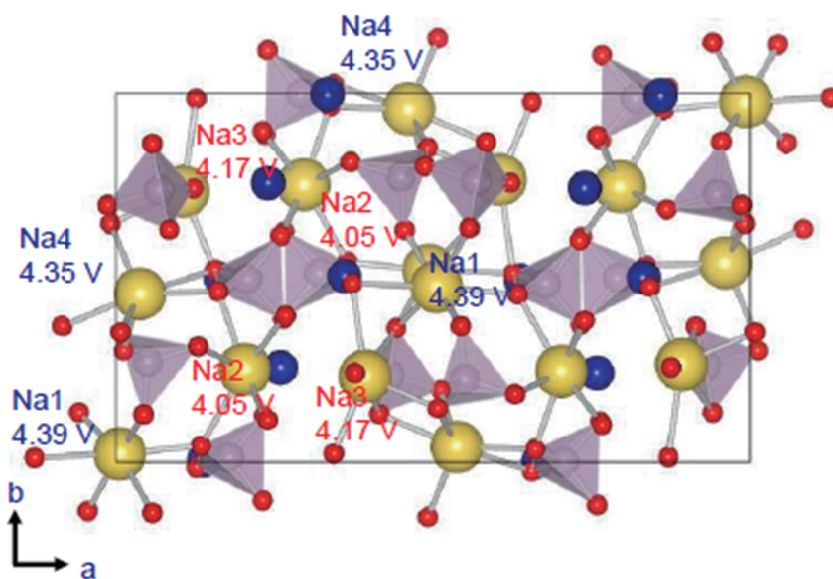


Fig. 2.3 Calculated battery voltages after desodiation of $\text{Na}_4\text{Co}_3(\text{PO}_4)_2\text{P}_2\text{O}_7$ to $\text{Na}_3\text{O}_3(\text{PO}_4)_2\text{P}_2\text{O}_7$ using the same atom representations as Fig. 2.1. Orange labels indicate 7-coordinated sites and blue labels 6-coordinated sites.

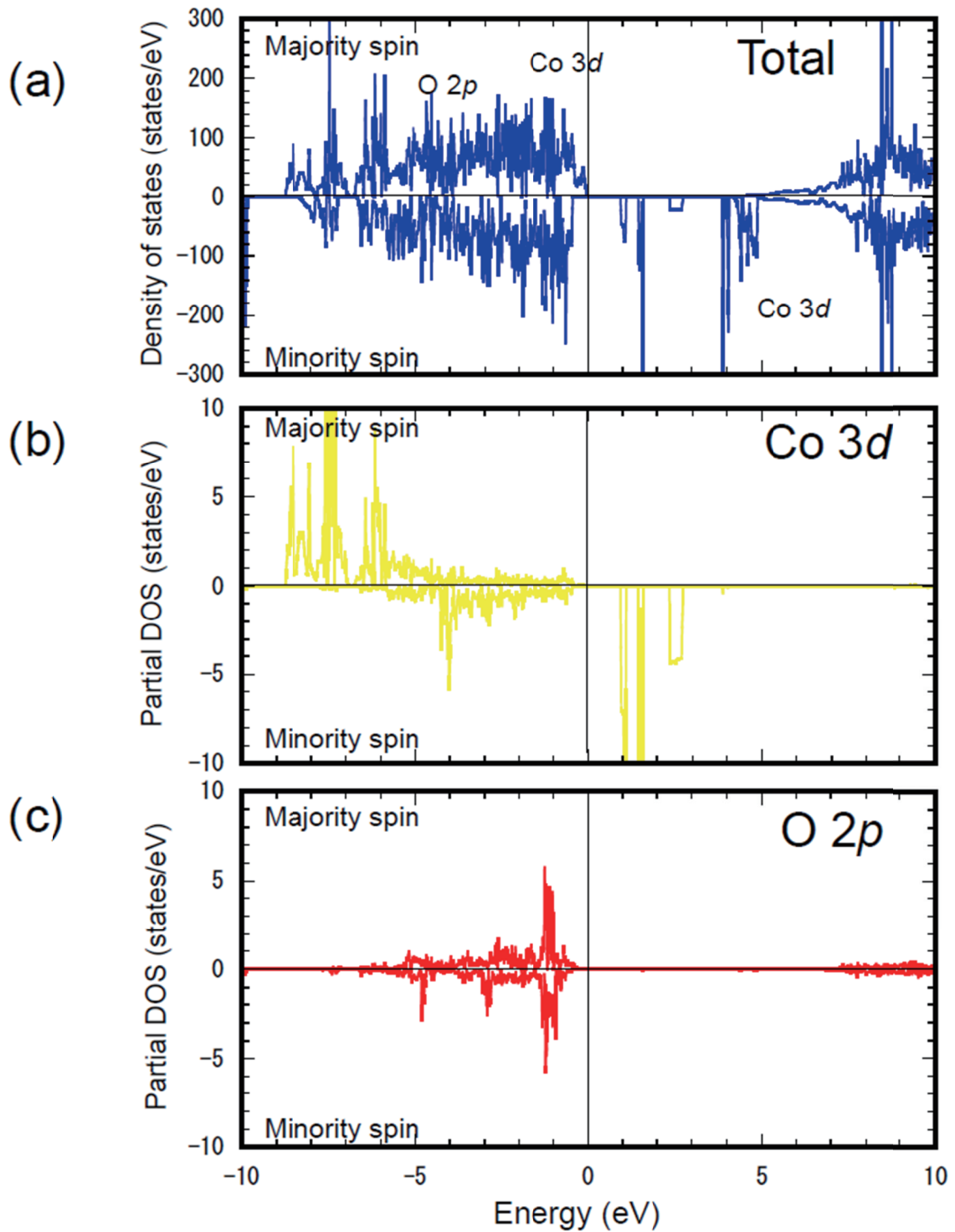


Fig. 2.4 Electric structure of $\text{Na}_3\text{Co}_3(\text{PO}_4)_2\text{P}_2\text{O}_7$: (a) Total density of states (DOS); partially density of states of (b) $\text{Co}3d$ electrons and (c) $\text{O}2p$ electrons.

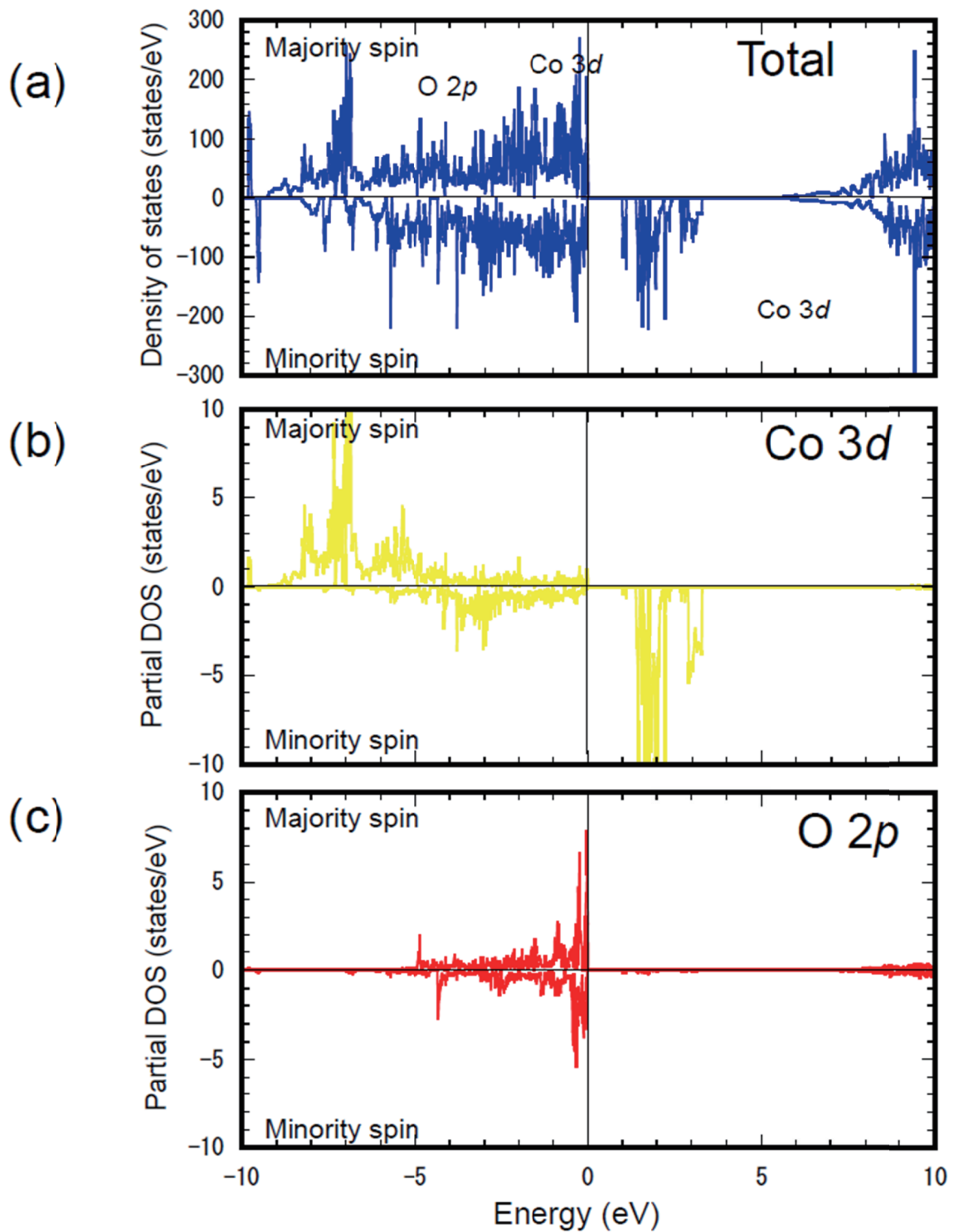


Fig. 2.5 Electric structure of $\text{NaCo}_3(\text{PO}_4)_2\text{P}_2\text{O}_7$: (a) Total density of states (DOS); partially density of states of (b) $\text{Co}3d$ electrons and (c) $\text{O}2p$ electrons.

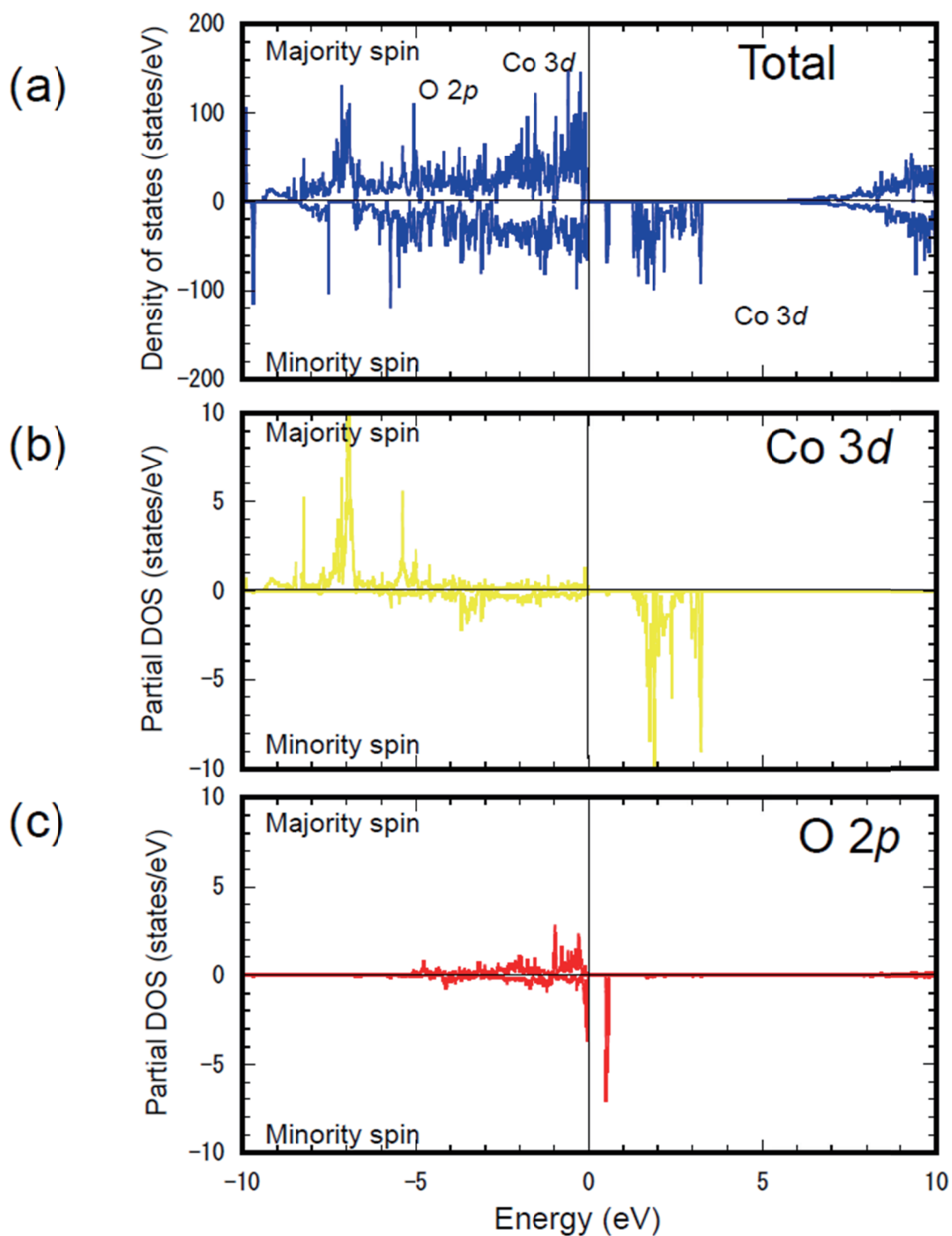


Fig. 2.6 Electric structure of $\text{Co}_3(\text{PO}_4)_2\text{P}_2\text{O}_7$: (a) Total density of states (DOS); partially density of states of (b) $\text{Co}3d$ electrons and (c) $\text{O}2p$ electrons.

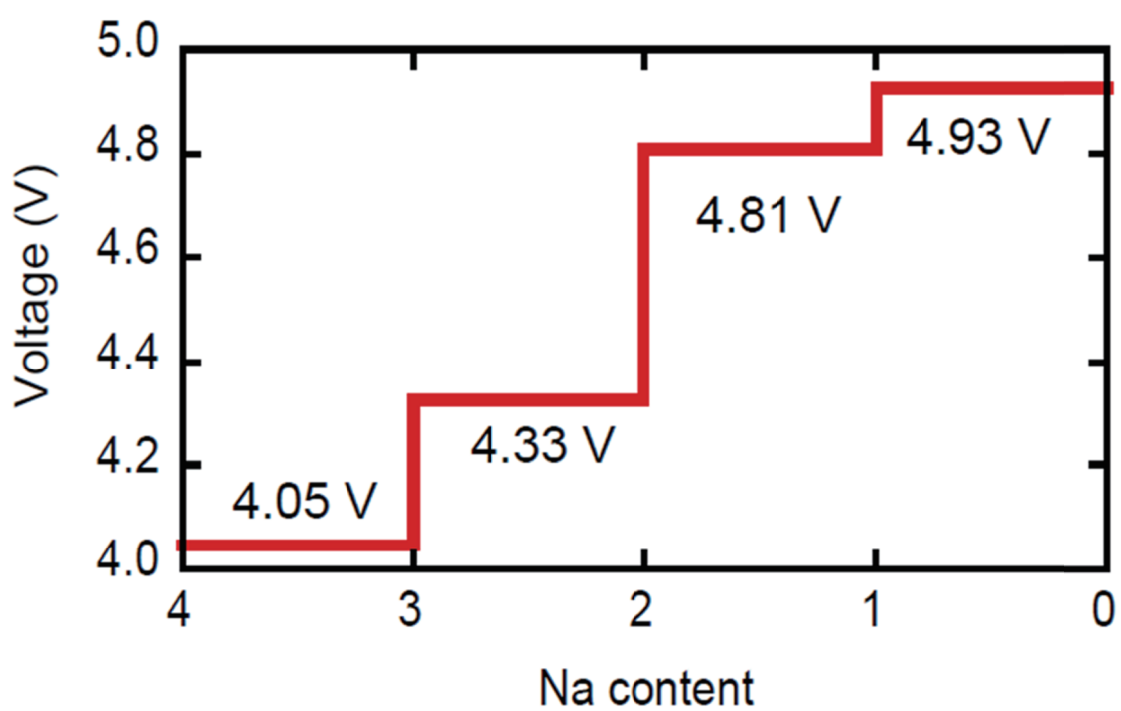


Fig. 2.7 Battery voltages during desodiation of $\text{Na}_4\text{Co}_3(\text{PO}_4)_2\text{P}_2\text{O}_7$ assuming a two phase reaction. Voltage increase stepwise from 4.05 V to 4.93 V as Na atoms are removed.

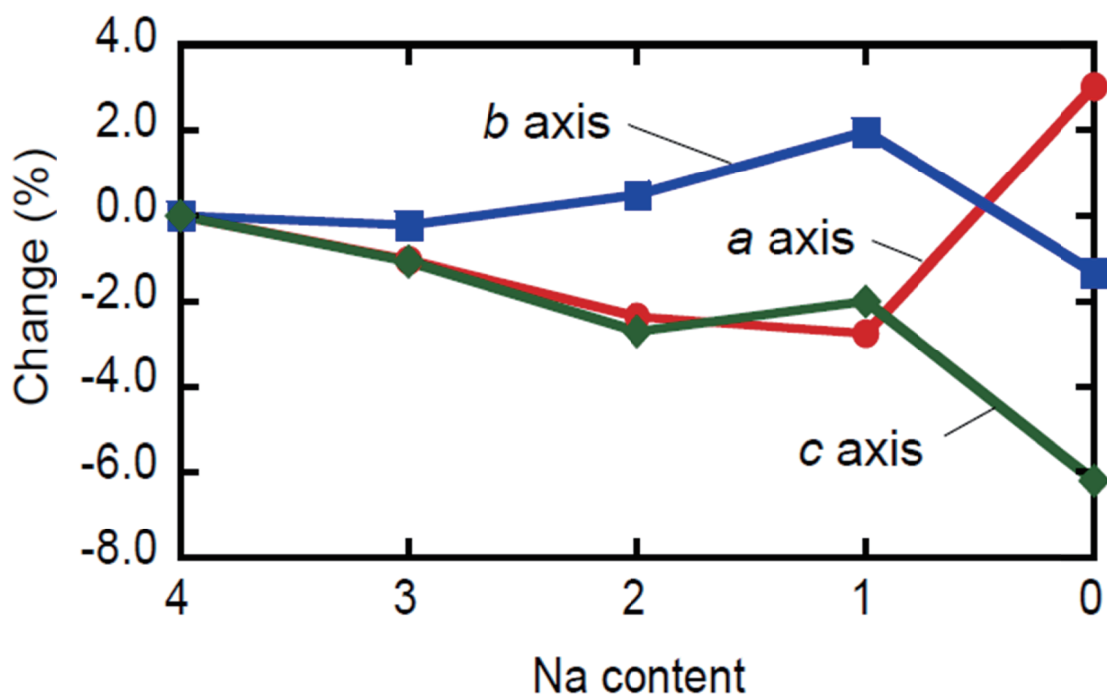


Fig. 2.8 Lattice parameter changes during desodiation of $\text{Na}_4\text{CO}_3(\text{PO}_4)_2\text{P}_2\text{O}_7$ ($x=4$ to 0).

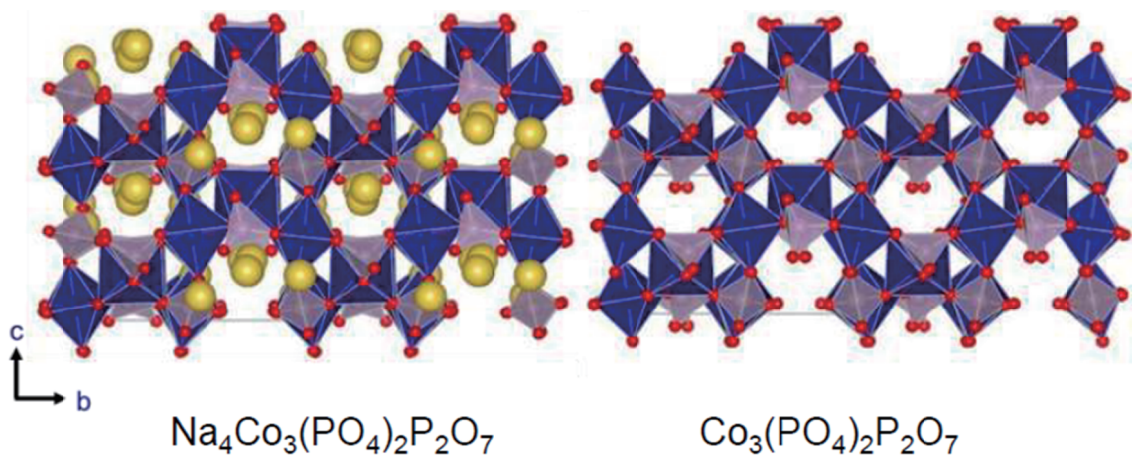


Fig. 2.9 Crystal structure changes during desodiation from $\text{Na}_4\text{Co}_3(\text{PO}_4)_2\text{P}_2\text{O}_7$ to $\text{Co}_3(\text{PO}_4)_2\text{P}_2\text{O}_7$ using the same atom representations as Fig. 2.1. The largest change is due to channel contraction when Na4 atoms are removed during the last desodiation step.

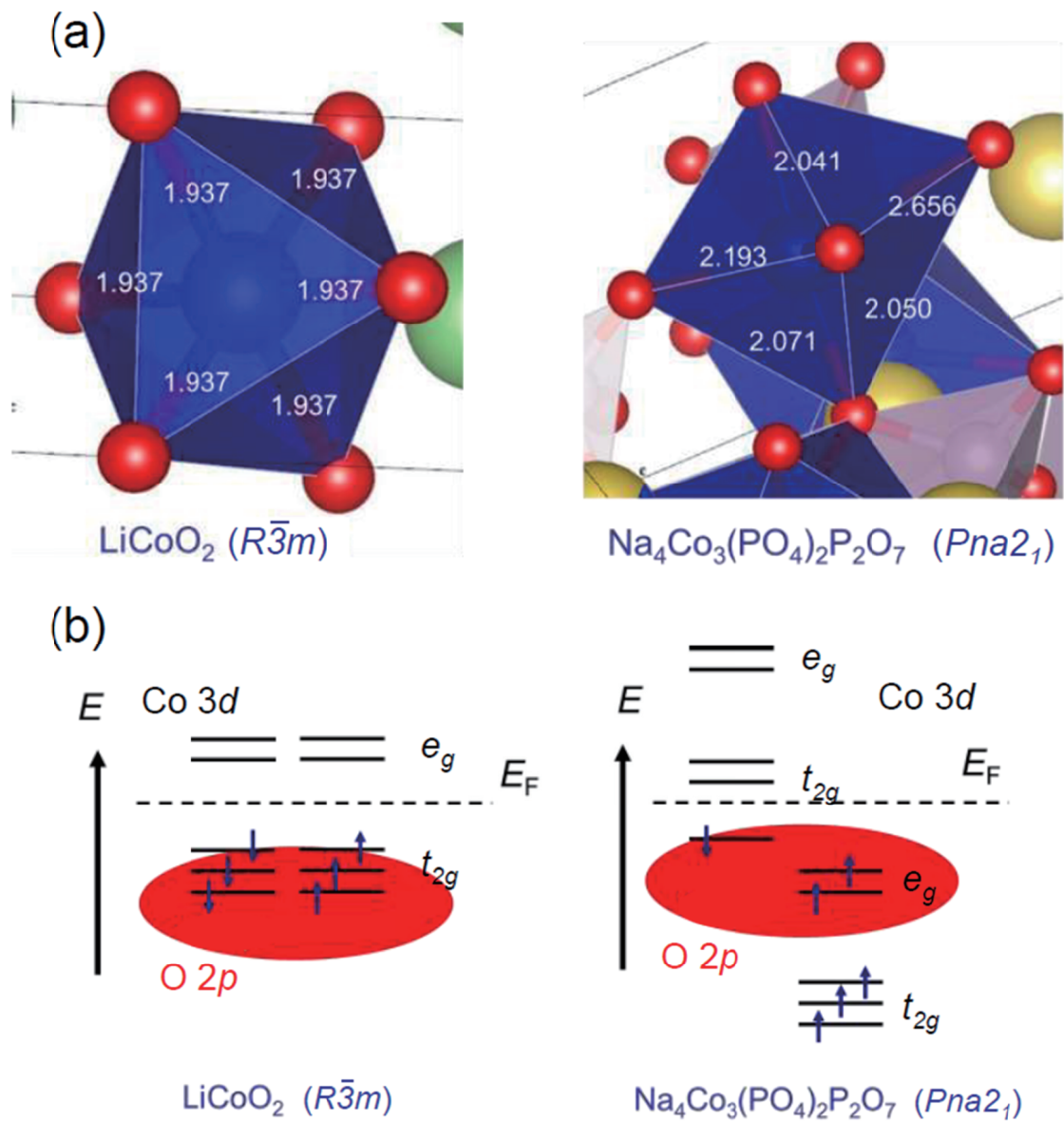


Fig. 2.10 Local structures around Co ions in LiCoO₂ and Na₄Co₃(PO₄)₂P₂O₇ with bond lengths in A using the same atom representations as Fig. 2.1; (b) Co3d spin states (horizontal bars) relative to O2p orbitals (filled ellipses) and the Fermi energy (E_F) for LiCoO₂ and Na₄Co₃(PO₄)₂P₂O₇.

Chapter III

Na₄Ni₃(PO₄)₂P₂O₇; First-ever Experimental Evidence on Potentially Highest Properties of Nickel-based Polyanion Family

3.1. Introduction

High power batteries have been required to enhance fuel and/or electric efficiencies of upcoming systems in hybrid vehicles. Researches on high potential active materials for a positive electrode are one of the important approaches to enhance power densities of the batteries. Cobalt-based polyanion compounds (e.g. LiCoPO₄, Li₂CoPO₄F, Li₂CoP₂O₇) for lithium-ion batteries exhibit 4.8 V (vs. Li⁺/Li)-class working potentials [1-5], while they have often suffered from capacity fading with increase in cycle number. [4,6,7] On the other hand, considerable predictions by density functional theory (DFT) calculations have accumulated by many researchers to imply higher redox potentials of Ni²⁺/Ni³⁺ than Co²⁺/Co³⁺ in the isostructural polyanion frameworks [8-10]. Given the calculation results, new electrode materials of nickel-based counterparts have been desirable to establish new batteries with high power. It, however, appears that redox reaction of Ni²⁺/Ni³⁺ in any polyanion frameworks behaves inactive. As represented by olivine-LiNiPO₄, it is well accepted that the inactive natures of nickel-based counterparts are derived from either low electric or ionic conductivity [11, 12]. Carbon coating and/or lattice doping can compensate for the insulating natures and decrease in diffusion length by using fine particles can enhance diffusivity in bulk [13-15]. Such various attempts have been conducted on the use of nickel-based counterparts as a positive electrode.

Despite the great efforts, comparable reversible capacities to cobalt-based polyanion family have not been confirmed yet [16-19].

Recently, we reported new active materials of $\text{Na}_4\text{Co}_3(\text{PO}_4)_2\text{P}_2\text{O}_7$ (NCPP) and its derivatives, classified as high potential positive electrodes for sodium-ion batteries (SIBs) [20-22]. Redox couples of $\text{Co}^{2+}/\text{Co}^{3+}$ in NCPP appears in high potential region from 4.1 V to 4.7 V (*vs.* Na^+/Na). Substituting Co^{2+} for Ni^{2+} in the structure would be an effective way to raise reaction potential, while the electrochemical activity of $\text{Na}_4\text{Ni}_3(\text{PO}_4)_2\text{P}_2\text{O}_7$ (NNPP), isostructural to NCPP [23, 24], was not reported yet. Additionally, NCPP delivers the reversible capacity of 95 mAhg^{-1} , which can be repeatedly obtained even at 50th cycle [20]. The cycle performance of NCPP apparently differs from the sharp capacity fading of LiCoPO_4 , implying high stability of the new intercalation structure even in the course of charge/discharge reaction under high electrode potentials. There has been growing recognition that cation mixing as one of the significant degradation modes arises between two ions which have close ionic radii such as Li^+ and Co^{2+} (or Co^{3+}) [25, 26]. Also, positive solution energies of Na^+ substitution to Co^{2+} or Ni^{2+} sites in olivine structure were evaluated by DFT calculations [27]. The previous researches deduce cation mixing would be inherently unfavorable in the new intercalation structure owing to the wide difference in ionic radii of constituent elements, namely, Na^+ , P^{5+} and Co^{2+} (or Co^{3+}). Herein, understanding electrochemical and structural characteristics of NNPP set a precedent for the use of various nickel-based counterparts as a positive electrode for high power batteries.

3.2. Experimental

$\text{Na}_4\text{Ni}_3(\text{PO}_4)_2\text{P}_2\text{O}_7$ was synthesized by using a sol-gel method. Reagent grade of $(\text{CH}_3\text{COO})_2\text{Ni}$, $\text{Na}_4\text{P}_2\text{O}_7$ and $\text{NH}_4\text{H}_2\text{PO}_4$ (Nacalai tesque) were used as the starting materials. The stoichiometric ratio of these materials was mixed in a diluted nitric acid solution and then

glycolic acid was added to prevent the particle growth of $\text{Na}_4\text{Ni}_3(\text{PO}_4)_2\text{P}_2\text{O}_7$ precursor. The solution was heated at 80°C for 12 h with continuous stirring. The gel obtained was annealed at 300°C for 5hr and then 700°C for 50hr under air atmosphere. After the powder was mechanically milled, heat treatment at 700°C for 5hr was carried out under air atmosphere. As-prepared material was mixed with sucrose as a carbon resource and subsequently heat treatment was carried out at 700°C for 5hr under flowing Ar gas to carbonize the sucrose.

Electric conductivity of as-prepared material by the sol-gel method and subsequently heat treatment at 700°C for 50hr under air atmosphere was evaluated as ca. 10^{-11} S/cm by powder resistance measurement (Hiresta-UP MCP-HT450, Mitsubishi Chemical Analytech Co., Ltd). On the other hand, Electric conductivity of NNPP after carbonization of sucrose was investigated by powder resistance measurements (Loresta-GP MCP-T610, Mitsubishi Chemical Analytech Co., Ltd.).

All composite electrodes consist of 85wt% $\text{Na}_4\text{Ni}_3(\text{PO}_4)_2\text{P}_2\text{O}_7$ as an active material, 10wt% residual carbon and acetylene black as a conductive carbon and 5wt% poly(vinylidene fluoride) as a binder. The electrochemical tests of as-prepared electrodes were conducted by using the CR2032 coin type cell at 25°C , with a sodium metal (Aldrich) as counter electrode. The electrolyte was 1.0 mol/cm^3 NaPF_6 dissolved in ethylene carbonate (EC) / dimethyl carbonate (DMC) (50:50 by vol., Kishida Chem., battery grade).

The pristine NNPP and several charged states to 17 mAhg^{-1} , 34 mAhg^{-1} , 51 mAhg^{-1} , 68 mAhg^{-1} , 85 mAhg^{-1} and 5.1 V (vs. Na^+/Na) was characterized by synchrotron X-ray diffraction (SXRD) measurement at beam line BL19B2 SPring-8 in Japan and the wavelength of incident X-ray beam was set to 0.5 \AA using a silicon monochromator. Structural analysis by the Rietveld method was carried out using RIETAN-FP [28] and the schematic illustrations of the crystal structure were drawn by using the program VESTA [29].

First-principles calculations were performed using the projector-augmented wave (PAW) method within the framework of density functional theory (DFT), as implemented in the VASP code. Exchange-correlation interactions were treated by the generalized gradient approximation (GGA-PBE). On-site Coulomb repulsion was treated using the GGA+ U method. We used a Hubbard effective charge of $U_{\text{eff}}=6.4\text{eV}$ for Ni3d electrons. For the PAW potentials, 2p and 3s for Na, 3d and 4s for Co, 3s and 3p for P, and 2s and 2p for O were explicitly treated as valence electrons. Plane wave expansion was performed up to 500 eV. A $1\times 3\times 4$ k -point mesh, based on the Monkhorst-Pack scheme, was used for Brillouin zone sampling of primitive cells containing 104 atoms. Calculated errors were estimated to be below 10^{-5}eV per $\text{Na}_4\text{Ni}_3(\text{PO}_4)_2\text{P}_2\text{O}_7$ formula unit. Lattice constants and internal atomic coordinates were considered fully optimized when residual Hellmann-Feynman (HF) forces were smaller than $1.0\times 10^{-2}\text{ eV/\AA}$. For simplicity, all spin configurations were considered to be ferromagnetic.

3.3. Results and discussion

At first, the yellow powder of NNPP, synthesized by a sol-gel method (Supporting Information), exhibited low electric conductivity of ca. 10^{-11} S/cm (Fig. 3.1) and was classified as an insulator. The powder was mixed with sucrose as a carbon resource and heat treatment was carried out at 700°C for 5hr under flowing Ar gas to carbonize the sucrose. Figure 3.2 shows SXRD pattern of NNPP after carbonization of sucrose and the crystal structure was optimized by Rietveld analysis. Rietveld analysis of the XRD pattern confirmed the pure single phase and the diffraction peaks were successfully indexed (Agreement factors: $R_{\text{wp}}=4.675$, $R_p=3.308$, $R_e=3.448$, $S=1.36$) with a space group of $Pna2_1$, having an orthorhombic unit cell with the lattice parameters ($a=18.0066(3)\text{\AA}$, $b=10.4076(1)\text{\AA}$, $c=6.4941(1)\text{\AA}$). Refined atomic position was also listed in Table 1. The SEM image (Fig. 3.3) of NNPP after carbonization

revealed the particle size ranges from 100 nm to 1 μm and auger electron spectroscopy (AES) mapping of the resultant black powder revealed carbon layer was homogeneously covered on the surface of the particles and as a result, the electric conductivity of the powder was improved to ca. 10^{-5} S/cm (Fig. 3.1).

Next, we describe the electrochemical characteristics investigated by using coin-type cell with sodium metal as a counter electrode. All composite electrodes consist of 85wt% NNPP as an active material, 10wt% residual carbon and acetylene black as a conductive filler and 5wt% poly(vinylidene fluoride) as a binder. The thermogravimetric analysis (TG) was measured to determine the amount of residual carbon. (Fig. 3.4) Here, all potentials (V) are referred to Na^+/Na . Fig. 3.5a shows the initial charge/discharge profiles at the current density of 34 mA g^{-1} (0.14 mA cm^{-2}). NNPP could deliver the reversible capacity of 62 mAh g^{-1} and the coulomb efficiency was estimated to 65%. Fig. 3.5b shows the cycle performance at 34 mA g^{-1} between 3.5 V and 5.1 V. While the slight irreversible capacity still remained at 30th cycle, the capacity retention was estimated to 71%. The extra charge capacity repeatedly obtained would be ascribed as side reactions such as electrochemical oxidation of organic electrolyte because the electrode was exposed to high potential above 4.5 V. We believe further development on electrolytes with wide potential window will make it possible to improve the cycle performance. Rate capabilities of Na^+ insertion reaction (Fig. 3.5c) were also investigated. All samples were charged to 5.1 V at 34 mA g^{-1} and subsequently discharged at higher current densities at 340 mA g^{-1} (1.4 mA cm^{-2}) and 850 mA g^{-1} (3.5 mA cm^{-2}). The capacity retentions compared to the discharge capacity at 34 mA g^{-1} were estimated to 98% and 94% at 340 mA g^{-1} and 850 mA g^{-1} , respectively. Potential drops under applying the high current densities were small enough to maintain 4.3 V-class discharge potentials even at 850 mA g^{-1} , suggesting the rate performances should be acceptable.

Structural characterization of NNPP during Na⁺ extraction was also discussed. As described in Fig. 3.6, the diffraction pattern of the charged electrode to 5.1 V is different from the pristine electrode (Fig. 3.2a), indicating structural transformation should occur by Na⁺ extraction from NNPP. Given the sufficient intensity of the patterns, there is no significant structural degradation such as amorphous transformation, which often contributes to low efficiency and/or poor cycle performance. [30] The crystal structure charged to 5.1 V has an orthorhombic unit cell with the lattice parameter of a= 17.3456(7)Å, b= 10.4576(5)Å, c=6.5520(3)Å and it is clarified by comparing with pristine NNPP that the lattice shrink 3.7% along a-direction and expand 0.5% and 0.9% along b and c directions, respectively. Hence, Na⁺ extraction induces anisotropic changes of the crystal structure. The volume change (ΔV) was also estimated to 2.3% and was small enough to use as a practical electrode material.

Potential steps shown in charge profile indicate Na⁺ extraction would proceed through multistep reaction paths. To promote better understanding of the mechanism, we corrected SXRD patterns at several charged states as described in Fig. 3.7. With regard to pristine NNPP, the peak (I) around 3.18° is ascribed as the diffraction pattern of (200) lattice plane. When the electrode was charged to 17 mAhg⁻¹, the peak (I) shows no significant shift and the new peak (II) appeared at the higher angle region around 3.25°. The intensity ratio of peak (II) vs. peak (I) was increased by further Na⁺ extraction up to 34 mAhg⁻¹. The behavior itself is similar to Li⁺ extraction mechanism of LiFePO₄ [31-33], which is so-called “two-phase reaction”. Another peak (III) at the higher angle around 3.4° slightly appeared and it is clarified that three phases (I), (II) and (III) should coexist. The intensity ratio of peak (III) vs. peak (II) was increased by further Na⁺ extraction up to the charge capacity of 51 mAhg⁻¹ with decrease in the intensity of peak (I) and two kinds of two phase reactions viz. phase (I)→(II) and phase (II)→(III) would proceed in parallel at the latter part of the first potential plate. After charging to 68 mAhg⁻¹, the

patterns dramatically changed and the new peak (IV) around 3.28° clearly appeared, while the other peaks are almost invisible. When the electrode potential was reached to 5.1 V, the new single phase (IV) only existed as mentioned above. In the course of the second plate, the change of lattice parameter was negligible. Hence, it is conjectured that Na^+ extraction from phase (IV) would be single phase reaction rather than two phase. Regarding (011) lattice planes, the initial peak position around 5.2° shifted to lower position around 5.1° . The shift to lower position is apparently differs from the behavior of (200) and (210) lattice planes, supporting anisotropic changes of the crystal structure during Na^+ extraction.

When we focus on lower Bragg angle region of $2.0\text{-}3.0^\circ$, diffraction pattern having faint intensity appeared at 2.8° and 2.4° after charged to 34 mAh/g and 68 mAh/g, respectively. d values of 10.3 Å and 11.6 Å estimated by Bragg equation correspond to three-fifth and two-third of the lattice parameter of a -direction at charged state, indicating superlattice structure having Miller indexes of (5/300) and (3/200) planes. We also investigated Na^+ extraction sites from pristine NNPP by DFT calculation in order to clarify the origin of these superlattice structures. As described in Fig. 3.8, pristine NNPP has crystallographically four kinds of Na^+ sites. For the comparison purpose, free energies of $\text{Na}_3\text{Ni}_3(\text{PO}_4)_2\text{P}_2\text{O}_7$ produced by Na^+ extraction of each Na^+ site were calculated. It clarified that $\text{Na}_3\text{Ni}_3(\text{PO}_4)_2\text{P}_2\text{O}_7$ after Na^+ extraction from Na2 or Na3 site have lower free energies than Na1 or Na4 and therefore Na^+ was preferably extracted from Na2 and Na3 sites located along a -direction. Given this point, superlattice structures of (5/300) and (3/200) planes could be explained by rearrangement of residual Na^+ sites having wide distances of 10.3 Å and 11.6 Å along a -direction. Figure 3.9a describes wireframe view of superlattice structure having two times a -axis length and 32Na^+ . After initial 10Na^+ , corresponding to ca. 53 mAhg^{-1} , was extracted from 16Na^+ located at Na2 and Na3 sites and residual 6Na^+ was rearranged in a regular interval as described in Fig. 3.9b.

Here we used the Na1, Na4, Ni, P and O sites obtained by Rietveld refinement shown in Fig. 3.6 (Not considering superlattice structure). The 10Na^+ extraction was also accompanied with multi-phase reaction and further extraction induced structural rearrangement, resulting in single phase IV. However, the diffraction pattern around 2.4° still remained after charged to 5.1 V, indicating the residual 6Na^+ couldn't be removed by further charging. By combining this result with DFT calculation, it is implied that Na^+ located at Na1 and Na4 would be extracted at the latter half of charge, in other word, higher potential region.

From here, we discuss the latter half of charge reaction mechanism. While the SXRD patterns obtained after charged above 68mAhg^{-1} were almost similar each other, we found the intensity of diffraction patterns around 6.6° gradually increased. The d-value was estimated to 8.67 \AA which is half of a-axis lattice parameter and the plain interval indicates the faint diffraction pattern should be derived from (200) plane. As mentioned above, Na^+ was extracted from Na1 and Na4 sites at latter half of charge. When all 16Na^+ at Na1 and Na4 sites still remains like Model A (Fig. 3.10c), the interval of Na^+ is not uniform. After charged to 5.1 V, the capacity was reached to ca. 96mAhg^{-1} , estimated to 18Na^+ extraction in the superlattice structure. In other words, 8Na^+ was extracted from Na1 and Na4 sites at the latter half of charge and therefore we assumed the crystal structure (Model B, Fig. 3.10d) arranging 8Na^+ at Na1 and Na4 sites uniformly. Figure 3.10b shows simulated XRD patterns of pristine phase, Model A and B around 6.6° . The intensity of the pattern around 6.6° was gradually increased by arranging Na^+ sites uniformly with charging and the behavior is good agreement with the actual diffraction patterns shown in Fig. 3.10a..

To combine the structural transformations with their reaction potentials, cyclic voltammograms (CVs) were corrected at low scan rate of 0.01 mVs^{-1} . As shown in Fig. 3.11, five kinds of redox couples (A-A') ~ (E-E'), which are successfully comparable to the

charge/discharge profiles, were confirmed in the potential region of 4.3-5.1 V. Na⁺ extraction from Na2 and Na3 sites in phase (I), corresponds to the oxidation current peak (A), which has an overlap with peak (B) in the slightly higher potential region. The overlap of the redox couples supports the competition reaction, not the consecutive reaction, of two phase reactions (I) → (II) and (II) → (III). Further Na⁺ extraction at the 3rd current peak (C) led to form the single phase (IV) by arranging residual Na⁺ at 2Na and 3Na sites uniformly. The structural rearrangement could be induced by the structural stability of phase (IV) compared to coexistence states of phase (I+II+III). After that, Na⁺ was extracted from Na1 and Na4 sites in phase (IV), corresponding to the peaks (D) and (E). The charge reaction exhibits single phase reaction. The potential difference in Na⁺ extraction from phase (I) and (IV) was evaluated as ca. 0.4 V, suggesting higher Na⁺ chemical potential of Na1 and Na4 sites in phase (IV) than Na2 and Na3 sites in phase (I).

When it comes to reversibility of Na⁺ extraction/insertion, the typical characteristics is the low polarizations ($\Delta V = 40\sim 70$ mV) of each redox couples except for (A–A') ($\Delta V = 220$ mV), which are good agreement with the acceptable rate capabilities as mentioned above. In general, the polarization of redox couple on CV is influenced by both ion conductivity of electrolyte and ion diffusivity in bulk. In this case, the former couldn't explain the behavior because it doesn't change during charge/discharge. With regard to the latter, Na⁺ insertion path at low Na⁺ contents can be selective among kinetically more favorable diffusion pathways and inserted Na⁺ would be preferentially occupied along the pathways. As a consequence, the diffusivity was decreased at high Na⁺ contents during Na⁺ insertion. Cationic repulsion of Na⁺–Na⁺ can also contribute to poor reversibility especially at high Na⁺ contents. Such a structural drawback at high Na⁺ contents will be covered by increase in the number of the insertion sites and decrease in the particle size is still needed.

3.4. Conclusion

This paper described first experimental evidences on the highest redox potential of Ni²⁺/Ni³⁺ in NNPP as a member within the nickel-based polyanion family. The reversible capacity was currently limited to 48% compared to its theoretical capacity of 130 mAhg⁻¹, corresponding to one electron reaction of Ni²⁺/Ni³⁺ and there still exist needs for optimizing synthesis conditions to control particle sizes and/or utilizing electrolyte with wide potential window to increase in the capacity. To get a better understanding of reaction mechanism, structural characterization during charge reaction was also investigated. We found NNPP shows competitive two phase reactions and subsequently phase transition to single phase by arranging residual Na⁺ sites uniformly. The structural rearrangement during Na⁺ extraction can lead to more stable phase (IV) and the reversibility contributes to good cycle performance. We believe the findings will open up new possibility of utilizing nickel-based polyanion family, which have been expected as potentially highest properties as a positive electrode for either SIBs or LIBs.

References

- [1] K. Amine, H. Yasuda and M. Yamachi, *Electrochem. Solid-State Letters*, 3 (2000) 178-179.
- [2] S. Okada, S. Sawa, M. Egashira, J. Yamaki, M. Tabuchi, H. Kageyama, T. Konishi and A. Yoshino, *J. Power Sources*, 97-98 (2001) 430-432.
- [3] S. Okada, M. Ueno, Y. Uebou and J. Yamaki, *J. Power Sources*, 146 (2005) 565-569.
- [4] X. Wu, Z. Gong, S. Tan and Y. Yang, *J. Power Sources*, 220 (2012) 122-129.
- [5] H. Kim, S. Lee, Y. U. Park, H. Kim, J. Kim, S. Jeon and K. Kang, *Chem. Mater.*, 23 (2011) 3930-3937.
- [6] J. Wolfenstine, U. Lee, B. Poese, J. L. Allen, *J. Power Sources*, 144 (2005) 226-230.
- [7] E. Markevich, R. Sharabi, H. Gottlieb, V. Borgel, K. Firdman, G. Salitra, D. Aurbach, G.

- Semrau, M. A. Schmidt, N. Schall, C. Bruenig, *Electrochem. Commun.*, 15 (2012) 22-25.
- [8] G. Hautier, A. Jain, S. P. Ong, B. Kang, C. Moore, R. Doe, G. Ceder, *Chem. Mater.*, 23 (2011) 3495-3508.
- [9] M. E. Arroyo-de Dompablo, M. Armand, J. M. Tarascon and U. Amador, *Electrochem. Commun.*, 8 (2006) 1292-1298.
- [10] T. Mueller, G. Hautier, A. Jain, G. Ceder, *Chem. Mater.*, 23 (2011) 3854-3862.
- [11] D. Morgan, A. Van der Ven, G. Ceder, *Electrochem. Solid-State Lett.*, 7 (2) (2004) A30-A32.
- [12] J. Yu, K. M. Rosso, J. Liu, *J. Phys. Chem. C*, 115 (2011) 25001-25006.
- [13] P. Gibot, M. Casas-Cabanas, L. Laffont, S. Levasseur, P. Carlach, S. Hamelet, J-M. Tarascon and C. Masquelier, *Nature Mater.*, 7 (2008) 741-747.
- [14] S-Y.Chung, J.T.Bloking and Y.M.Chiang, *NatureMater.*, 1 (2002) 123-128.
- [15] J. J. Chen, M. S. Whittingham, *Electrochem. Commun.*, 8 (2006) 855-858.
- [16] J. Wolfenstine, J. Allen, *J. Power Sources*, 142 (2005) 389.
- [17] R. Qing, M. C. Yang, Y. S. Meng, W. Sigmund, *Electrochem. Acta*, 108 (2013) 827-832.
- [18] J. Wolfenstine, J. Allen, *J. Power Sources*, 136 (2004) 150-153.
- [19] M. Nagahama, N. Hasegawa, S. Okada, *J. Electrochem. Soc.*, 157 (6) (2010) 827-832.
- [20] M. Nose, H. Nakayama, K. Nobuhara, H. Yamaguchi, S. Nakanishi and H. Iba, *J. Power Sources*, 234 (2013) 175-179.
- [21] M. Nose, S. Shiotani, H. Nakayama, K. Nobuhara, S. Nakanishi and H. Iba, *Electrochem. Commun.*, 34 (2013) 266-269.
- [22] M. Nose, K. Nobuhara, S. Shiotani, H. Nakayama, S. Nakanishi and H. Iba, *RSC Adv.*, 4 (2014) 9044-9047.
- [23] F. Sanz, C. Parada, U. Amador, M. A. Monge, C. Ruiz-Valero, *J. Solid State Chem.* 123

(1996) 129-139.

[24] F. Sanz, C. Parada, J. M. Rojo, C. Ruiz-Valero, *Chem. Mater.*, 13 (2001) 1334-1340.

[25] Q. D. Truong, M. K. Devaraju, Y. Sasaki, H. Hyodo, T. Tomai, I. Honma, *Chem. Mater.* 26 (2014) 2770-2773.

[26] Q. D. Truong, M. K. Devaraju, T. Tomai, I. Honma, *ACS Appl. Mater. Interfaces*, 5 (2013) 9926-9932.

[27] Craig A. J. Fisher, Veluz M. Hart Prieto, M. Saiful Islam, *Chem. Mater.* 20 (2008) 5907-5915.

[28] F. Izumi and K. Momma, *Solid State Phenom.*, 130 (2007) 15-20.

[29] K. Momma, F. Izumi, *J. Appl. Crystallogr.*, 41 (2008) 653-658.

[30] Y. X. Li, Z. L. Gong and Y. Yang, *J. Power Sources.*, 174 (2007) 528-532.

[31] A. K. Padhi, K. S. Nanjundaswamy, J. B. Goodenough, *J. Electrochem. Soc.*, 144 (1997) 1188-1194.

[32] A. S. Andersson, B. Kalska, L. Haggstrom, J. O. Thomas, *Solid State Ion.*, 130 (2000) 41-52.

[33] C. Delmas, M. Maccario, L. Groguenec, F. Le Cras, F. Weill, *Nature Mater.*, 7 (2008) 665-671.

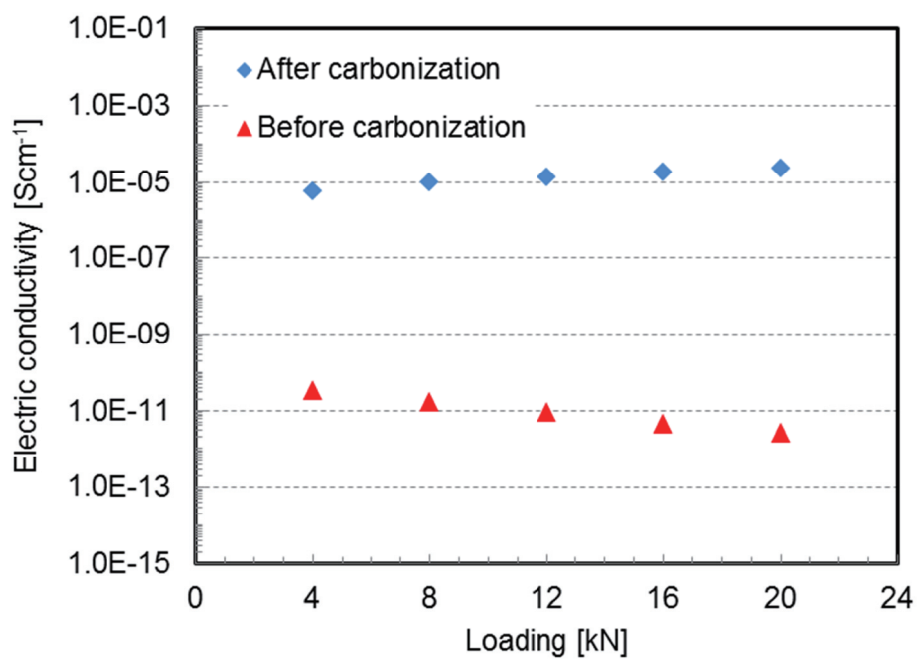
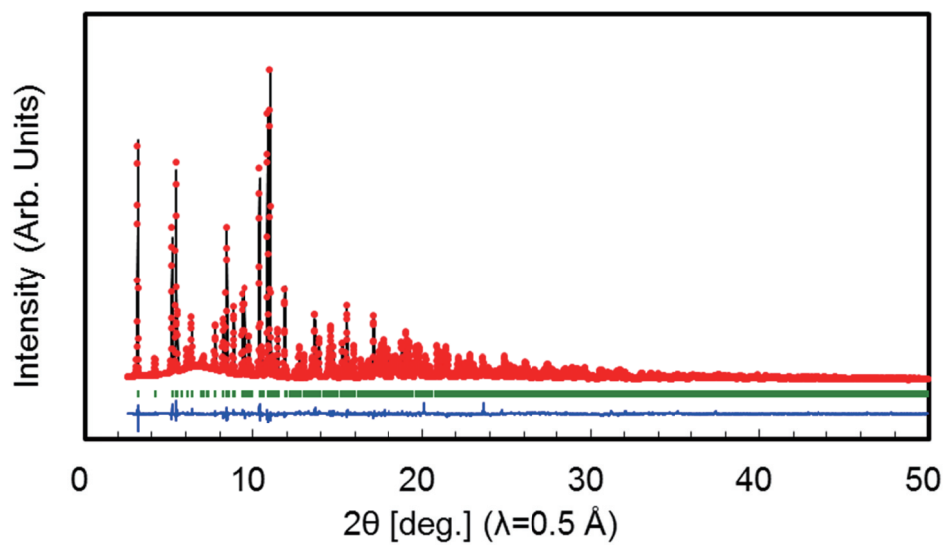


Fig. 3.1 Electric conductivities of NNPP before and after carbonization of sucrose.

a)



b)

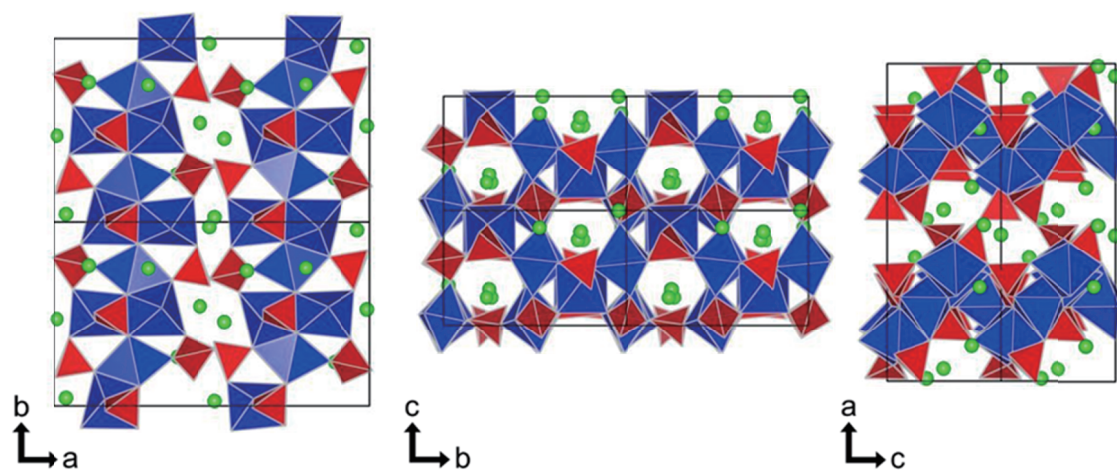


Fig. 3.2 a) Synchrotron X-ray diffraction pattern with Rietveld refinement and b) polyhedral view of crystal structure of $\text{Na}_4\text{Ni}_3(\text{PO}_4)_2\text{P}_2\text{O}_7$.

Table 1. Refined atomic position of $\text{Na}_4\text{Ni}_3(\text{PO}_4)_2\text{P}_2\text{O}_7$.

Atom	x	y	z	Temperature factor	Occupancy
Ni1	0.16913	0.00551	0.06092	0.123962	1
Ni2	0.13837	0.49704	0.07043	0.123962	1
Ni3	0.23942	0.74497	0.33657	0.123962	1
P1	0.28979	0.50462	0.07103	0.3482	1
P2	0.17866	0.48717	0.57577	0.3482	1
P3	0.07097	0.76459	0.2125	0.3482	1
P4	0.04878	0.22777	0.0244	0.3482	1
Na1	0.00816	0.47372	0.35012	1.140137	1
Na2	0.20296	0.24839	0.31442	1.140137	1
Na3	0.38953	0.26372	0.24431	1.140137	1
Na4	0.03907	0.04284	0.49914	1.140137	1
O1	0.23317	0.60587	0.11174	0.973538	1
O2	0.33917	0.47284	0.2544	0.973538	1
O3	0.16081	0.0355	0.39118	0.973538	1
O4	0.23614	0.38295	0.03779	0.973538	1
O5	0.26988	0.10726	0.05162	0.973538	1
O6	0.37375	0.01039	0.25302	0.973538	1
O7	0.23435	0.37617	0.60896	0.973538	1
O8	0.13194	0.46133	0.38147	0.973538	1
O9	0.00857	0.19127	0.81053	0.973538	1
O10	0.06005	0.63621	0.09503	0.973538	1
O11	0.12581	0.75825	0.37883	0.973538	1
O12	0.41501	0.38021	0.5572	0.973538	1
O13	0.04868	0.37042	0.05285	0.973538	1
O14	0.12839	0.18718	0.00768	0.973538	1
O15	0.00579	0.15182	0.17515	0.973538	1

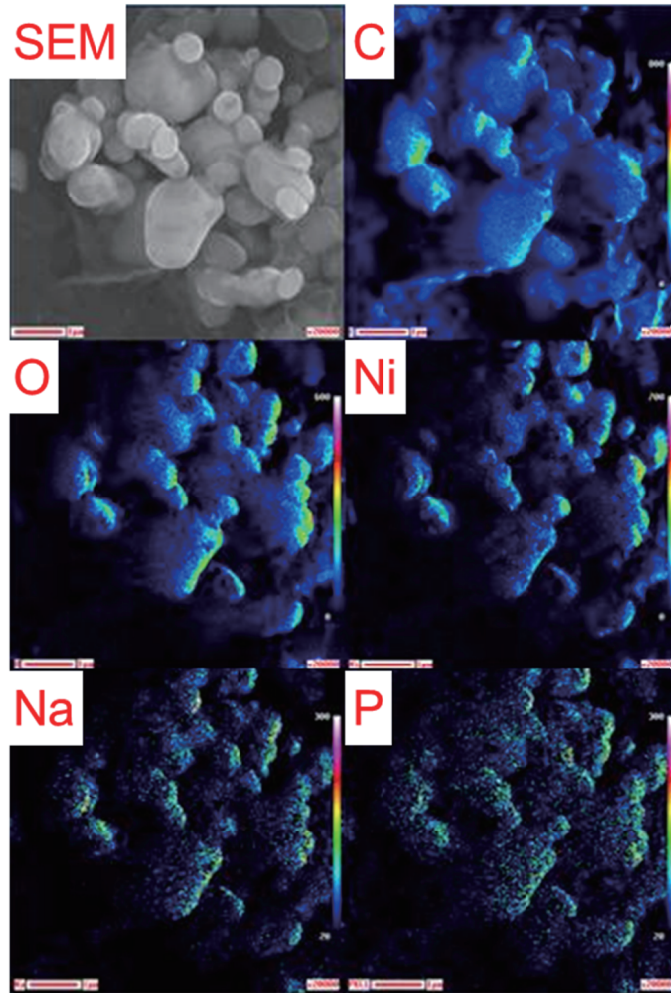


Fig. 3.3 SEM image and AES mapping of carbon-coated NNPP.

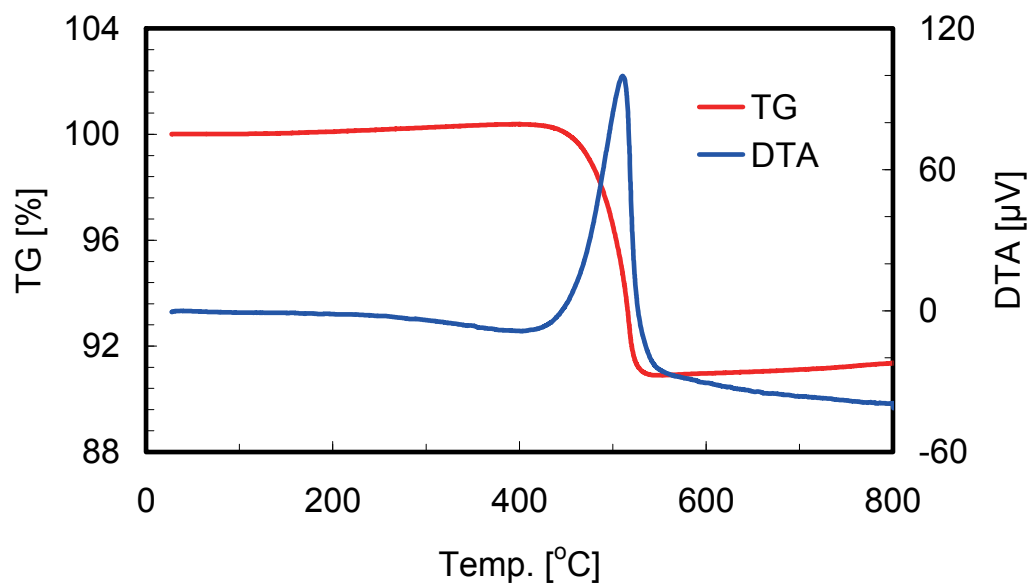


Fig. 3.4 TG and DTA curves of NNPP after carbonization of sucrose.

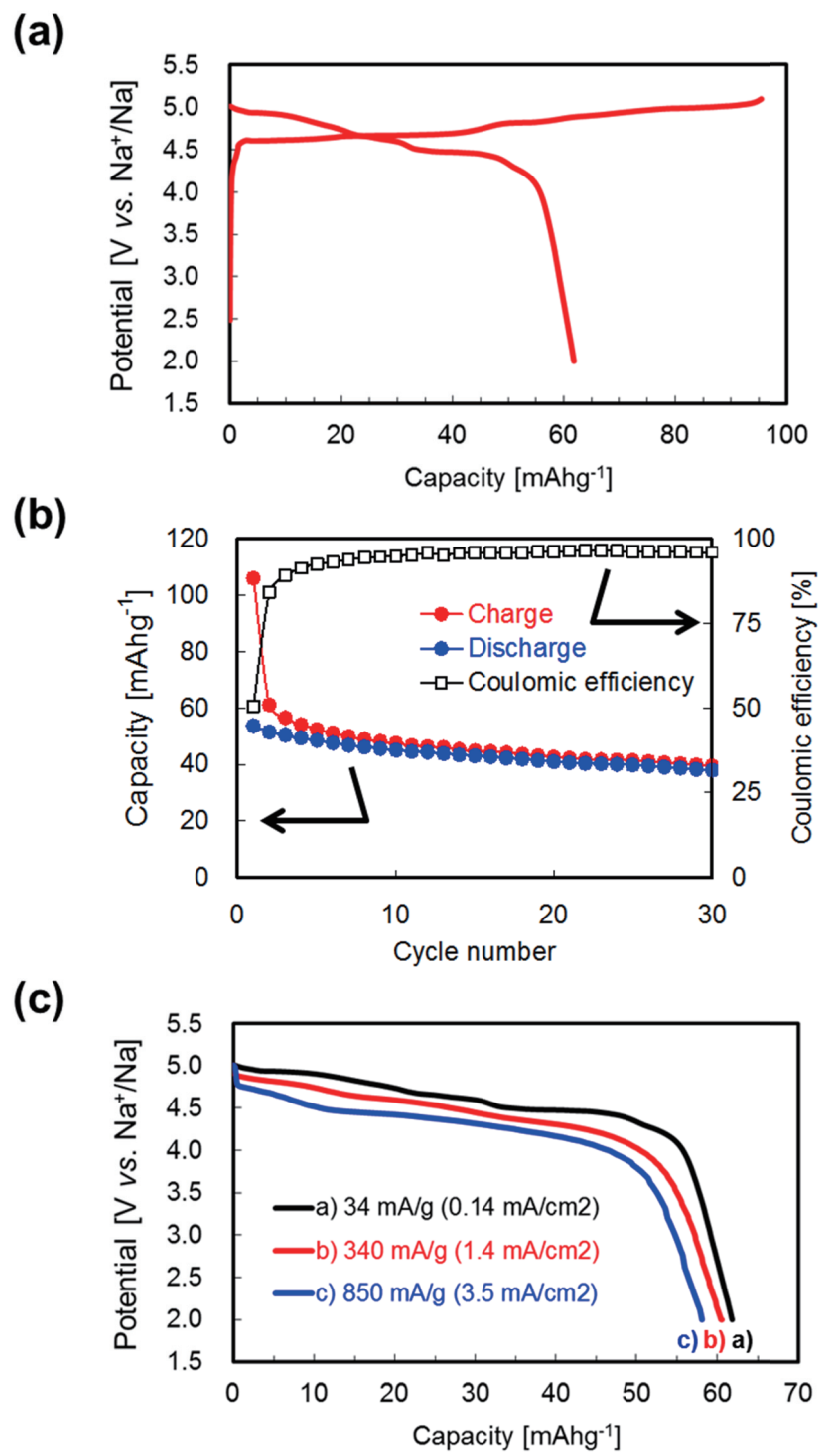


Fig. 3.5 a) Charge and discharge curve and b) cycle performance with coulombic efficiency of Na₄Ni₃(PO₄)₂P₂O₇. c) Discharge curves at various current densities of 34 mA/g, 340 mA/g and 850 mA/g after charged to 5.1 V vs. Na⁺/Na.

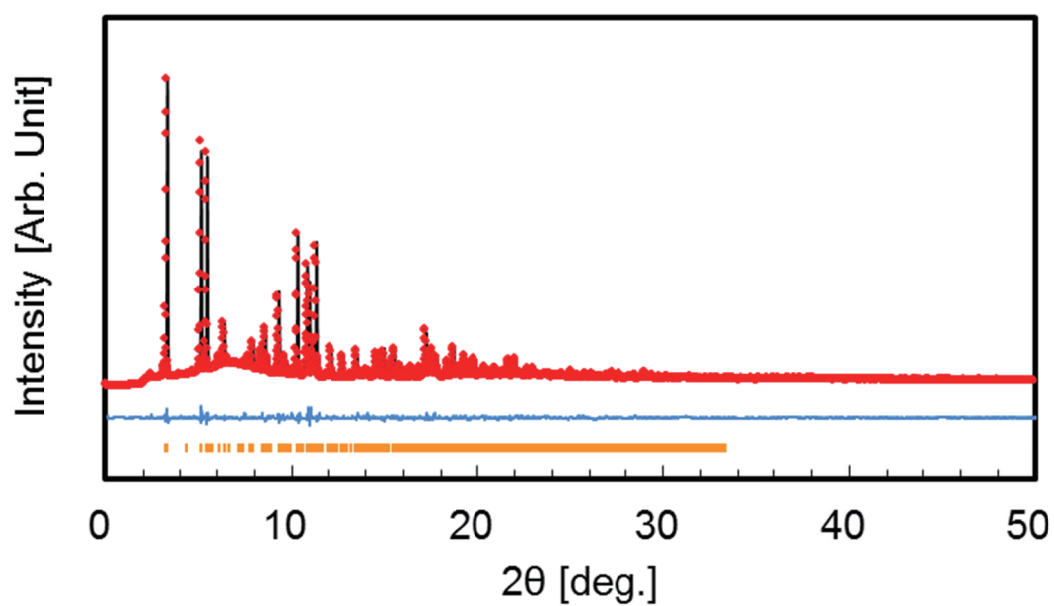


Fig. 3.6 Synchrotron X-ray diffraction pattern of NNPP at charged state to 5.1 V with Rietveld refinement (Agreement factors: $R_{wp}=6.45$, $R_p=4.09$, $R_e=5.46$, $S=1.18$)

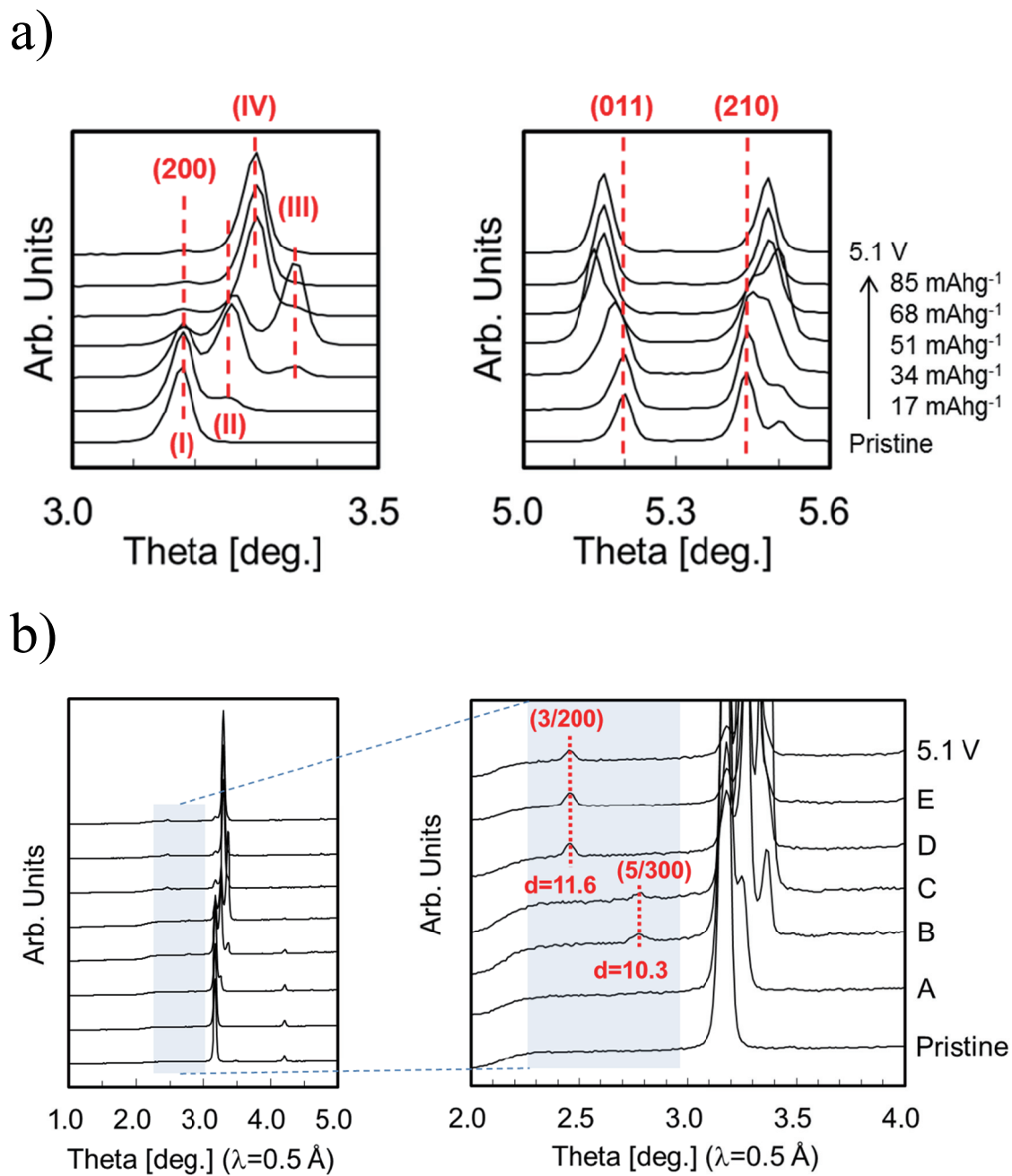
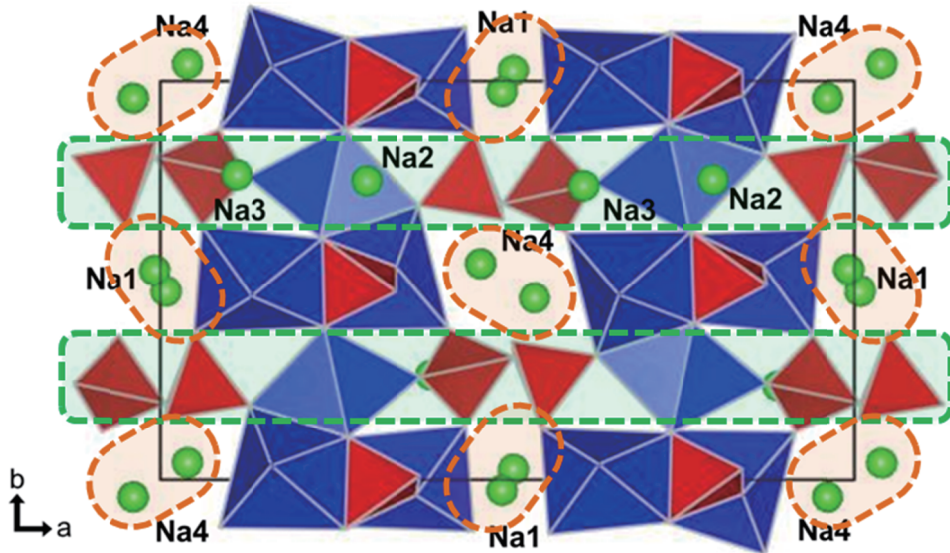


Fig. 3.7 a) *Ex-situ* synchrotron X-ray diffraction (SXRD) patterns of pristine $\text{Na}_4\text{Ni}_3(\text{PO}_4)_2\text{P}_2\text{O}_7$ and $\text{Na}_{4-x}\text{Ni}_3(\text{PO}_4)_2\text{P}_2\text{O}_7$ after charged to 17, 34, 51, 68 and 85 mAhg^{-1} . b) Facile diffraction patterns in the lower Bragg angle region of 2.0 and 3.0° .

a)



b)

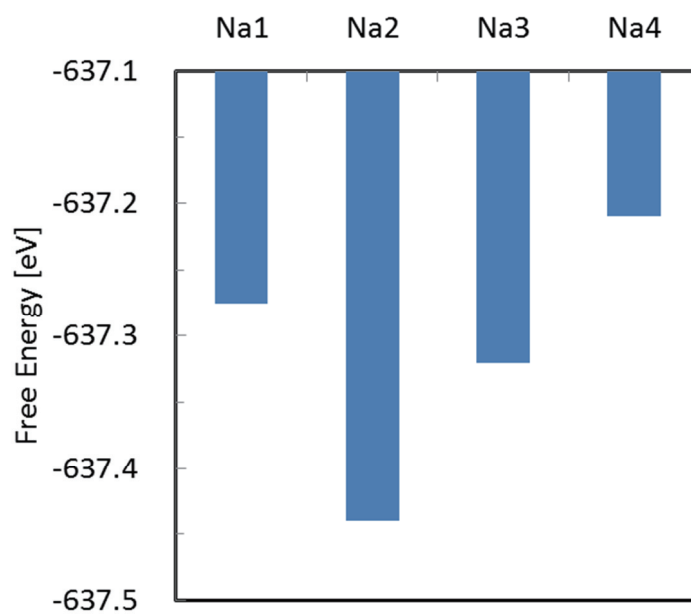
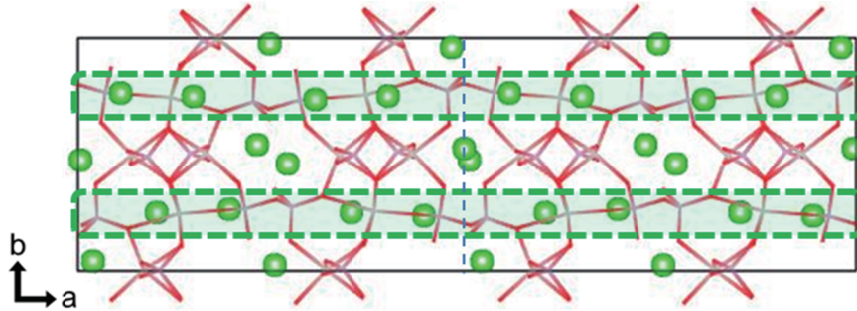
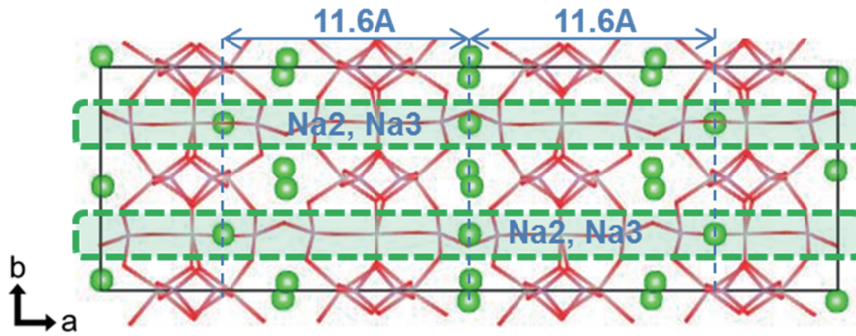


Fig. 3.8 a) Crystal structure with four kinds of Na⁺ accommodation sites of Na₄Co₃(PO₄)₂P₂O₇ and b) free energies of Na₃Co₃(PO₄)₂P₂O₇ after Na⁺ extraction on one site.

a)



b)



c)

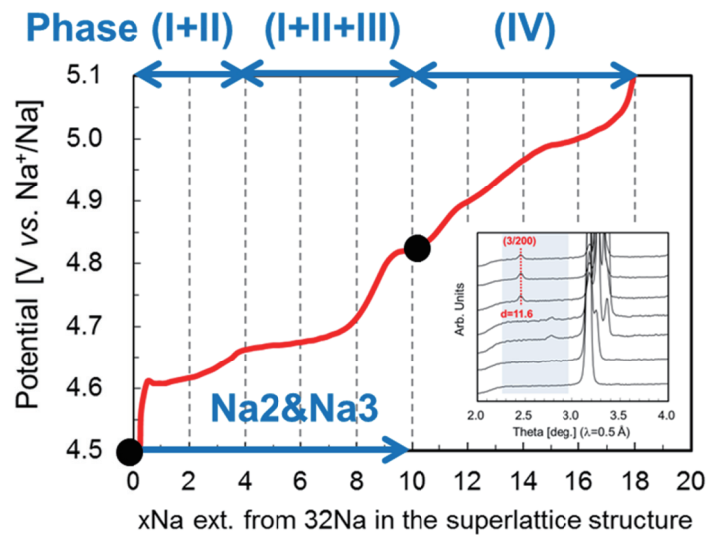


Fig. 3.9 Wireframe views of a) pristine $\text{Na}_4\text{Ni}_3(\text{PO}_4)_2\text{P}_2\text{O}_7$ (Phase I) and b) $\text{Na}_{4-x}\text{Ni}_3(\text{PO}_4)_2\text{P}_2\text{O}_7$ after charged 68 mAhg^{-1} (Phase IV). c) Charge curve at 34 mA/g as a function of $x\text{Na}^+$ extraction from 32Na^+ in the superlattice structure.

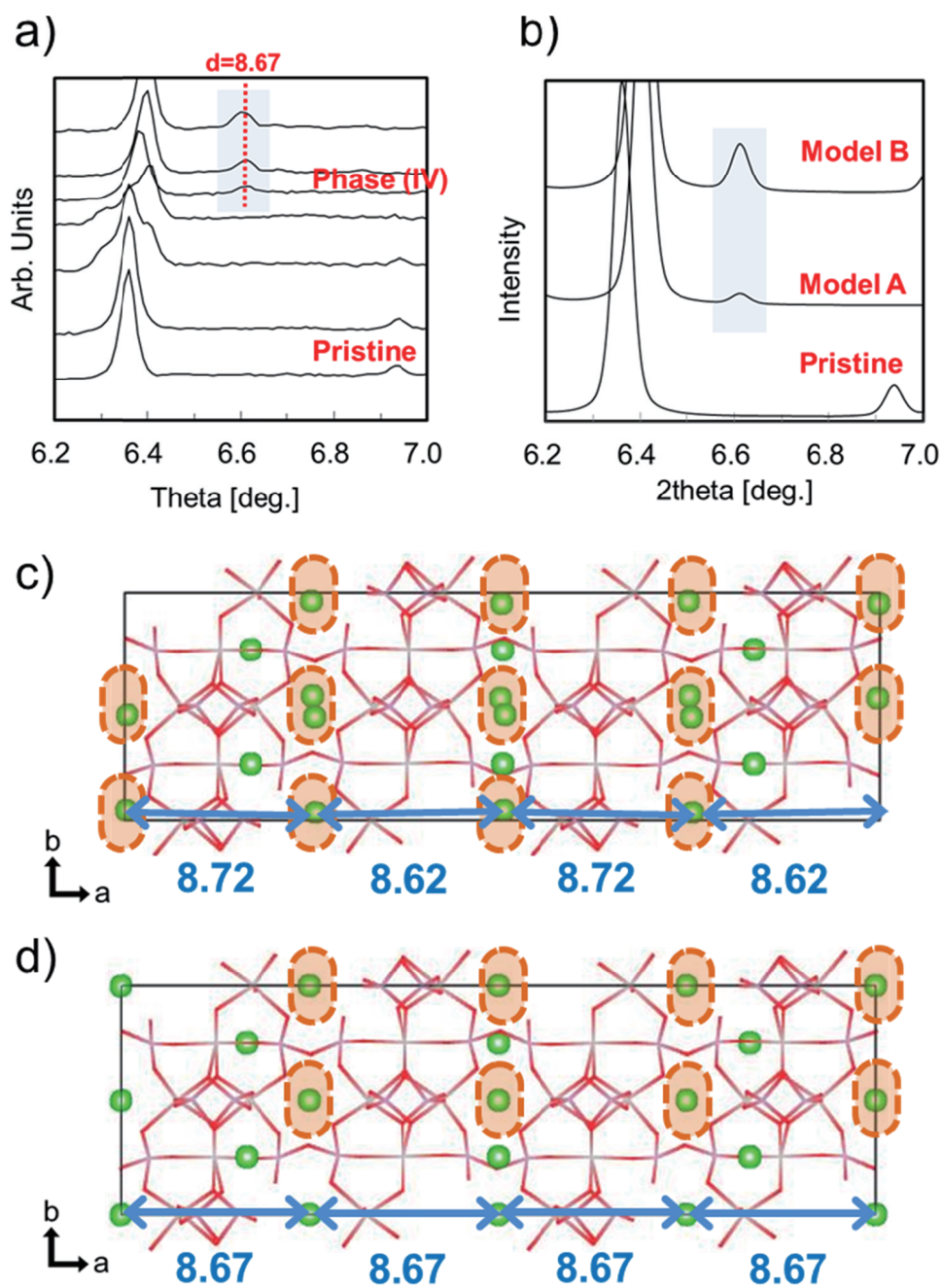


Fig. 3.10 a) Actual XRD patterns of pristine phase $\text{Na}_4\text{Ni}_3(\text{PO}_4)_2\text{P}_2\text{O}_7$ and charged phase $\text{Na}_{4-x}\text{Ni}_3(\text{PO}_4)_2\text{P}_2\text{O}_7$. b) Simulated XRD patterns of pristine and charged phases obtained from the crystal structures of c) Model A and d) B.

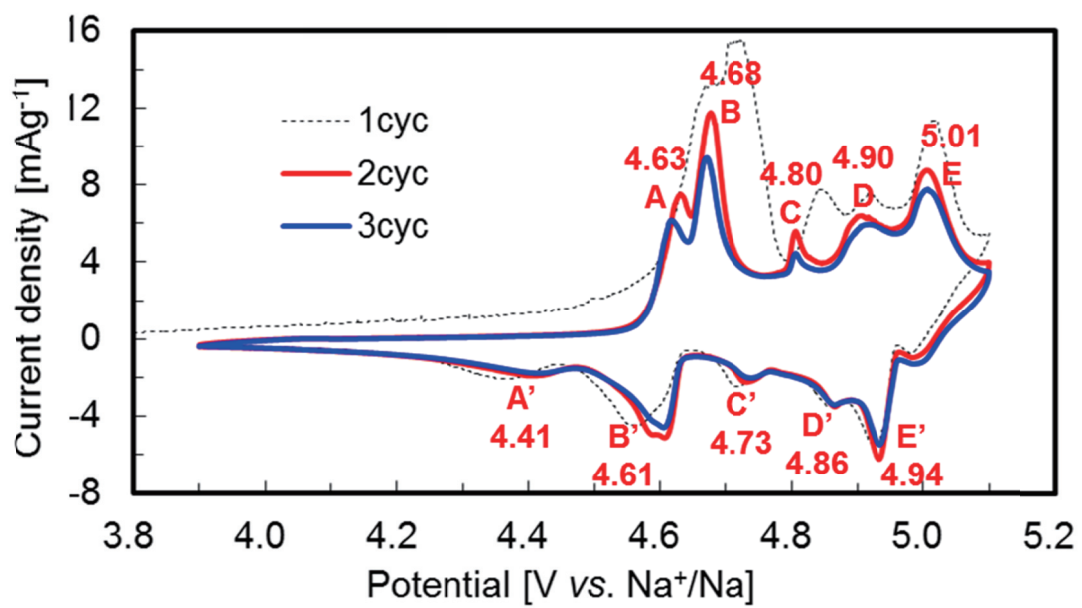


Fig. 3.11 Cyclic voltammograms of $\text{Na}_4\text{Ni}_3(\text{PO}_4)_2\text{P}_2\text{O}_7$ at the scan rate of 0.01 mVs^{-1} .

Chapter IV

$\text{Na}_4\text{Co}_{2.4}\text{Mn}_{0.3}\text{Ni}_{0.3}(\text{PO}_4)_2\text{P}_2\text{O}_7$: High Potential and High Capacity Electrode Material for Sodium-Ion Batteries

4.1. Introduction

Lithium-ion batteries (LIBs) have been used as the power sources of portable devices since their commercialization in 1991. LIBs are being applied to power sources of eco-friendly vehicles and the market of LIBs has grown rapidly in recent years. Therefore, LIBs are currently demanded to have higher performances for an energy density, a rate performance, sustainability, a safety etc and lithium is expected to be shortage in the near future. Nowadays, sodium-ion batteries (SIBs) using Na^+ instead of Li^+ as an ionic carrier have been reconsidered one of the future batteries to build up a sustainable society because of their comparably high energy densities and low Clerk number of Na.

Regarding positive electrode materials for SIBs, mixed polyanion family of $\text{Na}_4\text{Co}_3(\text{PO}_4)_2\text{P}_2\text{O}_7$ (95 mAhg^{-1} , 4.1-4.7 V vs. Na^+/Na) and $\text{Na}_4\text{Fe}_3(\text{PO}_4)_2\text{P}_2\text{O}_7$ (129 mAhg^{-1} , 3.2 V vs. Na^+/Na) has gained much attention because of their high potential or high capacity. [1,2] According to the report of F. Sanz et al, $\text{Na}_4\text{M}_3(\text{PO}_4)_2\text{P}_2\text{O}_7$ (M=Mn and Ni) are isostructural to $\text{Na}_4\text{Co}_3(\text{PO}_4)_2\text{P}_2\text{O}_7$ [3,4]. Given the close values of Co^{2+} , Mn^{2+} and Ni^{2+} ionic radii, novel phases described as $\text{Na}_4\text{Co}_{3-x}\text{M}_x(\text{PO}_4)_2\text{P}_2\text{O}_7$ (M=Mn and/or Ni) can be prepared, while their electrochemical characteristics have not been reported so far. During the course of the survey, we found that the novel $\text{Na}_4\text{Co}_{2.4}\text{Mn}_{0.3}\text{Ni}_{0.3}(\text{PO}_4)_2\text{P}_2\text{O}_7$ electrode material shows complex redox

behavior, which apparently differs from that of $\text{Na}_4\text{Co}_3(\text{PO}_4)_2\text{P}_2\text{O}_7$. Here we report the electrochemical characteristics of $\text{Na}_4\text{Co}_{2.4}\text{Mn}_{0.3}\text{Ni}_{0.3}(\text{PO}_4)_2\text{P}_2\text{O}_7$ and its charge compensation mechanism by using X-ray absorption spectroscopy (XAS).

4.2. Experimental

$\text{Na}_4\text{Co}_{2.4}\text{Mn}_{0.3}\text{Ni}_{0.3}(\text{PO}_4)_2\text{P}_2\text{O}_7$ was synthesized by using a sol-gel method. Reagent grade of $(\text{CH}_3\text{COO})_2\text{M}$ (M=Co, Ni and Mn), $\text{Na}_4\text{P}_2\text{O}_7$ and $\text{NH}_4\text{H}_2\text{PO}_4$ (Nacali tesque) were used as the starting materials. The stoichiometric ratio of these materials was dissolved into a diluted nitric acid solution and then glycolic acid was added to prevent the particle growth. The solution was heated at 80°C for 12hr with continuous stirring. The gel was annealed at 700°C for 50hr under air atmosphere. The powder and Vapor-Grown Carbon Fiber (Showa Denko, VGCF) were mixed with a weight ratio of 5 to 1, and subsequently heat retreatment was carried out at 700°C for 5hr under purging Ar. Then, a N-methyl pyrrolidone based slurry composed of the mixture of $\text{Na}_4\text{Co}_{2.4}\text{Mn}_{0.3}\text{Ni}_{0.3}(\text{PO}_4)_2\text{P}_2\text{O}_7$ (75 wt%) and VGCF (15 wt%), acetylene black (5 wt%) as a conductive filler and poly(vinylidene fluoride) (5 wt%) as a binder was cast on an aluminum current collector.

CR2032-type coin cell was fabricated with the above-described positive electrode. Metallic sodium (Aldrich) was used as a negative electrode and $1.0 \text{ mol/cm}^3 \text{ NaPF}_6$ (Kishida Chem.) dissolved in ethylene carbonate (EC) / diethylene carbonate (DEC) (50:50 by vol., Kishida Chem.) was applied to the electrolyte. All electrochemical tests were conducted in a thermostatic bath maintaining at 25°C . Galvanostatic charge/discharge tests were carried out at a constant current density of 34 mA g^{-1} (0.2C). Here, 1C was defined as the current density of 170 mA g^{-1} , at which its theoretical capacity (170 mAh g^{-1}) can be delivered for an hour. Rate

performances were also evaluated at 2C and 5C rates. Cyclic voltammetry was conducted at a constant scan rate of 0.01 mVs^{-1} in the potential region of 3.5-5.0 V vs. Na^+/Na .

The as-prepared electrode material was characterized by synchrotron X-ray diffraction (SXRD) measurements at beam line BL19B2 SPring-8 in Japan and the wavelength of incident X-ray beam was set to 0.499 \AA using a silicon monochromator. Structural analysis by the Rietveld method was carried out using RIETAN-FP [5] and the schematic illustrations of the crystal structure were drawn by using the program VESTA [6]. *Ex-situ* XAS spectra at the Co, Mn and Ni *K*-edges of the pristine and charged electrodes were also recorded in transmission mode at beam line BL-33XU of the synchrotron radiation facility SPring-8 in Japan.

4.3. Results and discussion

Figure 4.1a shows the synchrotron X-ray diffraction and Rietveld refinement patterns of as-prepared material. A small trace (ca. 0.5%) of NaCoPO_4 was identified as impurity and the crystal structure of the main product was successfully indexed with space group $Pna2_1$ in an orthorhombic unit cell with lattice parameters $a=18.0332(3) \text{ \AA}$, $b=10.5399(2) \text{ \AA}$ and $c=6.5367(1) \text{ \AA}$. Refined atomic position was listed in Table 1 and the fitting was satisfactory ($R_{\text{wp}}=4.63\%$, $R_e=4.03\%$, $S(R_{\text{wp}}/R_e)=1.08$). As illustrated in Fig. 4.1b, $\text{Na}_4\text{Co}_{2.4}\text{Mn}_{0.3}\text{Ni}_{0.3}(\text{PO}_4)_2\text{P}_2\text{O}_7$, isostructural to $\text{Na}_4\text{M}_3(\text{PO}_4)_2\text{P}_2\text{O}_7$, has Na^+ accommodation sites along multiple diffusion pathways in the refined crystal structure.

Fig. 4.2a shows the charge/discharge profiles of $\text{Na}_4\text{Co}_{2.4}\text{Mn}_{0.3}\text{Ni}_{0.3}(\text{PO}_4)_2\text{P}_2\text{O}_7$ in the potential range of 3.0-4.8 V vs. Na^+/Na at 0.2C rate. $\text{Na}_4\text{Co}_{2.4}\text{Mn}_{0.3}\text{Ni}_{0.3}(\text{PO}_4)_2\text{P}_2\text{O}_7$ has two potential plateau region in the profile and the reversible capacities reached to ca. 90 mAhg^{-1} . The irreversible capacity gradually decreased with an increase in the cycle number and was negligible at 10th cycle. When the upper potential limit was set at 5.1 V vs. Na^+/Na (Fig. 4.2b),

the charge profile shows the 3rd potential plateau in the high potential region above 4.8 V vs. Na⁺/Na and the reversible capacities reached to ca. 104 mAhg⁻¹ at 1st cycle and ca. 110 mAhg⁻¹ at 10th cycle. Although 1.33 electron reaction should be required to deliver the theoretical capacity of 170 mAhg⁻¹, the reversible capacity of 110 mAhg⁻¹ was limited to ca. 0.86 electron reaction. The irreversible capacity also reached to ca. 73 mAhg⁻¹ at 1st cycle and ca. 18 mAhg⁻¹ even at 10th cycle. In general, typical organic electrolytes are unstable in the high potential region and the electrolyte decomposition would occur in the 3rd potential plateau region. Fig. 4.2c shows the rate performances of Na₄Co_{2.4}Mn_{0.3}Ni_{0.3}(PO₄)₂P₂O₇ at 2C and 5C rates. The reversible capacities reached to ca. 106 mAhg⁻¹ at 2C rate and ca. 103 mAhg⁻¹ at 5C rate. The polarization of the charge/discharge reaction was little enough to maintain high discharge potential above 4.0 V vs. Na⁺/Na even at 5C rate. The material also exhibits high capacity retentions of 93% at 2C rate and 88% at 5C rate at 10th cycle by comparing with 1st cycle (Fig. 4.2d). As shown in Fig. 2e, Na₄Co_{2.4}Mn_{0.3}Ni_{0.3}(PO₄)₂P₂O₇ has two types of redox couples around 4.2 V and 4.6 V vs. Na⁺/Na, corresponding to the first and the second plateau regions in the charge/discharge profiles, respectively. As reported in our previous paper [1], Na₄Co₃(PO₄)₂P₂O₇ has the multi redox couples in the potential region of 4.1-4.7 V and the broad redox couple around 4.6 V on the CVs is not similar with the multi redox behavior of Na₄Co₃(PO₄)₂P₂O₇ in the potential region between 4.3 V and 4.7 V. The difference of their redox behavior indicates Mn and Ni substitutions to Co site would have some influences on the phase transition mechanism during Na⁺ extraction and therefore, we are now under investigating structural changes by Na⁺ extraction during charge reaction and will report elsewhere.

Ex-situ XAS was employed in this study to elucidate the charge compensation mechanism during charge reaction. Normalized Co, Mn and Ni *K*-edge X-ray absorption near-edge structure (XANES) spectra at the pristine and charged electrodes are shown in Fig. 4.3. Here, we

estimated the Co, Ni and Mn *K*-edge absorption energies at the absorbance of 0.5. As described in Fig. 4.3a, the Co *K*-edge absorption energy of the pristine electrode slightly shifted to the higher energy value by charging to 34 mAhg⁻¹ and then clearly increased by charging to 102 mAhg⁻¹. Therefore, Co redox proceeds more predominantly in the second plateau region than the first plateau region. The spectra of the pristine and charged electrodes were almost similar to olivine-type LiFe_{0.5}Co_{0.5}PO₄ reported by K.-W. Nam et al. [7] Therefore, Co redox can proceed between roughly divalent and trivalent. No significant energy shift appeared after charged to 136 mAhg⁻¹, but the absorption energy shifted to the lower energy value by charging to 170 mAhg⁻¹. The energy shift implies oxidized Co ions would be partially reduced to lower valence state in spite of charge process.

Next, the Mn *K*-edge XANES spectra and the Mn *K*-edge absorption energies as a function of charge capacity are plotted in Fig. 4.3b. The Mn *K*-edge spectra absorption energy of the pristine electrode clearly shifted to higher energy value by charging to 34 mAhg⁻¹ and then the energy shifted to slightly higher values by charging to 136 mAhg⁻¹. Hence, Mn redox proceeded more predominantly in the first plateau region than the second plateau region. Then, no significant energy shift appeared by charging to 170 mAhg⁻¹. The spectrum of the pristine electrode was similar to olivine-type LiMn_{0.5}Fe_{0.5}PO₄ [8]. In contrast, the absorption energy after charged to 170 mAhg⁻¹ exhibits apparently higher value than that of Li_{1-x}Mn_{0.5}Fe_{0.5}PO₄ (x=1). By comparing these results, it is indicated Mn²⁺ would be oxidized to trivalent or more. Here, ca. 33% of M²⁺ in Na₄M₃(PO₄)₂P₂O₇ must be oxidized to M⁴⁺ to deliver the theoretical capacity of ca. 170 mAhg⁻¹. Hence, the wide valence change of Mn redox strongly suggests Mn substitution should be effective method to enhance the capacity.

Finally, as shown in Fig. 4.3c, Ni *K*-edge absorption energy of the pristine electrode almost linearly-shifted to higher energy values by charging to 102 mAhg⁻¹. Hence, Ni redox has a

possibility to contribute to the charge compensation with Co and Mn redox. The absorption energy shifted to lower and then higher values by further charging to 136 mAhg⁻¹ and 170 mAhg⁻¹, respectively. Therefore, charge compensation by Ni redox has complex reduction and re-oxidation process.

The tiny shifts of the absorption energies above charge capacity of 136 mAhg⁻¹ indicate Co, Mn and Ni redox could not work well, because the irreversible side reaction such as electrolyte decomposition severely occurred as discussed in Fig. 4.2b. The mechanism for partial reductions of oxidized Co and Ni ions is not clarified at this stage, but electrolyte decomposition could affect on oxidation states of each transition metal. Additionally, similar behavior of lithium-rich layered oxides was reported and was associated with ion migration in the structure. [9] Given this, we are now under investigating the structural changes during charge reaction. *Ex-situ* XAS study also revealed Co, Ni and Mn redox proceeded not sequentially but simultaneously in both of the first and the second plateau regions. Simultaneous charge compensation by Co, Mn and Ni redox suggests mixed potential of each redox should appear in two redox couples on the CVs (Fig. 4.2d). Regarding olivine-type LiFe_{0.5}Co_{0.5}PO₄ [7], LiMn_{0.5}Fe_{0.5}PO₄ [8] and LiFe_{1/4}Mn_{1/4}Co_{1/4}Ni_{1/4}PO₄ [10] positive electrodes for LIBs, charge compensation proceeded sequentially at each redox potentials (i.e. Fe²⁺/Fe³⁺ : 3.4 V, Mn²⁺/Mn³⁺ : 4.1 V and Co²⁺/Co³⁺ : 4.8 V vs. Li⁺/Li), resulting in wide operating potential. As compared with the previous results, simultaneous charge compensations by Co, Mn and Ni ions in Na₄Co_{2.4}Mn_{0.3}Ni_{0.3}(PO₄)₂P₂O₇ should be a very distinguishing feature and it should be noted that the derivatives of Na₄Co₃(PO₄)₂P₂O₇ can provide high mixed potentials by using suitable amounts of Mn and/or Ni substitution. We are now undergoing further optimization of the derivatives.

Conclusions

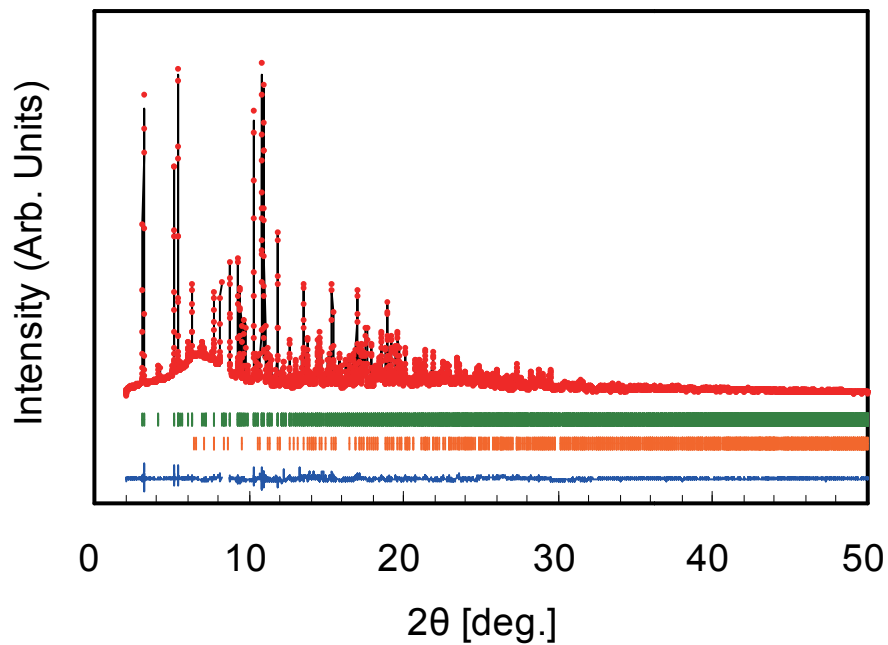
In this chapter, the electrochemical characteristics of $\text{Na}_4\text{Co}_{2.4}\text{Mn}_{0.3}\text{Ni}_{0.3}(\text{PO}_4)_2\text{P}_2\text{O}_7$ and its charge compensation mechanism were investigated. The material shows 4.5 V class high potential and the reversible capacity reached to ca. 103 mAhg^{-1} at 5C rate with maintaining high discharge potential. *Ex-situ* XAS results clarified Ni and Mn redox as well as Co redox contributed to charge compensation of Na^+ extraction simultaneously and therefore, the material can provide high mixed potential of each redox reactions. These results strongly suggest further exploration of $\text{Na}_4\text{Co}_{3-x}\text{M}_x(\text{PO}_4)_2\text{P}_2\text{O}_7$ (Mn and/or Ni) should pave the way for high power and high energy SIBs.

References

- [1] M. Nose, H. Nakayama, K. Nobuhara, H. Yamaguchi, S. Nakanishi and H. Hideki, *Journal of Power Sources* 234 (2013) 175-179.
- [2] H. Kim, I. Park, D.H. Seo, S. Lee, S.-W. Kim, W.J. Kwon, Y.U. Park, C.S. Kim, S. Jeon and K. Kang, *J. Am. Chem. Soc.* 134 (2012) 10369-10372.
- [3] F. sanz, C. parada, U. Amador, M.A. Monge and C. Ruiz-Valero, *J. Solid State Chem.* 123 (1996) 129-139.
- [4] F. Sanz, C. Parada, J.M. Rojo, and C. Ruiz-Valero, *Chem. Mater.* 13 (2001) 1334-1340.
- [5] F. Izumi and K. Momma, *Solid State Phenom.* 130 (2007) 15-20.
- [6] K. Momma and F. Izumi, *J. Appl. Crystallogr.* 41 (2008) 653-658.
- [7] W-S. Yoon, K-Y. Chung, K-W Nam, J. McBreen, D. Wang, X. Huang, H. Li, L. Chen and X-Q. Yang, *Journal of Power Sources* 183 (2008) 427-430.
- [8] K-W. Nam, W-S. Yoon, K. Zaghib, K-Y. Chung and X-Q. Yang, *Electrochemistry Communications* 11 (2009) 2023-2026.

- [9] M. Oishi, T. Fujimoto, Y. Takanashi, Y. Orikasa, A. Kawamura, T. Ina, H. Yamashige, D. Takamatsu, K. Sato, H. Murayama, H. Tanida, H. Arai, H. Ishii, C. Yogi, I. Watanabe, T. Ohta, A. Mineshige, Y. Uchimoto and Z. Ogumi, *Journal of Power Sources* 222 (2013) 45-51.
- [10] K-W. Nam, X-J. Wang, W-S. Yoon, H. Li, X. Huang. O. Haas, J. Bai and X-Q. Yang, *Electrochemistry Communications* 11 (2009) 913-916.

a)



b)

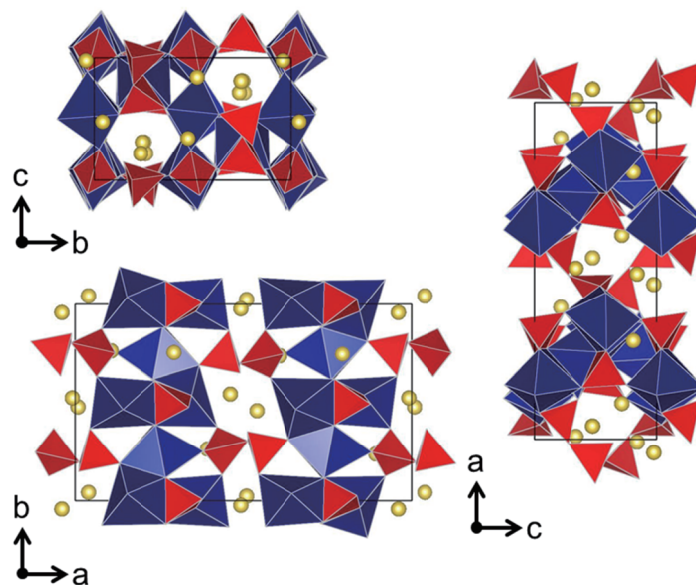


Fig. 4.1 a) Synchrotron X-ray diffraction patterns with Rietveld refinement. The experimental data points (red dots), calculated pattern (black line), Bragg diffraction positions (green tickets for Na₄Co_{2.4}Mn_{0.3}Ni_{0.3}(PO₄)₂P₂O₇ and orange tickets for NaCoPO₄) and the difference curve (blue line). b) Refined crystal structure of Na₄Co_{2.4}Mn_{0.3}Ni_{0.3}(PO₄)₂P₂O₇.

Table 1. Refined atomic position of $\text{Na}_4\text{Co}_{2.4}\text{Ni}_{0.3}\text{Mn}_{0.3}(\text{PO}_4)_2\text{P}_2\text{O}_7$ prepared by sol-gel method.

Atom	x	y	z	Temperature factor	Occupancy
Co1/Co	0.165584	0.002417	0.062696	0.375725	0.800000
Ni1/Ni	0.165584	0.002417	0.062696	0.375725	0.100000
Mn1/Mn	0.165584	0.002417	0.062696	0.375725	0.100000
Co2/Co	0.139002	0.494319	0.071979	0.375725	0.800000
Ni2/Ni	0.139002	0.494319	0.071979	0.375725	0.100000
Mn2/Mn	0.139002	0.494319	0.071979	0.375725	0.100000
Co3/Co	0.242799	0.742349	0.339551	0.375725	0.800000
Ni3/Ni	0.242799	0.742349	0.339551	0.375725	0.100000
Mn3/Mn	0.242799	0.742349	0.339551	0.375725	0.100000
P1/P	0.292383	0.503158	0.067646	0.638996	1.000000
P2/P	0.178899	0.486484	0.577236	0.638996	1.000000
P3/P	0.068100	0.762942	0.211257	0.638996	1.000000
P4/P	0.051399	0.230064	0.018444	0.638996	1.000000
Na1/Na	0.005890	0.476049	0.350160	1.212940	1.000000
Na2/Na	0.204600	0.248386	0.316710	1.212940	1.000000
Na3/Na	0.393722	0.263609	0.239731	1.212940	1.000000
Na4/Na	0.038742	0.041728	0.494960	1.212940	1.000000
O1/O	0.237251	0.612400	0.110610	0.192184	1.000000
O2/O	0.347121	0.475558	0.246604	0.192184	1.000000
O3/O	0.162914	0.036054	0.382841	0.192184	1.000000
O4/O	0.239304	0.386760	0.042716	0.192184	1.000000
O5/O	0.269129	0.106460	0.069545	0.192184	1.000000
O6/O	0.375417	0.009323	0.260358	0.192184	1.000000
O7/O	0.235200	0.376267	0.612318	0.192184	1.000000
O8/O	0.136431	0.458328	0.385941	0.192184	1.000000
O9/O	0.013397	0.194914	0.801214	0.192184	1.000000
O10/O	0.056982	0.635766	0.100072	0.192184	1.000000
O11/O	0.122718	0.757604	0.378410	0.192184	1.000000
O12/O	0.417818	0.369213	0.560019	0.192184	1.000000
O13/O	0.042403	0.365450	0.062409	0.192184	1.000000
O14/O	0.131640	0.189191	0.000000	0.192184	1.000000
O15/O	0.010698	0.146948	0.166446	0.192184	1.000000

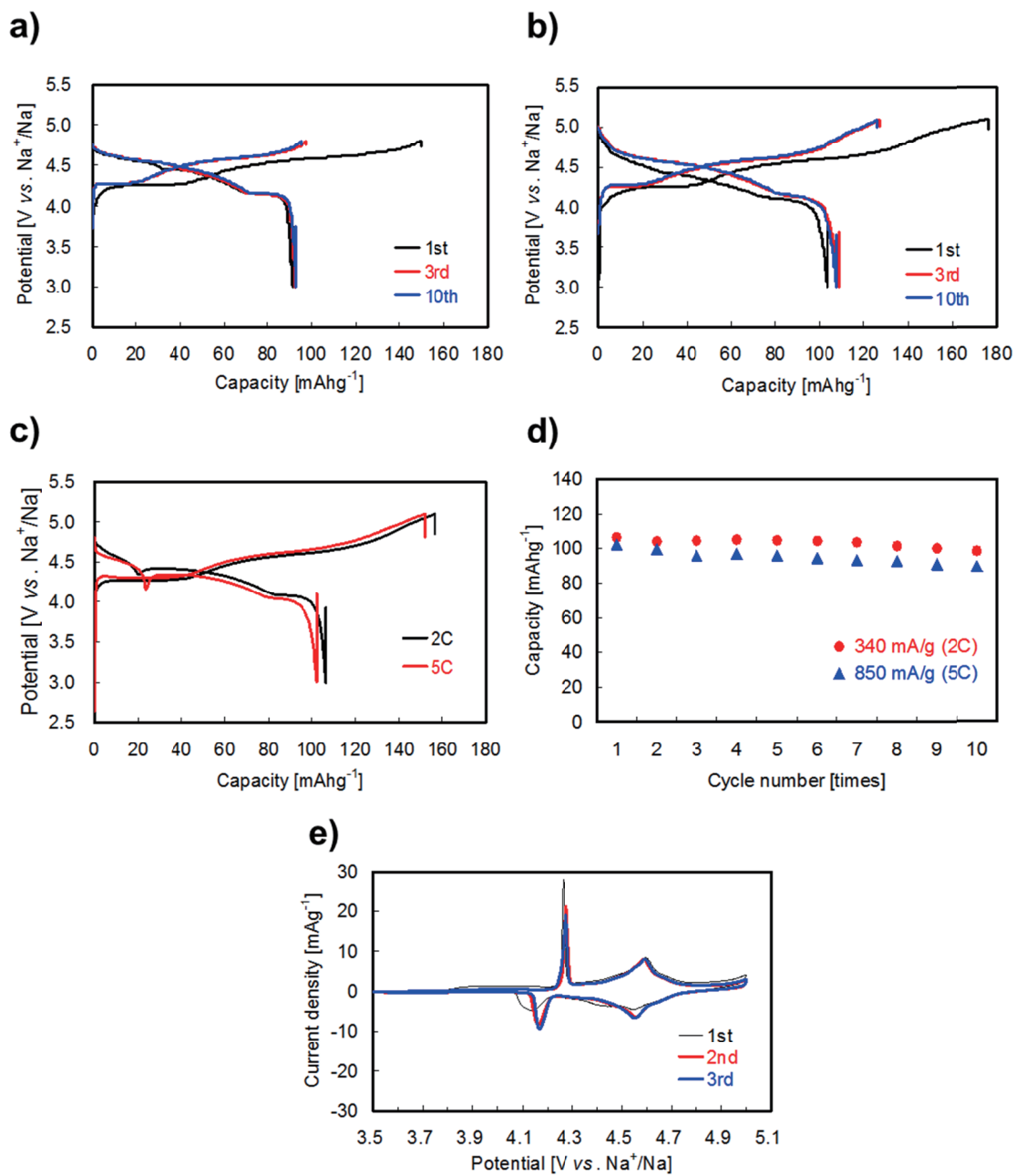


Fig. 4.2 Electrochemical characteristics of $\text{Na}_4\text{Co}_{2.4}\text{Mn}_{0.3}\text{Ni}_{0.3}(\text{PO}_4)_2\text{P}_2\text{O}_7$. Charge/discharge profiles at 0.2C rate in the potential ranges of a) 3.0-4.8 V and b) 3.0-5.1 V. c) Rate and d) cycle performances at 2C and 5C rates. e) Cyclic voltammograms between 3.5 V and 5.0 V vs. Na^+/Na at the scan rate of 0.01 mVs^{-1} .

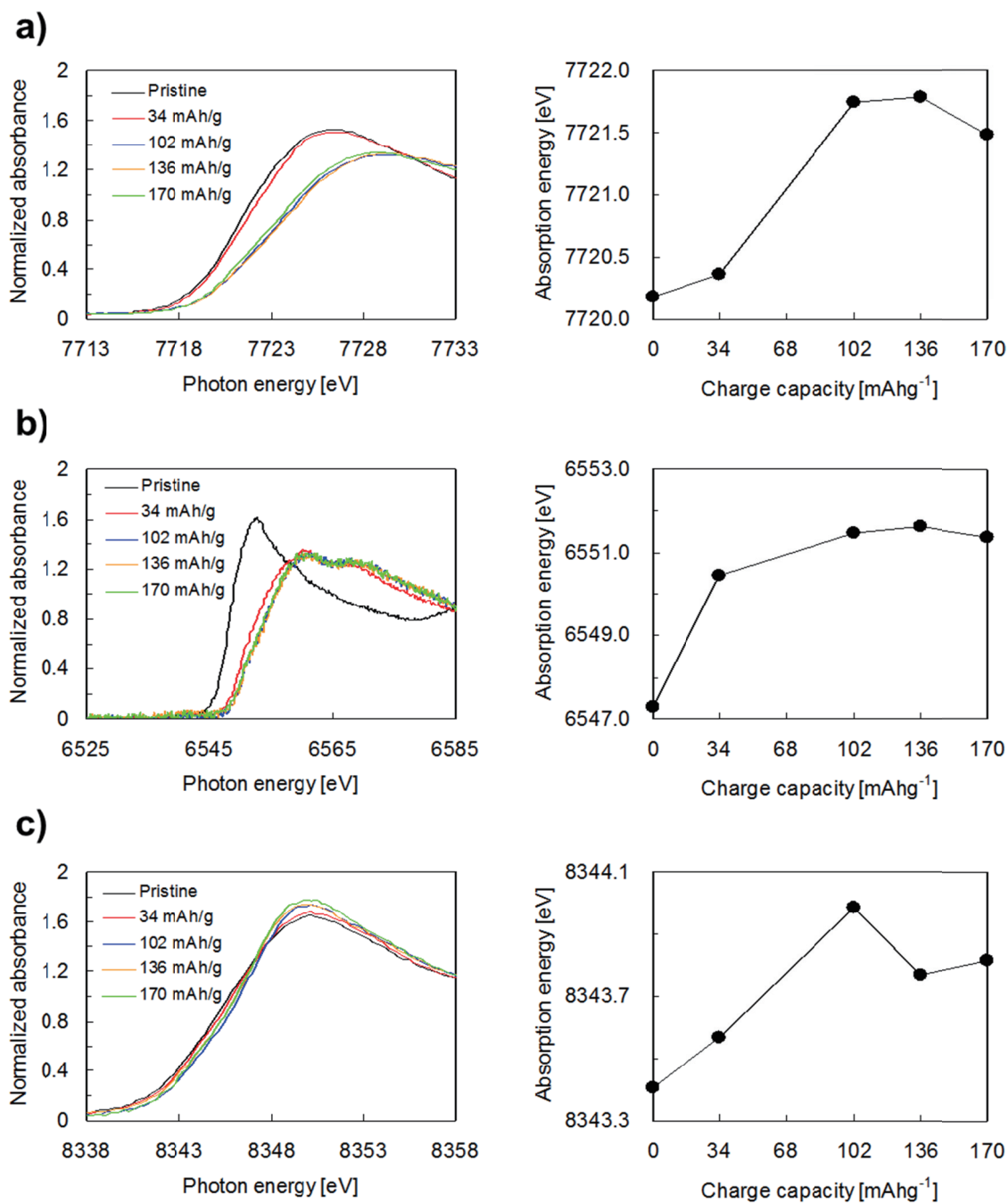


Fig. 4.3 a) Co, b) Mn and c) Ni XANES spectra and absorption energy values at the absorbance of 0.5 obtained from pristine and charged electrodes.

Chapter V

Electrochemical Li⁺ Insertion Capability into Na_{4-x}Co₃(PO₄)₂P₂O₇ and Its Application to Novel Hybrid-ion Battery

5.1. Introduction

Rechargeable batteries have been desired for high energy, high power, safety, sustainability and so on to meet the requirements of large-sale applications such as eco-friendly vehicles. Therefore, much effort has been devoted to develop a variety of batteries in order to establish new electricity storage system which can provide higher energy efficiencies. Nowadays, sodium-ion batteries (SIBs) have been reconsidered as one of the key technologies from the reasons as follows. The first is an abundant of sodium working as an ionic carrier instead of lithium ion and the other is the various intercalation structures, which are not familiar with lithium equivalences. Actually, many unique storage materials for both positive and negative electrodes (e.g. Na₂MP₂O₇ [M=Fe and Mn], Na₂FePO₄F, A_{4x-2}M[Fe(CN)₆]_x·zH₂O [A=Na/K, M=Fe, Mn, Co, Ni, and Zn], Na₃V₂(PO₄)₂F₃, Na₂Ti₃O₇ and Na₂Ti₆O₁₃)¹⁻¹⁰ have been reported. We also discovered mixed polyanion compounds of Na₄M₃(PO₄)₂P₂O₇ [M=Co, Ni and Mn] and its derivatives exhibit high operating potentials and high rate capabilities and therefore can be one of the most promising electrode materials for SIBs.¹¹⁻¹³

The crystal structure of Na₄Co₃(PO₄)₂P₂O₇, which was refined by Sanz et al., has a space group of *Pna2*₁ in an orthorhombic unit cell and four Na⁺ accommodation sites are well designed along multiple diffusion pathways in the crystal structure.^{14, 15} Given the rapid Na⁺ diffusivity in

the crystal structure, ^{11, 12} novel phase $\text{Li}_4\text{Co}_3(\text{PO}_4)_2\text{P}_2\text{O}_7$, isostructural to $\text{Na}_4\text{Co}_3(\text{PO}_4)_2\text{P}_2\text{O}_7$, can be very attractive electrode material for lithium-ion batteries. But unfortunately, we could not obtain $\text{Li}_4\text{Co}_3(\text{PO}_4)_2\text{P}_2\text{O}_7$ by sol-gel method and more stable phases (i.e. LiCoPO_4 and other minor impurities) were produced as shown in Fig. 5.1. Alternatively, $\text{Na}_{4-x}\text{Co}_3(\text{PO}_4)_2\text{P}_2\text{O}_7$ electrode can be prepared by electrochemical oxidation of $\text{Na}_4\text{Co}_3(\text{PO}_4)_2\text{P}_2\text{O}_7$ in sodium-based electrolyte. Hence, we have investigated Li^+ insertion capabilities into $\text{Na}_{4-x}\text{Co}_3(\text{PO}_4)_2\text{P}_2\text{O}_7$ as a host material. Here we describe our findings on Li^+ insertion capabilities of $\text{Na}_{4-x}\text{Co}_3(\text{PO}_4)_2\text{P}_2\text{O}_7$ and the practical application of the compatible Na^+ and Li^+ insertion capabilities to new hybrid-ion battery (HIB) assembled by combining $\text{Na}_4\text{Co}_3(\text{PO}_4)_2\text{P}_2\text{O}_7$ positive electrode and $\text{Li}_4\text{Ti}_5\text{O}_{12}$ negative electrode in lithium-based electrolyte.

5.2. Experimental, results and discussion

Electrochemical Na^+ extraction from $\text{Na}_4\text{Co}_3(\text{PO}_4)_2\text{P}_2\text{O}_7$, prepared by using sol-gel method described in Chapter I, was conducted by charge reaction at the current density of 34 mA g^{-1} (0.2C rate) in 1.0 mol cm^{-3} NaPF_6 dissolved in ethylene carbonate (EC) / diethylene carbonate (DEC) (50:50 by vol.). Here, 1C was defined as the current density of 170 mA g^{-1} , at which its theoretical capacity of 170 mA h g^{-1} can be delivered for an hour. All electrochemical measurements were conducted in thermostatic bath maintaining at 25°C . As shown in Fig. 5.2, $\text{Na}_4\text{Co}_3(\text{PO}_4)_2\text{P}_2\text{O}_7$ delivered the charge capacity of ca. 130 mA h g^{-1} . The ratio of Na : Co after charge reaction was estimated to 1.4 : 3.0 by ICP measurement and therefore we describe the host material as $\text{Na}_{1.4}\text{Co}_3(\text{PO}_4)_2\text{P}_2\text{O}_7$. The result indicates 2.6Na^+ , which corresponds to the capacity of ca. 115 mA h g^{-1} , was extracted from $\text{Na}_4\text{Co}_3(\text{PO}_4)_2\text{P}_2\text{O}_7$ by charge reaction. The extra charge capacity of ca. 15 mA h g^{-1} should be ascribed as oxidation of the organic electrolyte, owing to high electrode potential up to 4.7 V vs. Na^+/Na . After Na^+ extraction, the cell was

dismantled and the charged electrode was carefully rinsed three times in DEC solution. Then, Li^+ insertion into the host structure of $\text{Na}_{1.4}\text{Co}_3(\text{PO}_4)_2\text{P}_2\text{O}_7$ was carried out by discharge reaction at various current densities from 34 mA g^{-1} (0.2C rate) to 850 mA g^{-1} (5C rate) in 1.0 mol cm^{-3} LiPF_6 dissolved in EC/DEC (50:50 by vol.). Figure 5.3 a) shows the discharge profiles at various current densities in lithium-ion cell. Very interestingly, Li^+ insertion into $\text{Na}_{1.4}\text{Co}_3(\text{PO}_4)_2\text{P}_2\text{O}_7$ could work well. The discharge capacity reached to ca. 100 mAh g^{-1} at 0.2C rate and ca. 80 mAh g^{-1} even at 5C rate, corresponding to ca. 2.4Li^+ and 1.9Li^+ insertion, respectively. The capacity retention at 5C rate versus 0.2C rate reached to 80% and the polarization was comparably low enough to maintain high discharge potential. Hence, $\text{Na}_{1.4}\text{Co}_3(\text{PO}_4)_2\text{P}_2\text{O}_7$ can be employed as host material of Li^+ as well as Na^+ .

For the comparison purpose, we also describe the discharge profiles at the same current densities in sodium-ion cell (Fig. 5.3 b). The Li^+ insertion potential at low current density of 34 mA g^{-1} (0.2C rate) ranges from 4.7 to 3.6 V (vs. Li^+/Li) and was lower than the Na^+ insertion potential of 4.1-4.7 V (vs. Na^+/Na), corresponding to ca. 4.4-5.0 V (vs. Li^+/Li). The potential difference would be derived from the difference of chemical potential of Li^+ and Na^+ , implying Li occupancy sites are not similar to Na^+ occupancy sites. The kinetics of Li^+ and Na^+ insertion were comparable from the discharge profile at higher current densities such as 1C, 2C and 5C rates. Na^+ insertion exhibits higher capacity retention of 90% at 5C rate versus 0.2C rate and the polarization (ΔE) during Na^+ insertion at 5C rate was smaller than Li^+ insertion. These comparison revealed Li^+ insertion into $\text{Na}_{1.4}\text{Co}_3(\text{PO}_4)_2\text{P}_2\text{O}_7$ exhibits lower kinetics than Na^+ insertion.

Next, the structural analysis of the pristine, Na^+ -extracted and Li^+ -inserted materials was conducted by powder XRD measurements (Ultima IV, Rigaku corp. Ltd., Japan) using $\text{Cu K}\alpha$ radiation with 40 kV of tube voltage and 40 mA of current. Figure 5.4 shows the XRD patterns.

As compared with the pristine material, the XRD patterns of Na⁺-extracted and Li⁺-inserted materials dramatically change, indicating Na⁺ extraction and then Li⁺ insertion should lead to the drastic changes of the crystal structure. Detail structural refinements are now under investigated, but the significant shifts of diffraction peak positions at Bragg angles around 9-11° and 15-18° can provide valuable information on Li⁺ insertion mechanism. Regarding the pristine electrode, the peaks at Bragg angles of 9.81°, 15.98° and 16.76° were ascribed as the diffractions of the (200), (011) and (210) planes. As summarized in Table 5.1, their lattice spacing was estimated to 9.01 Å, 5.54 Å and 5.28 Å, respectively. The (011) and (210) lattice spacing shrunk to 5.31 Å and 5.04 Å by Na⁺ extraction and subsequently expanded to 5.51 Å and 5.14 Å by Li⁺ insertion, respectively. One of the reasons for the shrinkages and expansions can be explained by the changes of ionic radii by redox reaction of Co²⁺/Co³⁺ (Co²⁺: 82 pm, Co³⁺: 68 pm). The (200) lattice spacing also shrunk from 9.01 Å to 8.69 Å by Na⁺ extraction. But interestingly, the (200) lattice spacing shrunk further up to 8.48 Å by Li⁺ insertion in spite of increasing in ionic radii of Co ion by discharge reaction. The behavior was apparently different from the (011) and (210) planes, suggesting Li⁺ insertion should be accompanied with structural distortion along the (200) plane. Structural distortion during Li⁺ insertion should require higher formation energy, which would contribute to larger polarization especially at high rates. Additionally, the (200), (011) and (210) lattice spacing after Li⁺ insertion were narrower than the pristine electrode. The shrinkage would be derived from smaller ionic radii of Li⁺ than Na⁺ and therefore stronger interaction of Li⁺-O²⁻ than Na⁺-O²⁻, which could affect the lower kinetics of Li⁺ insertion than Na⁺ insertion as discussed in Fig. 5.3. Here we discussed the kinetics of Li⁺ insertion into the host structure of Na_{1.4}Co₃(PO₄)₂P₂O₇ from the standpoint of bulk diffusivity. As is well known, some fundamental studies showed the kinetics of Li⁺ transport at the interface of electrode and electrolyte was lower than Na⁺ transport because of

higher Lewis acidity of Li^+ than Na^+ and therefore higher interaction between Li^+ -solvent than Na^+ -solvent.^{16, 17} Given this point, further studies are currently focussed on the interface of $\text{Na}_x\text{Co}_3(\text{PO}_4)_2\text{P}_2\text{O}_7$ and electrolyte, and will be reported elsewhere.

Finally, the compatible Li^+ and Na^+ insertion capabilities can suggest new HIB by using $\text{Na}_4\text{Co}_3(\text{PO}_4)_2\text{P}_2\text{O}_7$ as a positive electrode. The HIBs, proposed by Barker et al, were assembled by using $\text{Na}_3\text{V}_2(\text{PO}_4)_2\text{F}_3$ or NaVPO_4F as a positive electrode with lithium-based electrolyte.¹⁸⁻²⁰ Nazar et al also discovered $\text{Na}_2\text{FePO}_4\text{F}$ can be employed as a positive electrode in HIB.²¹ In the rocking chair system, Na^+ should be extracted from positive electrodes at 1st charge reaction and then both of Li^+ and Na^+ are inserted into positive electrodes. Given the reaction mechanism, $\text{Na}_4\text{Co}_3(\text{PO}_4)_2\text{P}_2\text{O}_7$ can be suitable for the positive electrode material of HIBs, because of the compatible Na^+ and Li^+ insertion capabilities. We assembled the new HIB (Fig. 5.5 a) by combining $\text{Na}_4\text{Co}_3(\text{PO}_4)_2\text{P}_2\text{O}_7$ positive electrode and $\text{Li}_4\text{Ti}_5\text{O}_{12}$ negative electrode with 1.0 mol dm^{-3} LiPF_6 dissolved in EC/EMC/DMC (30 : 40 : 30 by vol.). $\text{Li}_4\text{Ti}_5\text{O}_{12}$ has higher Li^+ insertion/extraction potential (i.e. 1.5 V vs. Li^+/Li) than Na deposition potential of 0.3 V vs. Li^+/Li . Given the potential margin, the possible Na deposition in the case of using Li metal or graphite (ca. 0.1 V vs. Li^+/Li) as negative electrodes can be eliminated in this system, indicating high safety of the battery. As shown in Fig. 5.5 b), the battery delivered the reversible capacities of ca. 80 mAhg^{-1} at low rates such as 0.2C (6-10 cycles) and ca. 65 mAhg^{-1} and ca. 50 mAhg^{-1} even at high rates of 2C (26-30 cycles) and 5C (31-35 cycles), respectively. When the current density was set at low current density of 34 mA g^{-1} (0.2C) at 36th cycle, the reversible capacity was recovered to ca. 75 mAhg^{-1} (Fig. 5.6) and ca. 70 mAhg^{-1} of the reversible capacity, corresponding to 89% capacity retention versus 1st cycle, was delivered at 50th cycle. As described in Fig. 5.5 c), the new HIB exhibits 3.0 V-class high operating voltage at 0.2C in spite of using high potential negative electrode and the polarization at 2C was low enough to

maintain the high operating voltage of the battery. These performances (i.e. high voltage, rapid charge/discharge capabilities, safety and long term operation) suggest $\text{Na}_4\text{Co}_3(\text{PO}_4)_2\text{P}_2\text{O}_7$ positive electrode should be one of the most key electrode materials for not only SIBs but also HIBs and it should be noted that a variety of not only Na^+ but also Li^+ insertion materials as a negative electrode can be combined with $\text{Na}_4\text{Co}_3(\text{PO}_4)_2\text{P}_2\text{O}_7$ or its derivatives as a positive electrode to establish new electricity storage systems.

5.3. Conclusions

In this paper, we discovered Li^+ insertion capabilities into $\text{Na}_{4-x}\text{Co}_3(\text{PO}_4)_2\text{P}_2\text{O}_7$ and demonstrated the practical application of the compatible Na^+ and Li^+ capabilities to hybrid-ion batteries. $\text{Na}_{1.4}\text{Co}_3(\text{PO}_4)_2\text{P}_2\text{O}_7$ exhibits rapid Li^+ insertion capabilities (i.e. 100 mAhg^{-1} and 80 mAhg^{-1} at 0.2C and 5C rates, respectively) and therefore can be employed as a good host material of Li^+ . The compatible Li^+ and Na^+ insertion capabilities suggest new hybrid-ion battery by combining $\text{Na}_4\text{Co}_3(\text{PO}_4)_2\text{P}_2\text{O}_7$ and $\text{Li}_4\text{Ti}_5\text{O}_{12}$ in lithium-based electrolyte. The battery exhibits 3.0 V-class high voltage in spite of using high potential negative electrode, indicating high power and safety of the battery, which are strongly required for large-scale applications such as eco-friendly vehicles.

References

- [1] P. Barpanda, T. Ye, S. Nishimura, S. C. Chung, Y. Yamada, M. Okubo, H. Zhou and A. Yamada, *Electrochem. Commun.*, 2012, **24**, 116-119.
- [2] P. Barpanda, G. Liu, C. D. Ling, M. Tamaru, M. Avdeev, S. C. Chung, Y. Yamada and A. Yamada, *Chem. Mater.*, 2013, **25(17)**, 3480-3487.

- [3] P. Barpanda, T. Ye, M. Avdeev, S. C. Chung and A. Yamada, *J. Mater. Chem. A*, 2013, **1**, 4194-4197.
- [4] N. Recham, J. N. Chotard, L. Dupont, K. Djellab, M. Armand and J. M. Tarascon, *J. Electrochem. Soc.*, 2009, **156**, A993-A999.
- [5] Y. Lu, L. Wang, J. Cheng and J. B. Goodenough, *Chem. Commun.*, 2012, **48**, 6544-6546.
- [6] T. Matsuda, M. Takachi and Y. Moritomo, *Chem. Commun.*, 2013, **49**, 2750-2752.
- [7] H. Lee, Y. I. Kim, J. K. Park and J. W. Choi, *Chem. Commun.*, 2012, **48**, 8416-8418.
- [8] K. Chihara, A. Kitajou, I. D. Gocheva, S. Okada, J. Yamaki, *J. Power Sources*, 2013, **227**, 80-85.
- [9] P. Senguttuvan, G. Rouse, V. Seznec, J. M. Tarascon and M. Rosa Palacín, *Chem. Mater.*, 2011, **23**, 4109-4111.
- [10] A. Rudola, K. Saravanan, S. Devaraj, H. Gong and P. Balaya, *Chem. Commun.*, 2013, **49**, 7451-7453.
- [11] M. Nose, H. Nakayama, K. Nobuhara, H. Yamaguchi, S. Nakanishi and H. Hideki, *J. Power Sources*, 2013, **234**, 175-179.
- [12] M. Nose, S. Shiotani, H. Nakayama, K. Nobuhara, S. Nakanishi, H. Iba, *Electrochem. Commun.*, 2013, **34**, 266-269.
- [13] M. Nose, H. Nakayama, K. Nobuhara, S. Nakanishi and H. Iba, *THE 53RD BATTERY SYMPOSIUM IN JAPAN*, 2012, **2E07**, 309.
- [14] F. Sanz, C. Parada, U. Amador, M.A. Monge and C. Ruiz-Valero, *J. Solid State Chem.*, 1996, **123**, 129-139.
- [15] F. Sanz, C. Parada, J. M. Rojo, and C. Ruiz-Valero, *Chem. Mater.*, 2001, **13**, 1334-1340.

- [16] F. Sagane, T. Abe, Y. Iriyama and Z. Ogumi, *J. Power Sources*, 2005, **146**, 749-752.
- [17] F. Sagane, T. Abe, and Z. Ogumi, *J. Power Sources*, 2010, **195**, 7466-7470.
- [18] J. Barker, M. Y. Saidi, J. L. Swoyer, *J. Electrochem. Soc.*, 2004, **151(10)**, A1670-A1677.
- [19] J. Barker, R. K. B. Gover, P. Burns, A. J. Bryan, *Electrochem. Solid-State Lett.*, 2006, **9(4)**, A190-A192.
- [20] J. Barker, R. K. B. Gover, P. Burns, A. J. Bryan, *J. Electrochem. Soc.*, 2007, **154(9)**, A882-A887.
- [21] B. L. Ellis, W. R. M. Makahnouk, Y. Makimura, K. Toghil and L. F. Nazar, *Nat. Mater.*, 2007, **6**, 749-753.

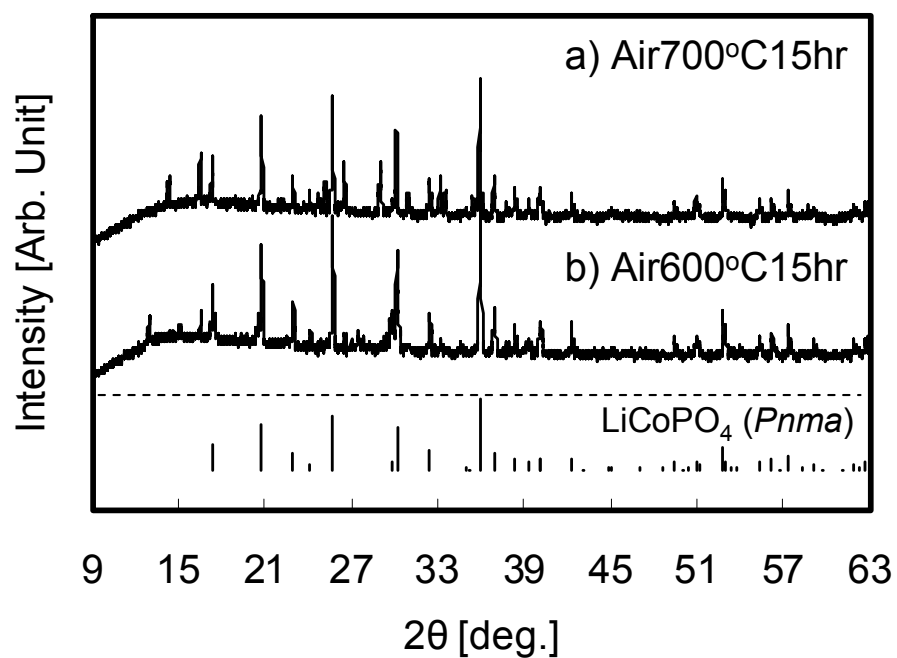


Fig. 5.1 XRD patterns of as-prepared materials by sol-gel method and heat treatment at a) 600°C and b) 700°C for 15hr under air atmosphere.

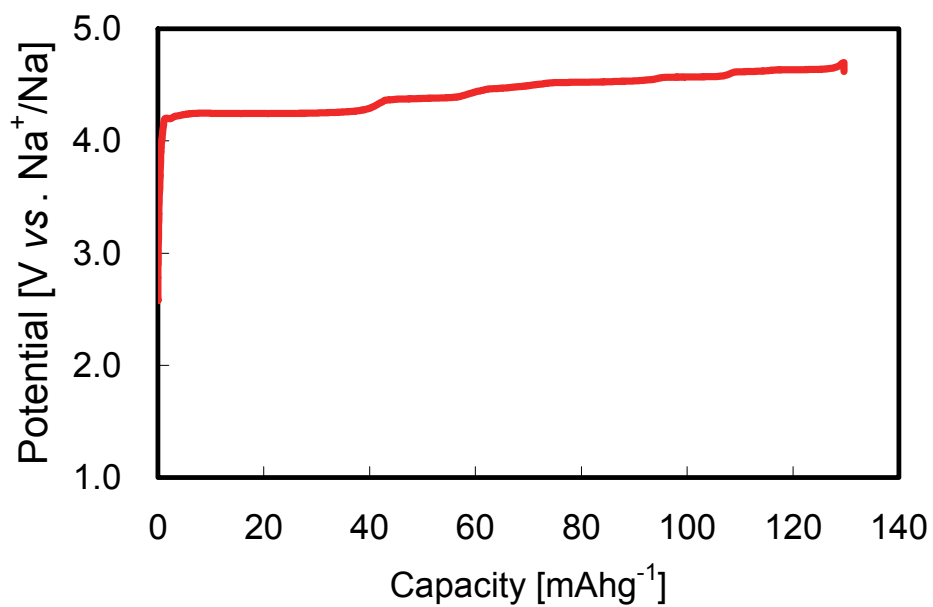


Fig. 5.2 Charge profile of $\text{Na}_4\text{Co}_3(\text{PO}_4)_2\text{P}_2\text{O}_7$ at 34 mA g^{-1} (0.2C) up to 4.7 V vs. Na^+/Na in 1.0 mol dm^{-3} NaPF_6 in EC/DEC [50 : 50 by vol. %].

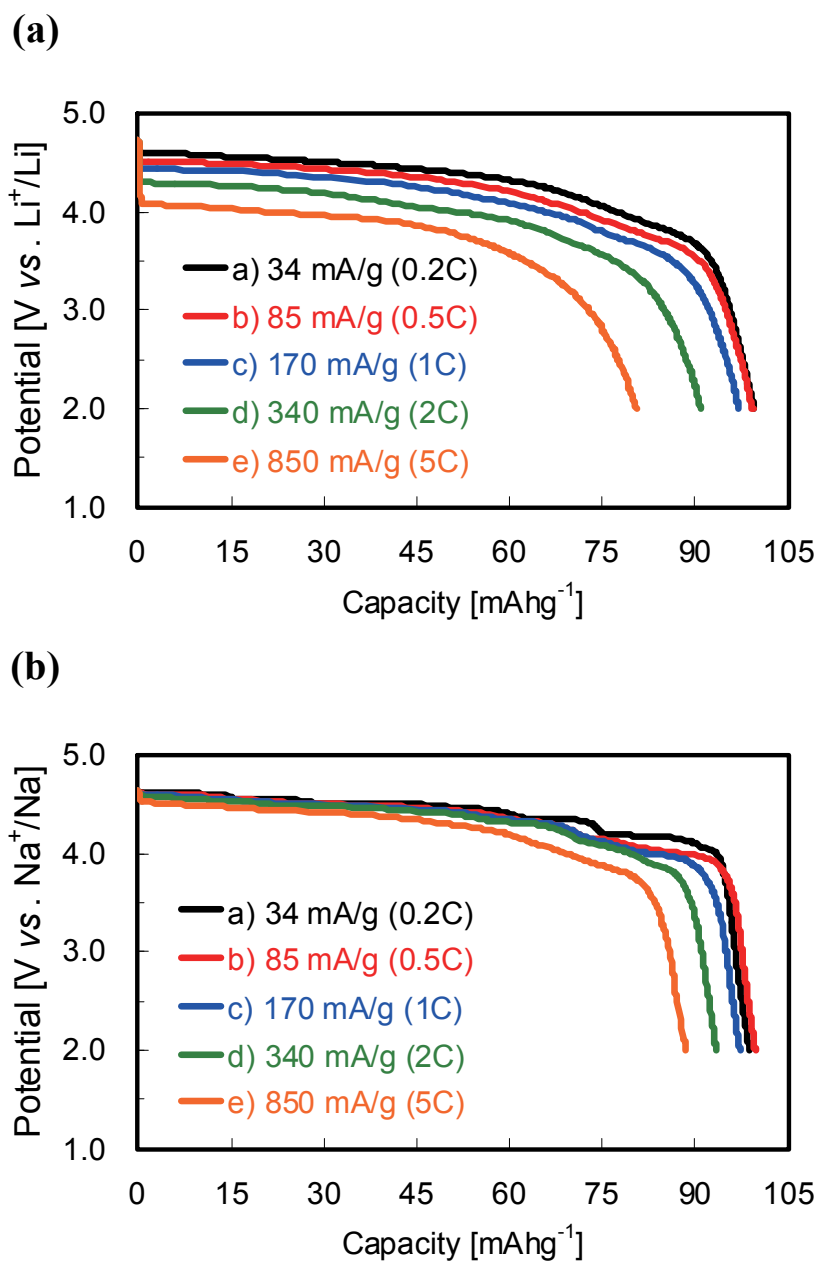


Fig. 5.3 Discharge profiles of $\text{Na}_{1.4}\text{Co}_3(\text{PO}_4)_2\text{P}_2\text{O}_7$ at the current densities of 34 mAg^{-1} (0.2C), 85 mAg^{-1} (0.5C), 170 mAg^{-1} (1C), 340 mAg^{-1} (2C) and 850 mAg^{-1} (5C) in a) lithium-ion cell and b) sodium-ion cell.

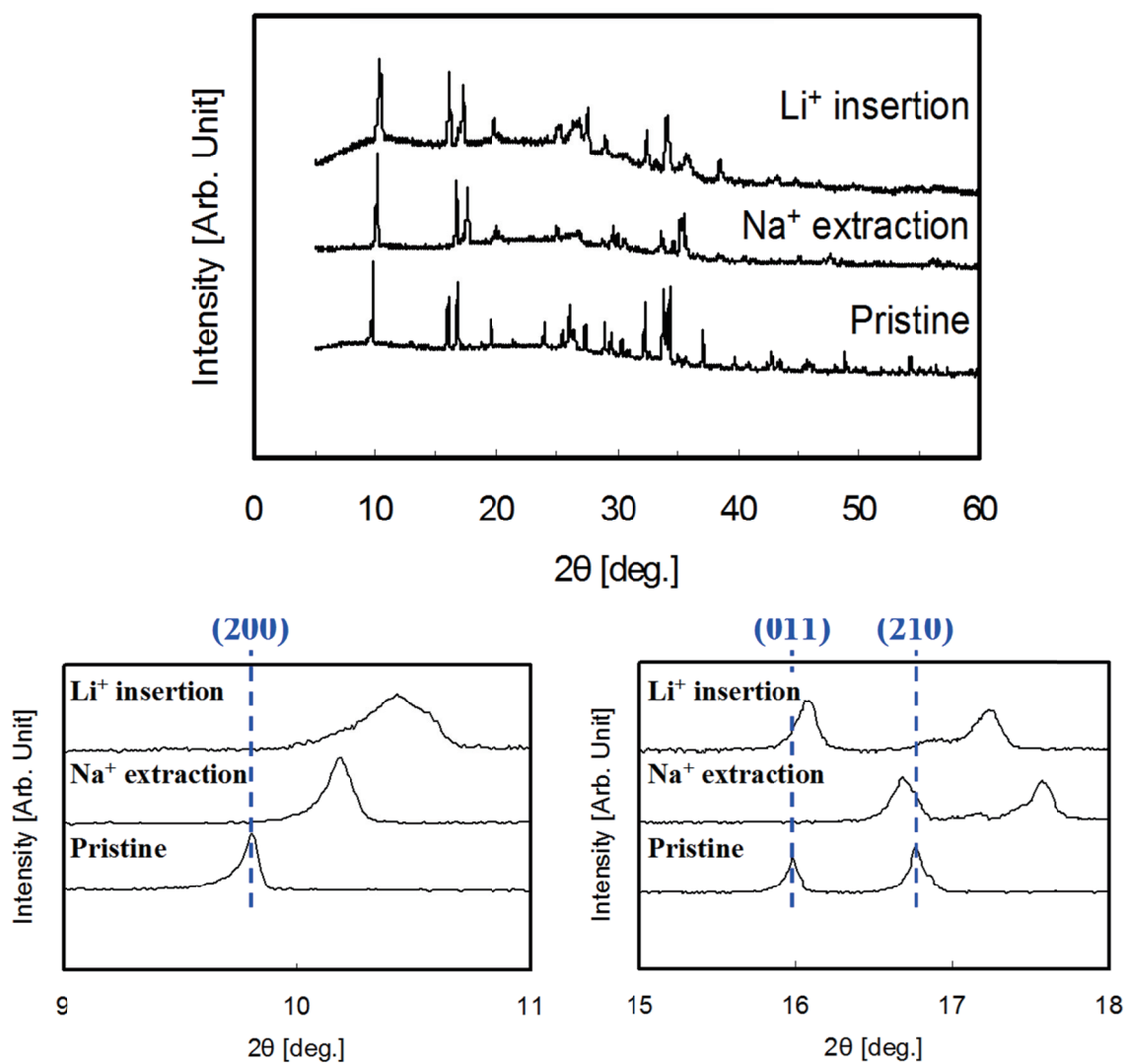
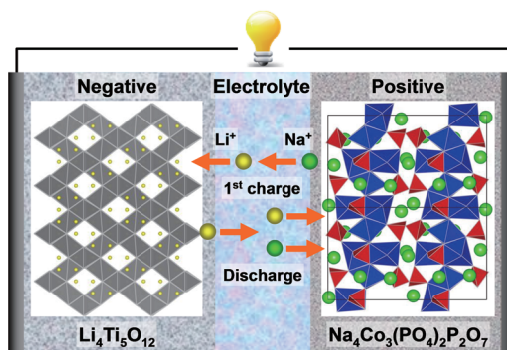


Fig 5.4 *ex-situ* XRD patterns of as-prepared, Na⁺ extracted and Li⁺ inserted electrode material.

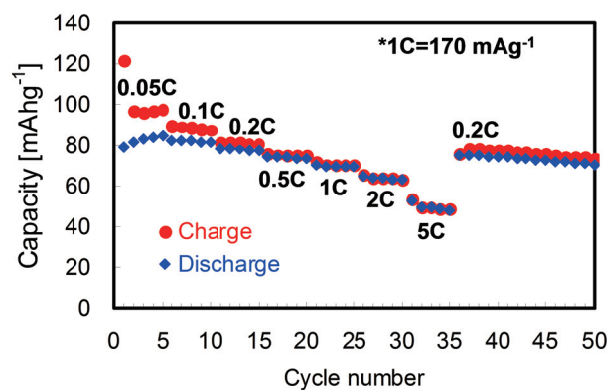
Table 5.1 d-values of the (200), (011) and (210) lattice planes.

Composition	d values		
	(200)	(011)	(210)
$\text{Na}_4\text{Co}_3(\text{PO}_4)_2\text{P}_2\text{O}_7$	9.01 Å	5.54 Å	5.28 Å
$\text{Na}_{1.4}\text{Co}_3(\text{PO}_4)_2\text{P}_2\text{O}_7$	8.69 Å	5.31 Å	5.04 Å
$\text{Li}_{2.4}\text{Na}_{1.4}\text{Co}_3(\text{PO}_4)_2\text{P}_2\text{O}_7$	8.48 Å	5.51 Å	5.14 Å

(a)



(b)



(c)

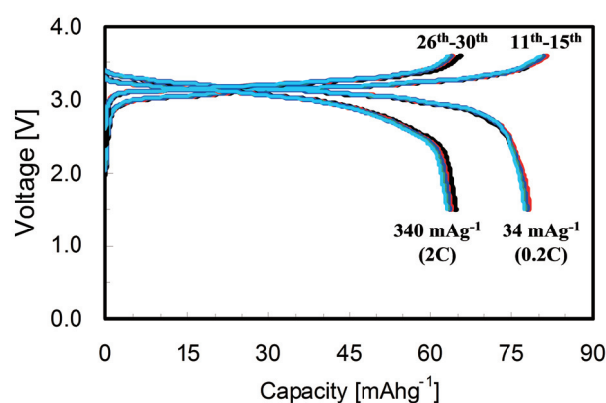


Fig. 5.5 a) Schematic image, b) cycle performance at various C-rates and c) typical charge/discharge profiles at 34 mAhg^{-1} (11th-15th) and 340 mAhg^{-1} (26th-30th) of the new HIB assembled by $\text{Li}_4\text{Ti}_5\text{O}_{12}$ negative electrode and $\text{Na}_4\text{Co}_3(\text{PO}_4)_2\text{P}_2\text{O}_7$ positive electrode with 1.0 mol dm^{-3} LiPF_6 dissolved in EC/EMC/DMC (30:40:30 by vol.)

F

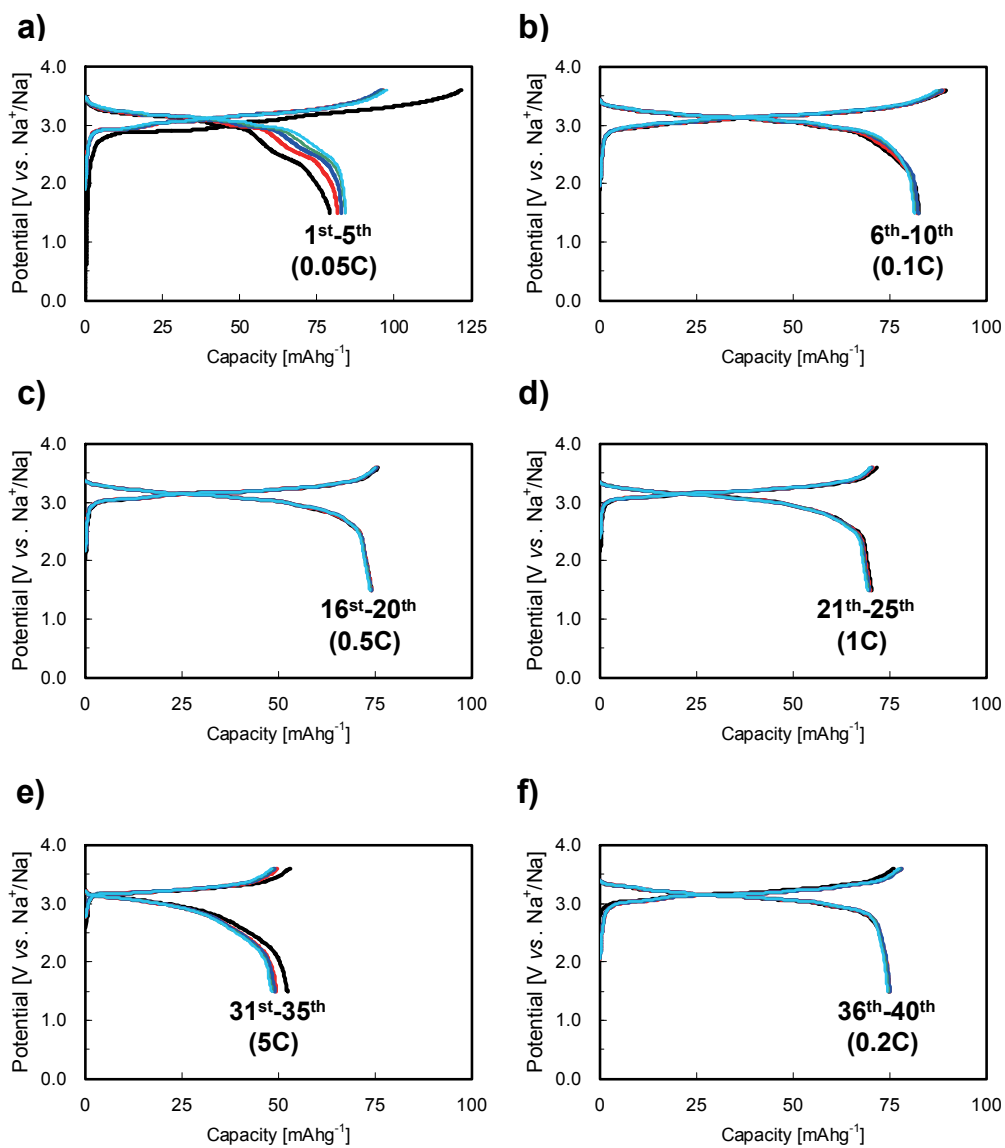


Fig. 5.6 Charge/discharge profiles of the new HIB at a) 1-5 cycles (0.05C), b) 6-10 cycles (0.1C), c) 16-20 cycles (0.5C), d) 21-25 cycles (1C), 31-35 cycles (5C) and 36-40 cycles (0.2C).

Publication List

Chapter I

$\text{Na}_4\text{Co}_3(\text{PO}_4)_2\text{P}_2\text{O}_7$; Novel Electrode Material for Sodium-ion Batteries

Masafumi Nose, Hideki Nakayama, Kunihiro Nobuhara, Hiroyuki Yamaguchi, Shinji Nakanishi, Hideki Iba

Journal of Power Sources, 234, (2013), 175–179

Chapter II

Structural and Electrical Analysis of $\text{Na}_4\text{Co}_3(\text{PO}_4)_2\text{P}_2\text{O}_7$ during Electrochemically Na^+ Extraction/Insertion

Hiroki Moriwake, Akihide Kuwabara, Craig A. J. Fisher, Masafumi Nose, Hideki Nakayama, Shinji Nakanishi, Hideki Iba and Yuichi Ikuhara

Journal of Power Source, Submitted.

Chapter III

$\text{Na}_4\text{Ni}_3(\text{PO}_4)_2\text{P}_2\text{O}_7$; First-ever Experimental Evidence on Potentially Highest Properties of Nickel-based Polyanion Family

Masafumi Nose, Hideki Nakayama, Shinji Nakanishi, Hideki Iba and Takeshi Abe

In preparation

Chapter IV

$\text{Na}_4\text{Co}_{2.4}\text{Mn}_{0.3}\text{Ni}_{0.3}(\text{PO}_4)_2\text{P}_2\text{O}_7$: High Potential and High Capacity Electrode Material for Sodium-Ion Batteries

Masafumi Nose, Shinya Shiotani, Hideki Nakayama, Kunihiro Nobuhara, Shinji Nakanishi, Hideki Iba

Electrochemistry Communications, 34, (2013), 266–269

Chapter V

Electrochemical Li^+ Insertion Capability into $\text{Na}_{4-x}\text{Co}_3(\text{PO}_4)_2\text{P}_2\text{O}_7$ and Its Application to Novel Hybrid-ion Battery

Masafumi Nose, Kunihiro Nobuhara, Shinya Shiotani, Hideki Nakayama, Shinji Nakanishi and Hideki Iba

RSC Advance, 4, (2014), 9044-9047

Not including in this thesis

First-principles study of alkali metal-graphite intercalation compounds

Kunihiro Nobuhara, Hideki Nakayama, Masafumi Nose, Shinji Nakanishi and Hideki Iba

Journal of Power Sources, **243**, (2013), 585–587.

Study of New Active Materials for Rechargeable Sodium-Ion Batteries

S. Nakanishi, M. Nose, H. Nakayama and H. Iba

Advances in Science and Technology, **93**, (2014), 137-145.

Electrochemical reactions of layered niobate material as novel anode for sodium ion batteries

Hideki Nakayama, Masafumi Nose, Shinji Nakanishi and Hideki Iba

Journal of Power Sources, **287**, (2015), 158-163.